Hyperon Production in Lead-Lead and Proton-Beryllium Interactions at 158 GeV/c per Nucleon

Michael Thompson

Thesis submitted for the degree of
Doctor of Philosophy

Particle Physics Group,
School of Physics and Astronomy,
University of Birmingham.

October, 1999.

Synopsis

One of the key probes of the behaviour of hot, dense hadronic matter is strangeness production. Such matter is produced in ultra-relativistic heavy ion collisions and may undergo a phase transition into a state called the *Quark Gluon Plasma* (QGP). The formation of the QGP would lead to an enhancement in the production of strange particles; the measurement of this enhancement being the aim of the WA97 experiment, following on from experiments WA85 and WA94.

In both 1995 and 1996 the WA97 experiment studied lead ion collisions on a lead target at 158 GeV/c per nucleon while control data using a proton beam was also taken in the same years. In 1995 a lead target was used for the proton data while in 1996 the target was changed to beryllium. The proton beam data acted as a control since the conditions found in such collisions are not sufficient to create the QGP. Charged particles were detected in a kinematic acceptance region around central rapidity and at medium p_T. The production of strangeness in all runs was measured by reconstructing the weak decays of strange hadrons, primarily the Λ, Ξ and Ω hyperons.

The geometry of the WA97 apparatus results in the acceptance region having curved limits in rapidity and p_T. Various methods of compensating for the shape of the acceptance region when extracting transverse mass distributions will be described in this thesis, with these methods tested and compared using the 1995 Pb-Pb hyperon data samples. These comparisons confirmed that the log likelihood method already in use was the best method.

Analysis has also been performed on the 1996 p-Be data, with transverse mass distributions and normalised yields per event for Λ and $\overline{\Lambda}$ hyperons being presented. These results are compared with the p-Be results for Ξ^-, $\overline{\Xi}^+$ and $\Omega^-+\overline{\Omega}^+$ hyperons as well as similar results from the p-Pb and 1995 Pb-Pb data. The inverse slopes obtained from the transverse mass distributions, for Λs and Ξs, increase from p-Be through p-Pb to Pb-Pb. A similar increase with the collision system is observed with the yields per event for all studied particle species. The yields per event per participant are consistent between the p-Be and p-Pb data and, for the centrality range studied in the Pb-Pb data, show no increase with centrality. These yields are, however, significantly greater in Pb-Pb than in the proton beam data, with this enhancement increasing with the strangeness content of the particle.

Author's Contribution

The author's contribution to the fixed target heavy ion program at CERN can be split into two parts. The major contribution has been to the data analysis of WA97. While the author's work on evaluating methods for correcting for the acceptance of the WA97 detector confirmed the choice of the method already in use, this work did involve calculating a significant proportion of the Λ and $\overline{\Lambda}$ hyperon weights for the 1995 Pb-Pb data.

For the p-Be data, the author was once more concerned with the Λ and $\overline{\Lambda}$ hyperon samples. This time the contribution was more extensive, with the author being responsible for determining the selection criteria, calculating the majority of the weights, extracting the m_T distributions and calculating the final yields per event. Throughout the author's analysis work presentations were made on the status of the work every few months to the rest of the collaboration.

The author's involvement with NA57 was more limited, being restricted to performing shifts. These shifts were undertaken during the mapping of the field of the Goliath magnet and all the data taking runs up to and including the 1999 p-Pb run.

Acknowledgements

I would like to first thank PPARC for their foresight and wisdom in funding my PhD. I am also grateful to Professor John Dowell for the opportunity to work in the Particle Physics Group in the School of Physics and Astronomy at the University of Birmingham.

Thanks must go to Dr Orlando Villalobos-Baillie, my offical supervisor, for guiding me along the long and winding road that is a PhD. Assisting in no small way with this challenging task were Professor John Kinson and Dr Dave Evans[1]. The latter pair were also instrumental in maintaining my sanity during many long evenings at CERN, though their efforts in this regard pale next to those of the inimitable Dr Frank Votruba. I am grateful to Dr Lawrence Lowe for very helpful computing and system advice, as well as correcting my litany of silly mistakes.

I also owe thanks to all the members of the Particle Physics Group, in particular the 'Omega' group, for generating such a friendly working environment. Fellow students who deserve individual praise are: Paul Norman, Brian Earl, Mark Venables, Shaun Ashby, Alun Lloyd, Dave Lamb and Carrie Goodwin.

Much as it pains me, I must also thank Dr Peter Jones, Rob Barton and Matt Lamont from the *Nuclear* Physics Group (and *NA49* !). The former two for allowing me to 'tag' onto them at QM'99 in Turin and Matt for showing me the delights of the chocolate aisles at Jumbo's.

[1] The "people's councillor" and future Tory Prime Minister!

I must thank all those I met at the most wonderful five days of my life, the Graduate School course at the University of Keele. The course was really 'made' by the people, of whom there are too many to thank by name (even if I could remember them all). My main thanks go to the rest of Group V - Adam, Chris, Charlotte, Caroline, Martin, Katherine, Thomas and our tutor Sue. Despite the initial debacle of the Gas Platform we quickly became a real *team* and good friends. I just hope I wasn't too much of a dead weight. My fellow 'board members' of Gâteau Express also deserve praise for coping magnificantly despite my presence - Ali, Graeme (for his plans for world domination), Paul, Zoe (for the idea of 'novelty' cakes which, as in the business game, will not be pursued here!) and finally Jon. As well as having fun, this course saw me grow as a human being and allowed me to discover myself. I am, therefore, indebted to the research councils and the Careers Research and Advisory Council for organising a course which was as instructive and helpful as it was enjoyable.

Special appreciation goes to Dr Mark Whalley, who was a lecturer at the University of Keele while I was an undergraduate there. Without his guidance and advice I doubt I would've done this PhD.

Most of all I must thank my parents, for their unwaivering love and support throughout my life.

Michael Thompson, October 1999, Birmingham

Contents

List of Figures

List of Tables

Chapter 1

The Quark Gluon Plasma and Heavy Ion Physics

1.1 Introduction

Mankind has pondered the question 'What is the universe made of?' since ancient times. Today, we believe that the fundamental constituents of the universe are the Quarks and Leptons, which have been discovered over the last century.

With the discovery of Quarks in the 1960's came a better understanding of strong interactions, which led to the development of a field theory: Quantum Chromodynamics (QCD). QCD predicts that under extreme conditions of temperature and/or density, hadronic matter will 'melt' into a state of free quarks and gluons known as the *Quark Gluon Plasma* (QGP) [1].

In addition to furthering our understanding of the behaviour of hadronic matter and QCD (non-perturbative QCD and confinement in particular), studying the QGP has importance in other areas. As the phase transition to the QGP is the only field theory phase transition that can be experimentally observed, studying the QGP is an important test of field theory. Studies of the QGP can also help increase our understanding of two astrophysical enigmas: neutron stars and the early universe. Being dense 'balls' of neutrons, the cores of neutron stars may be dense enough for them to be a QGP [2], while the early universe would have been a QGP until the hadrons were formed (about 10^{-5} seconds after the Big Bang) [3].

1.2 The Quark Gluon Plasma

1.2.1 Partons And Colour

Any particle which can interact through the strong force is generically known as a hadron. There are two types of hadrons, half-integer-spin ($\frac{1}{2}\hbar$, $\frac{3}{2}\hbar$) baryons and integer-spin mesons. One of the major discoveries made during the 1960's was the composite nature of baryons and mesons, with their constituents being spin-half particles named *quarks* (the properties of which are summarised in table 1.1). Specifically, baryons are composed of three quarks while mesons consist of a quark and an anti-quark. The discovery of quarks led to the development of a field theory for strong interactions - QCD. As with other field theories, QCD has field quanta which mediate the force between the quarks, these being refered to as *gluons*. Collectively, quarks and gluons are called *partons*.

Baryons, being spin-half, are fermions and as such are required to have anti-symmetric wavefunctions. However, simply composing baryons from three quarks can lead to a symmetric wavefunction. For example, the Ω^- baryon consists of three s quarks, resulting in the flavour part of the wavefunction being symmetric. These are all in the same spin state due the spin of the Ω^- baryon being $\frac{3}{2}\hbar$, so the spin part is also symmetric. If these were the only components of the total wavefunction then it would be symmetric, which is not possible. The solution to this problem is the introduction of a further quantum number: *colour*. This has nothing to do

Table 1.1: Properties of the quarks.

Flavour	Charge/$\lvert e \rvert$	Mass	
		Bound (dynamical)	Partially Chirally Restored (current)
u=up	$+\frac{2}{3}$	350 MeV/c^2	5 MeV/c^2
d=down	$-\frac{1}{3}$	350 MeV/c^2	9 MeV/c^2
s=strange	$-\frac{1}{3}$	550 MeV/c^2	150 MeV/c^2
c=charm	$+\frac{2}{3}$	1.8 GeV/c^2	1.3 GeV/c^2
b=bottom	$-\frac{1}{3}$	5.3 GeV/c^2	4.3 GeV/c^2
t=top	$+\frac{2}{3}$	Not Observed	174 GeV/c^2

with the colour we see with our eyes but is more like electric charge. To create an anti-symmetric colour wavefunction requires that there are three colour charges, Red (R), Blue (B) and Green (G). There are also the corresponding anti-colours, $\overline{R}$, $\overline{B}$ and $\overline{G}$, for the anti-quarks.

1.2.2 Confinement

In most respects QCD is analogous to Quantum Electrodynamics (QED, the field theory of lepton-photon interactions), with one important difference. QCD is a non-Abelian gauge theory whereas QED is Abelian. This means that gluons carry colour while photons do not carry electric charge. Indeed, in order to prevent quarks becoming colourless when emitting a gluon, gluons carry a colour and an anti-colour. For example, a red quark can emit a red-antigreen gluon and become a green quark. So, while photons cannot interact with themselves or each other (since they are neutral), gluons can do so (by virtue of being bi-coloured).

In QED an electron will continuously emit photons, which can then produce a virtual e^+e^-pair, as illustrated in figure 1.1(a). These will become polarised by the field of the real electron (as in figure 1.1(c)) such that, at large distances, the positrons will 'screen' the charge of the real electron. Therefore, in QED this vacuum polarisation causes the potential between two charges to have the form shown in figure 1.1(e), decreasing with increasing distance. This same process also works in QCD (see figure 1.1(b)), with quarks emitting gluons which produce quark-antiquark pairs. The gluons, as they are bicoloured, carry away colour from the quark. If, for example, a green quark emits a green-antiblue it will become a blue quark and the net colour of the pair (green) will no longer be concentrated on the quark. This dilution of the colour charge is further increased because the quark will emit more gluons which may also produce further gluons. The net effect of the gluon and quark-antiquark pair contributions is to surround the quark with a cloud of coloured particles which often carries the net colour of the system. This is illustrated in figure 1.1(d) which shows a quark surrounded by gluons with the net colour of the system (green) *not* on the quark. This dilutes the colour charge, so a probe will see less of the net colour as it moves closer to the quark. The potential felt by the probe will, as a result, increase with increasing distance [4].

The result of this 'anti-screening' is a strong potential of the form given by [5]

$$V_s = \frac{-4\alpha_s}{3r} + \gamma r \tag{1.1}$$

where α_s is the strong coupling constant, r is the distance between quark and antiquark and γ is a constant determined from experiment. As a function of the four-momentum transfer Q^2, which is inversely related to distance, α_s has the form [6]

$$\alpha_s(Q^2) = \frac{12\pi}{(33 - 2n_f)\log(Q^2/\Lambda^2)}$$

where n_f is the number of quark flavours. Λ^2 is the Q^2 scale at which $\alpha_s(Q^2)$ becomes too large for perturbation theory to be used, found by experiment to be about 200 MeV [7]. This gives the distance dependence of α_s illustrated in figure 1.1(f). When r is large, therefore, so are both terms of the potential, meaning it is impossible to find an isolated quark (or antiquark). This property of the strong interaction is known as *confinement*. Conversely, the potential tends to zero as r tends to zero, this being refered to as *asymptotic freedom*.

Quantum Electrodynamics (QED) Quantum Chromodymanics (QCD)

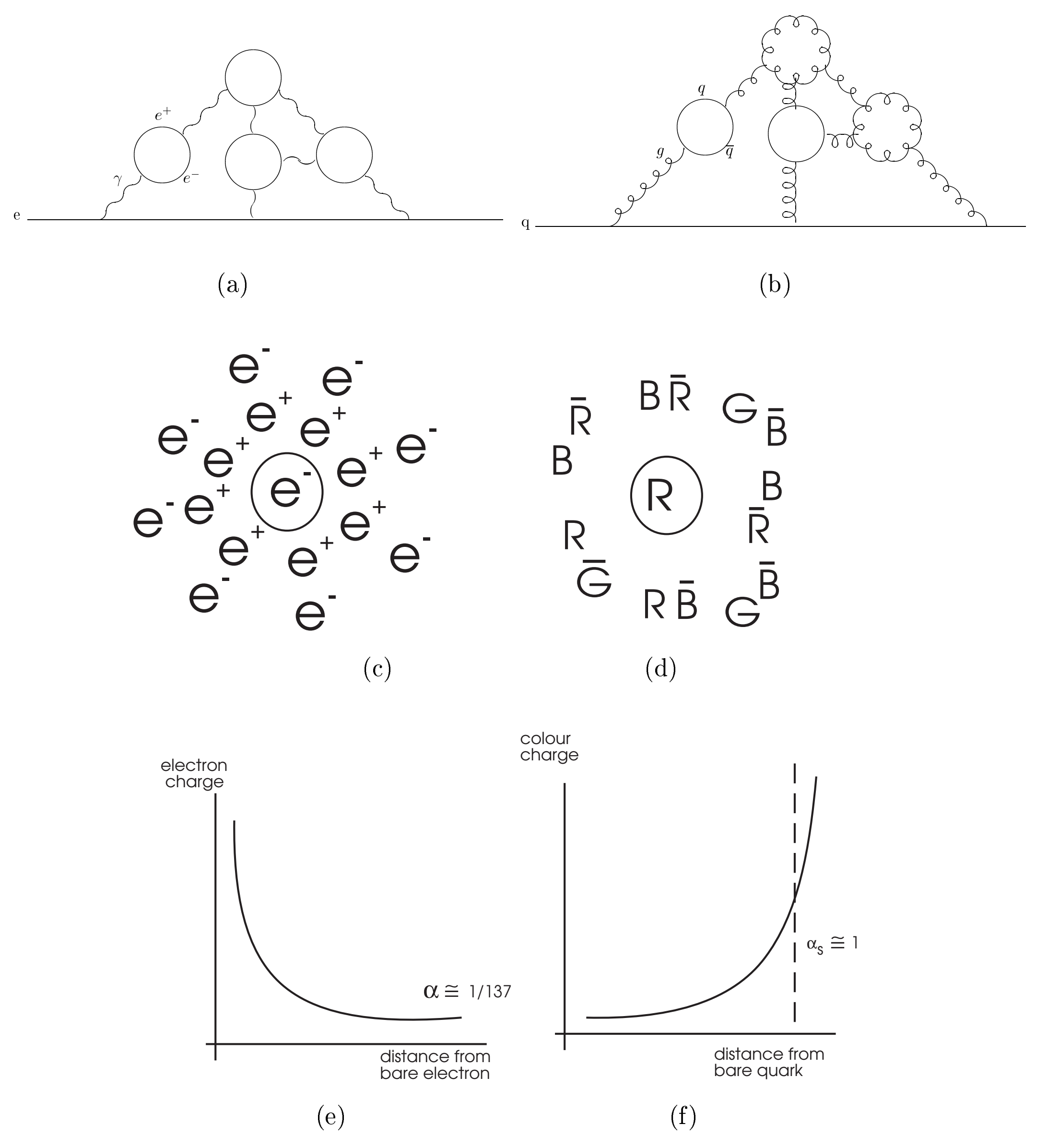

Figure 1.1: Virtual pair production around a) an electron and b) a quark. The charge distribution of these virtual pairs is shown in c) and d) with e) and f) showing the effect on the coupling constants, for electrons and quarks respectively.

1.2.3 Properties of the QGP

The potential given in the last section, equation 1.1, does not account for any effects due to the medium in which the colour charges are embedded. When the effects of a thermodynamic medium of temperature T are included, the potential takes the form [8, 9]

$$V_s(T,r) \sim \frac{\gamma(T)}{1/r_D(T)}(1-\exp(-r/r_D(T))) - \frac{\alpha_s}{r}\exp(-r/r_D(T)) \tag{1.2}$$

where $r_D(T)$ is the Debye screening radius. As the temperature rises $\gamma(T)$ decreases in such a way that above a critical temperature T_c $\gamma(T)=0$ and the potential then becomes simply the second term of equation 1.2

$$V_s(T>T_c,r) \sim -\frac{\alpha_s}{r}\exp(-r/r_D(T>T_c)) \tag{1.3}$$

For $r > r_D(T>T_c)$ it follows that $V(T>T_c,r) \to 0$ and the colour charges are free. If the temperature is sufficiently high, the distance between quarks in a hadron, r_H, will be greater than $r_D(T)$ and they will no longer be bound together, a condition known as *deconfinement*. Deconfinement can also occur at lower temperatures if the baryon density is high enough. In this case, the hadrons may overlap sufficiently for the distance between the quarks to approach zero. Therefore $\exp(-r/r_D(T)) \to 1$ meaning the first term of equation 1.2 tends to zero, as does the second term due to the nature of α_s discussed previously. As a direct consequence of colour screening, therefore, QCD predicts that hadronic matter will undergo a phase transition to a state of asymptotically free quarks and gluons, the QGP, under extreme conditions of temperature and/or density. A schematic illustration of the phase diagram for hadronic matter is shown in figure 1.2. Lattice QCD calculations suggest that T_c is around 150 MeV, which corresponds to a critical energy density in the region of 2-3 GeV/fm^3 [10] (compared with the energy density of normal nuclear matter of about $\frac{1}{2}$ GeV/fm^3). Such high temperatures existed in the early universe (before 10^{-5} seconds after the Big Bang) [3]. It is possible that the QGP still exists today in the Universe, in the cores of neutron stars [2] as they have baryon densities typically ten times that of normal nuclear matter.

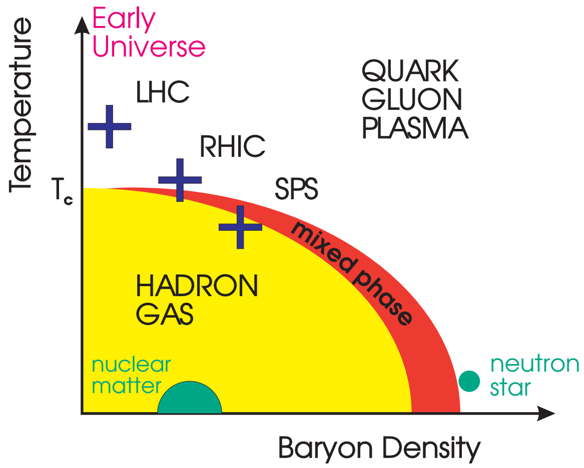

Figure 1.2: Phase diagram in the Temperature-Density plane for baryonic matter. This diagram shows the conditions created (or expected to be created) in experiments using the heavy ion beams of the Super Proton Syncrotron and Large Hadron Collider at CERN and the Relativistic Heavy Ion Collider at Brookhaven.

Another interesting property of the QGP concerns *chiral symmetry*, which relates to particle helicity (also known as handedness). The Dirac equation, $(i\not{\partial}-m)\psi = 0$, has solutions for massless particles which have a definite helicity, $\frac{1}{2}\sigma \cdot \hat{\mathbf{p}}$ [6]. For massive particles the solutions are admixtures of these two chiral states, commonly refered to as left-handed and right-handed states. The total wavefunction ψ is the sum of the left- and right-handed components , ψ_L and ψ_R respectively. Using the projection operators

$$P_L = \frac{1}{2}(1 - \gamma_5)$$

and

$$P_R = \frac{1}{2}(1 + \gamma_5)$$

these components can be written as

$$\psi_L = P_L\psi$$

and

$$\psi_R = P_R\psi.$$

For massless particles the Dirac equation becomes

$$0 = i\overline{\psi}\partial\!\!\!/\psi = i\overline{\psi}_L\partial\!\!\!/\psi_L + i\overline{\psi}_R\partial\!\!\!/\psi_R$$

since

$$\overline{\psi}_L\partial\!\!\!/\psi_R = \overline{\psi}_R\partial\!\!\!/\psi_L = 0$$

The two chiral states are, therefore, decoupled - this being chiral symmetry. If the mass is non-zero then an extra term is added

$$m\overline{\psi}\psi = m(\overline{\psi}_L\psi_R + \overline{\psi}_R\psi_L)$$

which couples the chiral states thus breaking chiral symmetry. It is known that asymptotically free quarks have very low masses compared with their bound masses, see table 1.1. As a consequence, chiral symmetry is expected to be partially restored in a QGP.

1.3 Relativistic Heavy Ion Collisions

It is thought that the way to create a QGP in the laboratory is through the collision of relativistic heavy ions. For the phase transition to occur a large, dense fireball region needs to be created in which a high proportion of the centre of mass energy is converted into thermal energy. The greater the atomic weight of the projectile the greater the size of the dense fireball created in the collision, implying use of the largest nucleus possible. Nucleus nucleus (N-N) collisions also have the advantage of greater *stopping* (the fraction of the beam energy which is converted into thermal energy in a collision) than hadron hadron (h-h) collisions. This results from the large number of h-h interactions which take place in a N-N collision.

A heavy ion collision can be split into three regions; the target and projectile remnants and the central fireball. It is in the last of these, the central fireball, that

QGP formation is expected to occur with the fireball having zero *rapidity* in the centre of mass frame. Rapidity is a kinematic variable defined by

$$Y = \frac{1}{2} \ln \frac{E + p_L}{E - p_L}$$

where E and p_L are the energy and longitudinal momentum of the particle respectively. When subjected to a Lorentz transformation along the beam axis, rapidity has the interesting property that it changes by a constant, which is the same for all particles, such that

$$Y' = Y + A$$

where Y' is the rapidity in the boosted frame. In the case of the Pb-Pb collisions studied by the WA97 collaboration if Y is the centre of mass frame and Y' is the laboratory frame then the constant A is 2.92, which is refered to as *central rapidity*. One important consequence of this concerns the rapidity distribution of the particles. If they are distributed symmetrically about zero in the centre of mass frame, as they are in Pb-Pb collisions, then they will be symmetrically distributed about central rapidity in the boosted frame (see figure 1.3).

A further factor in heavy ion collisions is the impact parameter of the collision. If the impact parameter is small (i.e. *central events*) then nearly all the available nucleons will participate in the interaction, leading to a hot, dense fireball. However, if the impact parameter is large then the collision will be peripheral so that few of the available nucleons will participate. This will reduce the energy and density of the fireball, reducing the likelihood of QGP formation. It is, therefore, interesting to study heavy ion collisions as a function of *centrality*, to look for the phase transition.

As many of the signatures of the QGP are enhancements or suppressions (see next section) control data, in which the QGP is *not* formed, is required. Due to the experimental difficulties in triggering on very peripheral N-N collisions the standard way of obtaining control data is to use a proton beam. Central N-N collisions will produce more particles than more peripheral N-N collisions which in turn will

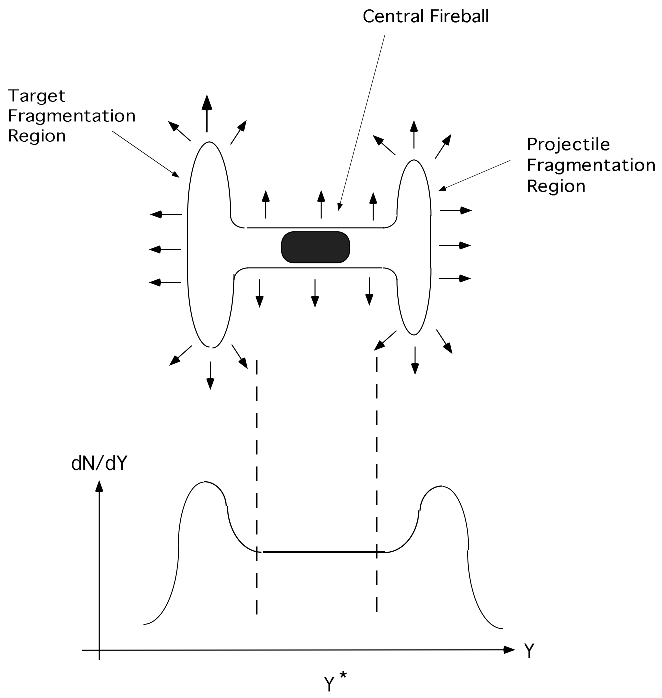

Figure 1.3: Schematic diagram showing a heavy-ion collision and the particle multiplicity as a function of rapidity in the laboratory frame.

produce more than proton induced reactions, whether a QGP is formed or not. Some method of accounting for this is therefore required. The data can be normalised by dividing by the number of negative hadrons or a variable can be found which allows all collision systems to be plotted on the same plot, *e.g.* the number of participants.

1.4 QGP Signatures

If the central fireball created in a heavy ion collision does make the phase transition into the QGP phase it then will expand thermodynamically and emit particles, primarily pions, from its surface thus cooling down. After 2-3$\times10^{-23}$ seconds the temperature density will have fallen enough for the QGP to hadronise back into the Hadron Gas (HG) phase. Figure 1.4 illustrates this evolution of a QGP produced in an ultra-relativistic nucleus-nucleus collision. Immediately after this feeze-out occurs the density will still be high enough for there to be hadronic interactions which could mask signatures of the QGP. Therefore, in order to detect the presence of the QGP requires studying a product of the QGP which does not interact strongly (like thermal photons [11, 12] or dileptons [13, 14]) or one which will survive the hadronisation process. This latter category includes charmonium suppression [9], entropy per baryon [15] and strangeness enhancement [16, 17] (this being the signature chosen by the WA97 collaboration and, hence, one which will be discussed in more detail in the next section).

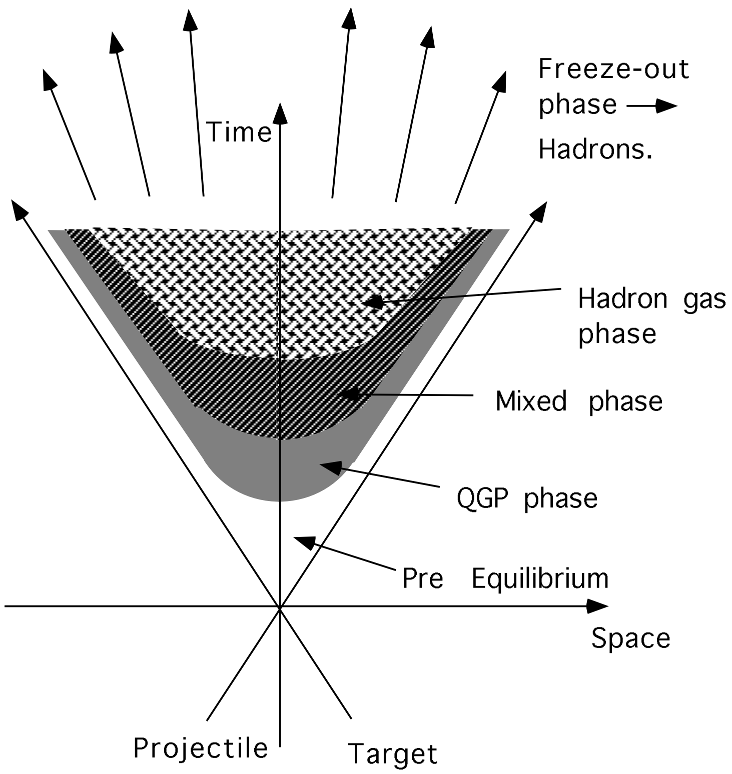

Figure 1.4: The space-time evolution of a heavy ion collision through the QGP phase to particle freeze-out.

1.4.1 Thermal Photons

Particles which do not interact through the strong force, such as photons and leptons (see next subsection), are thought to be good probes of the central fireball because of the nature of the electomagnetic (e-m) force. The mean free path for particles which interact electomagnetically, λ_{em}, in the dense fireball is about $50,000$ fm. As this is much greater than the size of the fireball, which is about 10 fm, most e-m particles do not interact between production and detection. In a QGP single photons are produced in the annihilation of a quark-antiquark pair

$$\mathrm{q}\overline{\mathrm{q}} \rightarrow \gamma g$$

and in quark-gluon interactions

$$g\mathrm{q} \rightarrow \gamma \mathrm{q}$$

In the hadron gas case, photon production is expected to be greater than in a QGP. This is a result of the higher initial temperature (for the same collision conditions) in the hadronic case caused by the fewer degrees of freedom in hadronic matter. Although hadronisation will leave these photons unaffected it will lead to the production of additional photons, through reactions such as

$$\pi^0 \rightarrow 2\gamma$$

and

$$\eta \rightarrow 2\gamma, 3\pi^0$$

The rates of backgrounds like the these increase with the square of the multiplicity, becoming the dominate source of photons in heavy ion collisions.

The WA80 Collaboration has studied photon production in S-Au collisions at 200 GeV [11]. Due to the difficulties mentioned above, the photon spectrum observed by WA80, shown in figure 1.5, is expressed as a 90% confidence level upper limit [18]. The curves shown are model predictions, with the hadronic models clearly predicting greater photon production than both the QGP model and the data, which are consistent. Further model studies [19] show that including two loop corrections leads to better agreement between QGP models and the data. These studies have, however, also found that the hadronic scenario is also consistent with the data, albeit with a quite unphysical density of several hadrons per fm^3.

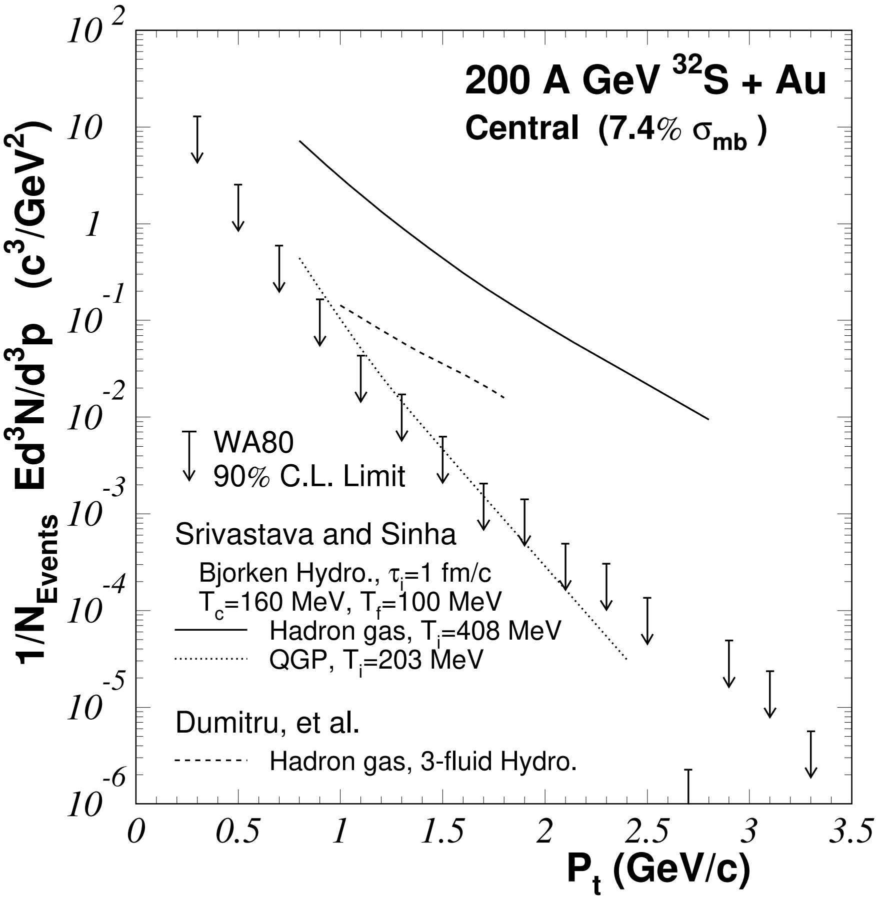

Figure 1.5: 90% confidence level upper limits for photon production observed by WA80. The solid and dashed curves show the results of calculations using hadron gas models while the dotted curve is the expectation based on a QGP scenario.

1.4.2 Dileptons

Leptons share the same advantages as photons for probing the QGP phase. They have the additional advantage that they carry invariant mass, allowing different processes to be distinguished. For single leptons, however, the background from hadron decays, such as

$$\pi^{\pm}, \mathrm{K}^{\pm} \to l^{\pm}\nu,$$

is too great for them to be used. Lepton pairs have much lower backgrounds, primarily combinatorial from the above meson decays and, for e^+e^- pairs, partially reconstructed γ-conversions and π^0-Dalitz decays. These backgrounds are still quite high however, with the rates increasing with the square of the multiplicity. Lepton pairs are produced in the Drell-Yan reaction

$$\mathrm{q\overline{q}} \to l^+l^-$$

within the QGP phase.

Figure 1.6 shows the inclusive e^+e^- mass spectrum found by NA45/CERES in Pb-Au collisions. The solid curve shows the sum of the contributions expected from hadron decays, represented by the dashed curves, assuming no QGP phase in the collision. An excess can clearly be seen in the low mass region $0.25 \leq M_{\mu\mu} \leq 0.7$ GeV/c^2, corresponding to enhancement by a factor of 2.6 ± 0.5(stat.)± 0.6(syst.) for the '96 data [20] and of 3.9 ± 0.9(stat.)± 0.9(syst.) for the '95 data [21]. The HELIOS/3 collabaration studied muon pairs in S-W interactions, from the dimuon threshold up to the J/ψ mass. In the mass range $0.2 \leq M_{\mu\mu} \leq 0.6$ GeV/c^2 the number of muon pairs per charged particle in S-W is greater than the p-W value by (76 ± 4) % [22]. The most likely explanation for this enhancement is $\pi\pi$ annihilation in a hot hadron gas [23]. What is less certain is whether these annihilations procede *via* a ρ meson which has been subjected to a downward mass shift. The lifetime of the ρ is such that a significant fraction could decay during the lifetime of the fireball. If the fireball is in the QGP phase with chiral symmetry partially restored

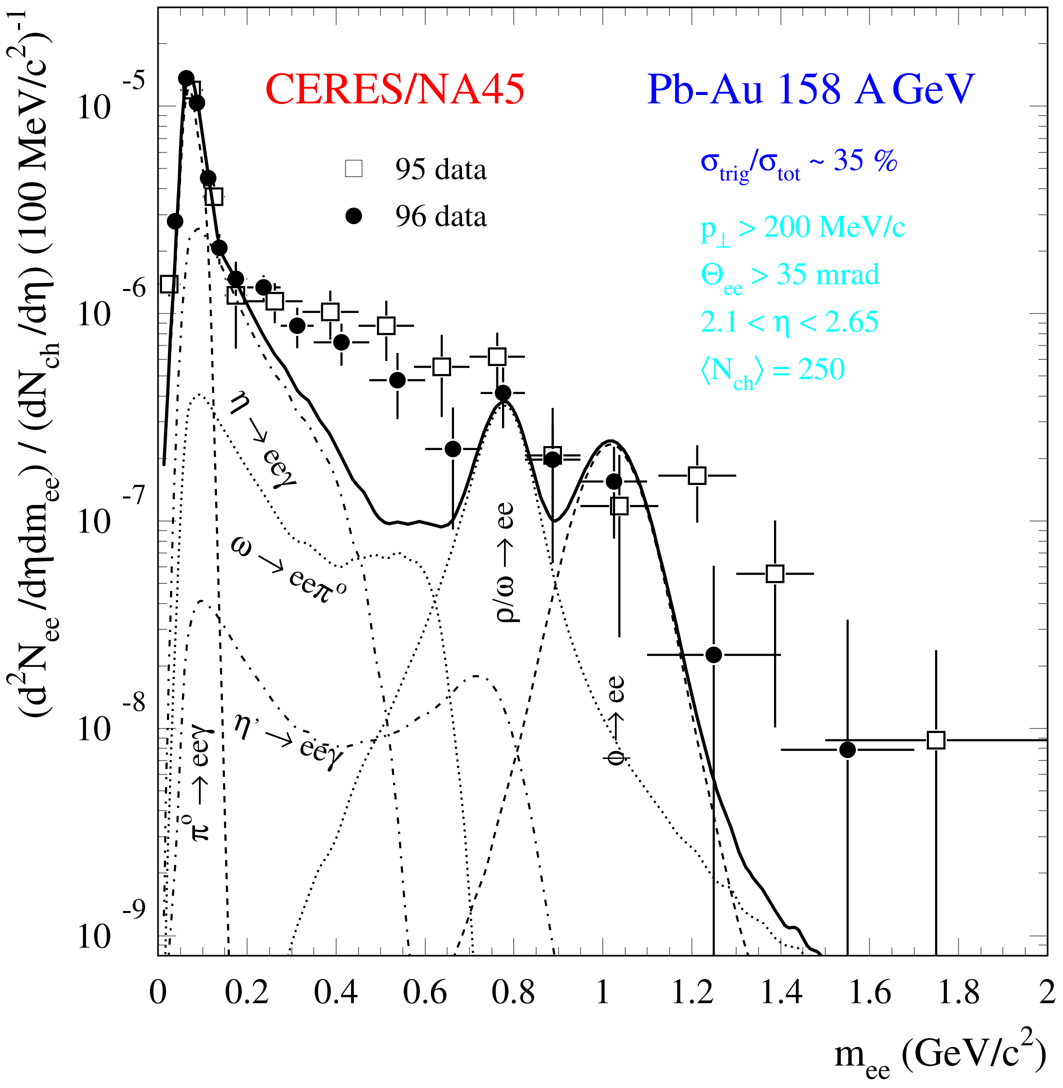

Figure 1.6: Inclusive e^+e^- mass spectrum seen by NA45. It is compared with the sum (solid line) of the expected contributions from hadron decays (dashed lines).

these ρ mesons would decay at a reduced mass [24]. Alternatively, the ρ mass could be broadened due to collisions with other baryons in the fireball. The collision rate in a typical heavy ion collision is such that this effect could be significant in the low-mass region of the dilepton spectra [25]. To conclusively determine the source of the enhancement NA45/CERES has upgraded its apparatus to allow greater statistics to be recorded with improved signal-to-background and mass resolution [26].

1.4.3 Charmonium Suppression

Charmonium suppression has been predicted to be an important signature of the phase transition to a QGP due to the nature of the Debye screening in the QGP phase [9]. The density in the QGP state is so large that the Debye colour screening radius is less than the radius of a bound $c\overline{c}$ pair. This makes forming such a pair very difficult, with most charm quarks pairing with up or down quarks to form D mesons. There are, however, hadronic processes which can lead to a depletion of charmonium in heavy ion collisions. Rescattering processes such as

$$J/\psi + \pi \rightarrow \mathrm{D}\overline{\mathrm{D}}\mathrm{X}$$

will cause significant depletion in the dense environment of a heavy ion collision.

NA50 has studied J/ψ suppression in Pb-Pb collisions. For peripheral collisions the suppression is in agreement with the trend of nuclear absorption determined from proton, oxygen and sulphur beam data from NA38 and NA51 [27]. Central Pb-Pb collisions show an additional suppression, which is shown in figure 1.7 by plotting the ratio of the J/ψ to Drell-Yan cross-sections divided by the nuclear absorption function. The mean nuclear path length, L, [28] is a measure of centrality [29], hence figure 1.7 shows not only that this additional suppression becomes greater with increasing centrality but that it is a threshold effect. The latter behaviour of the data is difficult to explain in hadronic scenarios.

1.4.4 Entropy per Baryon

In the phase transition to a QGP the liberated gluons provide the system with extra degrees of freedom. This will manifest itself as an increase in the specific entropy, S, of the system when compared to the hadronic scenario. Using lattice QCD it is possible to calculate the ratio of entropy to baryon number, B. Assuming a QGP consisting of up, down and strange quarks plus gluons, the ratio S/B was found

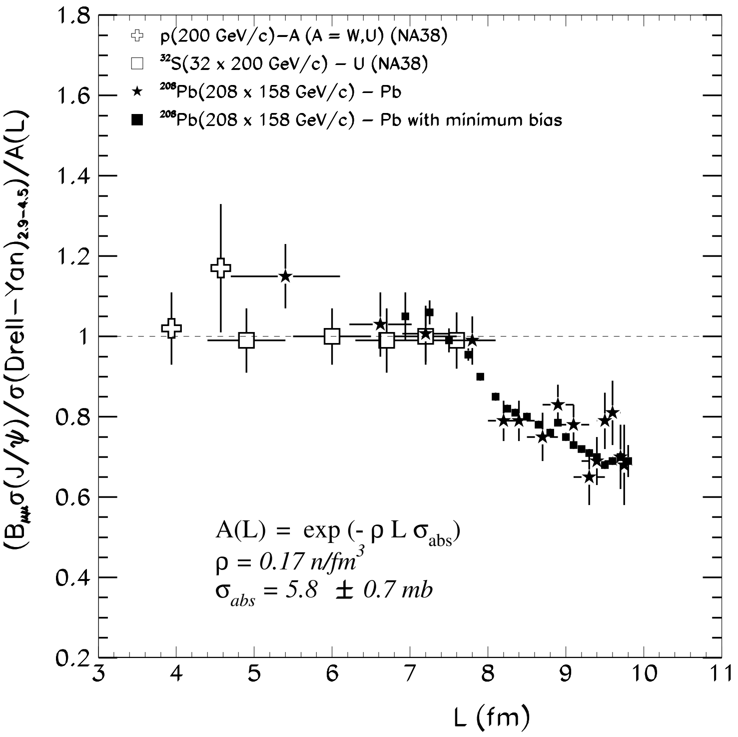

Figure 1.7: NA50 and NA38 $\sigma_{J/\psi}/\sigma_{DY}$ ratios divided by the nuclear absorption function determined from NA38 and NA51 data. L is the mean nuclear path length.

to be at least twice that in the hadron gas case for conditions typically found in experiments [15].

The entropy per baryon can be measured experimentally from charged particle multiplicities. Experiment EMU05 measured the charge asymmetry D_Q defined by

$$D_Q = \frac{N^+ - N^-}{N^+ + N^-}$$

where $N^{+(-)}$ is the number of positively (negatively) charged particles. Assuming that the only charged particles are protons, anti-protons and pions, with equal numbers of π^+ and π^-, $N^+ - N^-$ can be regarded as B while $N^+ + N^-$ is S. The EMU05 result of [17]

$$D_Q = 0.088 \pm 0.007 \simeq \frac{B}{S}$$

is in good agreement with theoretical QGP predictions of 0.08-0.09 [30] but cannot be explained by hadronic models.

1.5 Strangeness Production and Enhancement

It has been predicted that the production of strangeness in ultra-relativistic nucleus-nucleus collisions is a useful probe of the fireball produced in such a collision [16]. The weak interaction, the only one which can change quark flavours, is typified by a reaction time of 1×10^{-12} seconds or more [7]. The fireball of a heavy ion collision has a lifetime of 2-3×10^{-23} seconds [17], so the amount of strangeness produced in the collision will be preserved.

Firstly, consider the situation in which a heavy ion collision does not produce a QGP, so that the central fireball will be hadron gas. Here, strangeness production occurs through primary reactions like

$$pp \rightarrow p\mathrm{K}^+\Lambda,$$

$$pp \rightarrow pp\mathrm{K}^+\mathrm{K}^-$$

and

$$pp \rightarrow pp\Lambda\overline{\Lambda}.$$

In addition secondary interactions, such as

$$\pi^- p \rightarrow \Lambda\mathrm{K}^0$$

and

$$\pi^+\pi^- \rightarrow \mathrm{K}^+\mathrm{K}^-$$

can also produce strangeness. The primary reactions require threshold energies of 670 MeV, 990 MeV and 2.23 GeV respectively. As these are the lowest energy hadronic reactions which produce strangeness, it can be seen that the rate of strangeness production is quite low in a hadron gas. The time for a hadron gas fireball to reach strangeness equilibrium is 10-100 times greater than the lifetime of the fireball, therefore strangeness production is limited. This hadronic scenario will still give an enhancement relative to proton induced reactions but, as it is more difficult to produce strange particles of greater strangeness content, this enhancement should decrease for multi-strange particles [31].

In the case of a QGP fireball, strangeness equilibration occurs in about the lifetime of the fireball, primarily through the reaction

$$gg \rightarrow \mathrm{q}\overline{\mathrm{q}}$$

Initially light $\mathrm{q}\overline{\mathrm{q}}$ pairs are suppressed due to the lowest energy u and d quark states being occupied by the quarks from the heavy ions[1], while all the s quark states are available. Also, the effect of the factor $e^{-m_s/T}$, which usually inhibits $\mathrm{s}\overline{\mathrm{s}}$ production, is reduced by the high temperature of about 200 MeV and the reduction in m_s caused by the partial restoration of chiral symmetry. The combination of these two factors results in a relatively high production rate for $\mathrm{s}\overline{\mathrm{s}}$ pairs. This reaction dominates over

$$\mathrm{q}\overline{\mathrm{q}} \rightarrow \mathrm{s}\overline{\mathrm{s}}$$

due to the high gluon density, several hundred gluons in a QGP the size of a heavy ion collision fireball [32]. When hadronisation occurs the presence of strange quarks will lead to the formation of strange hadrons. The abudance of strange quarks should make the formation of Ξ^- baryons, consisting of dss, and Ω^- baryons, consisting of sss, (and the corresponding anti-particles) much easier relative to Λ baryons (uds) thereby giving larger enhancements for increasing strangeness content [33].

Therefore, a strangeness enhancement in a QGP, compared with a hadron gas, would manifest itself in increased yields of strange hadrons. Measuring the yields of such hadrons, especially hyperons (and corresponding anti-hyperons) such as Λ, Ξ and Ω, and their distributions should determine whether or not a QGP has been formed.

[1] This is true for the SPS which has high stopping. For the LHC, for example, this effect is negligible.

The WA85 experiment studied strangeness production in S-W collisions[2] [34] while WA94 studied S-S [35]. Their results for Λ, $\overline{\Lambda}$, Ξ^- and $\overline{\Xi}^+$ hyperons are shown in figure 1.8. The strangeness enhancement is defined as the double ratio $\frac{(Y/h^-)_{S-A}}{(Y/h^-)_{p-A}}$ where Y is the yield of the strange baryon, h^- is the corresponding yield of negative non-strange hadrons originating in the target and A is the target nucleus (tungsten for WA85 and sulphur for WA94). The Λ and $\overline{\Lambda}$ hyperons, with $|S| = 1$, show an enhancement of a factor of about 2.7 while the Ξ^- and $\overline{\Xi}^+$ hyperons, with $|S| = 2$, are enhanced more, by a factor of about 3.8 (WA85) and 3.4 (WA94) [36, 37].

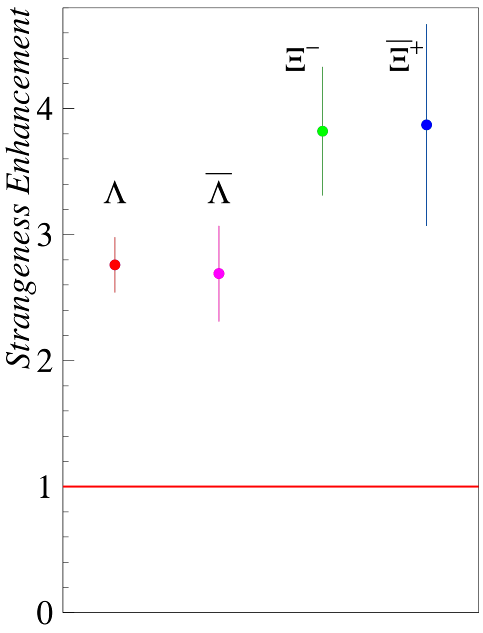

(a) WA85

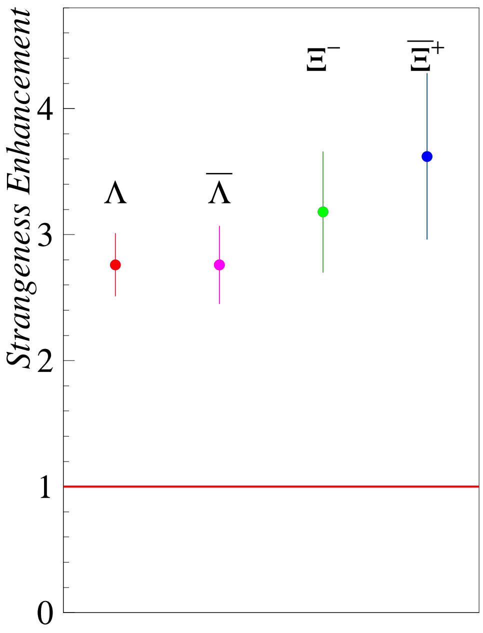

(b) WA94

Figure 1.8: Strangeness enhancements observed by a) WA85 and b) WA94. See text for details.

[2]WA85 was the first experiment to observe multistrange baryons in heavy ion collisions.

1.6 The WA97 Experiment

WA97 [38] was designed to continue the search for strangeness enhancement into Pb-Pb collisions, observe triply strange Ω baryons and to measure strangeness production as a function of centrality. Specifically WA97 studys the following weak decays (and the corresponding charge conjugate decays)

$$\mathrm{K}_s^0 \rightarrow \pi^+\pi^-,$$

$$\Xi^-(\Omega^-) \rightarrow \Lambda + \pi^-(\mathrm{K}^-)$$

and

$$\Lambda \rightarrow \mathrm{p} + \pi^-$$

As mentioned previously, in order to determine whether there really is an enhancement of strangeness requires some form of control experiment, one in which a QGP is *not* formed. Though p-p interactions may seem, at first glance, the ideal choice, the only practical proton target is liquid hydrogen. With the apparatus used by WA97 requiring a small target, the low density (0.07 gcm^{-3}) of liquid hydrogen leads to trigger rates which are too low. As with WA85 and WA94 before it, WA97 used a proton beam incident on the heavy ion target as a control in 1995, however there are nuclear effects which may complicate the analysis. Specifically, the Cronin effect [39], in which the incident proton undergoes multiple scatterings from nucleons in the target *before* the inelastic collision which produces most of the observed particles, may influence the yields of strange particles. To minimise these effects, in 1996 WA97 performed a p-Be run, the lightest system that could be used with the WA97 apparatus. This also has the benefit of providing a cross-check of the p-Pb data. With the closure of the CERN West Area, WA97 has been superseded by NA57 [40], which had its first (p-Pb) commisioning run in 1997 and will run until the end of 2000.

1.7 Summary

Studying the properties of the QGP is important not only in particle physics, where it is a test of QCD, but also in astrophysics, in connection with neutron stars and the early universe. It is believed that the dense, high temperature conditions found in ultra-relativistic heavy ion collisions are suitable for the formation of the QGP in the laboratory. Of the many methods for detecting a QGP the one chosen by the WA97 collaboration is strangeness enhancement, with analysis of the 1995 Pb-Pb and p-Pb data showing such an enhancement [41].

Chapter 2

The WA97 Experiment: Apparatus And Trigger.

2.1 Introduction

The purpose of the WA97 experiment was to investigate the central fireball produced in lead-lead collisions and to look for evidence of the formation of a QGP phase. In order to achieve this the WA97 collaboration chose to study strange particles, particularly hyperons (see Chapter 1). This chapter will describe the experimental set-ups and triggers that were employed in the 1995 lead-lead run and the 1996 proton-beryllium control run.

2.2 Experiment Requirements

2.2.1 Beam

The CERN Super Proton Synchroton (SPS) produces a beam of lead ions whose momentum is 158 GeV/c per nucleon. This beam strikes a lead target and it is believed that this beam energy is sufficient to create a central fireball hot and dense enough for QGP formation to occur.

When accelerating protons the SPS provides a beam of 450 GeV/c momentum. To obtain a proton beam equivalent to the lead beam a 400 mm thick beryllium (secondary) target was placed in the beam at the point where the beam is extracted from the SPS (not to be confused with the main beryllium target, to be described in section 2.4). Using dipole steering magnets, quadrupole focussing magnets and collimators a secondary proton beam of 158 GeV/c was produced and directed onto the main target. The interaction between the 450 GeV/c beam and the secondary target also produces particles other than protons, however, which leads to contamination of the secondary beam. This contamination consists primarily of pions which form 60% of the beam. These are vetoed in the trigger by using a pair of differential Čerenkov detectors [42] (see section 2.7).

2.2.2 Centrality

As described in Chapter 1, QGP formation is likely only in central events, which means triggering on high multiplicity events. Even then not all the particles will originate from the central fireball. Restricting the detector to particles with central rapidities, $2.4 < Y_{LAB} < 3.6$ for hyperons, will remove particles from the target/projectile remnants. Particles created in the fireball will also have a higher p_T than those of the target/projectile remnants, leading to the requirement that only particles with $p_T \geq 0.4$ GeV/c are detected.

2.2.3 Events

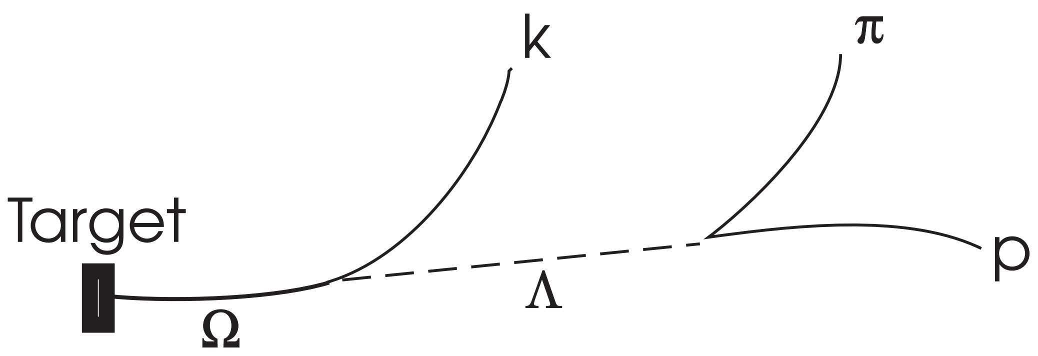

Figure 2.1: Schematic diagram showing the decay of an Ω hyperon.

To determine whether strangeness has been enhanced requires studying the following weak hyperon decays (and the associated anti-particle decays)

$$\Xi^-(\Omega^-) \rightarrow \Lambda + \pi^-(\mathrm{K}^-)$$

and

$$\Lambda \rightarrow \mathrm{p} + \pi^-$$

Good tracking within a magnetic field is needed to determine the four-momenta of the decay products, which then allows their tracks to be reconstructed (and extrapolated back towards the target) and decay vertices to be found. Figure 2.1 shows the decay topology of an Ω hyperon, where the Λ hyperon, being neutral, is not detected and is inferred from the four-momenta of the p and the π.

If there are few tracks, as in p-Be, this track reconstruction is relatively straightforward. With each Pb-Pb collision, however, producing several hundred charged tracks, the potential for reconstructing spurious Ξs and Ωs is very high. Fortunately the narrow kinematic window of the detectors described above reduces the number of charged tracks recorded in a typical Pb-Pb interaction to about 20.

2.3 The OMEGA Spectrometer

The OMEGA spectrometer consisted of a superconducting magnet whose two Helmholtz coils produced a magnetic field of 1.8 T. The target and most of the detectors for track identification were placed inside the 36m^2 region of field produced by the magnet. Figures 2.2 and 2.3 show the detector layouts for the 1996 p-Be and 1995 Pb-Pb runs, respectively. For all runs, data were taken for both field polarities. Although the system is symmetric, reversing the field is important to reduce residual systematic errors in the fine alignment of the detectors.

A useful system of co-ordinates is that which is defined relative to the centre of the OMEGA spectrometer. In this system, the beam crosses the $x = 0$ cm ($x_\Omega = 0$ cm) plane at $y_\Omega = 0$ cm and $z_\Omega = -0.5$ cm. The beam travels along the x-axis of this system. The main component of the magnetic field is in the OMEGA z-direction.

2.4 The Target

For the 1995 lead run the target was positioned at $x_\Omega = -60$ cm. Its thickness was chosen to be 1% of an interaction length, which corresponds to a thickness of 0.4 mm.

The beryllium target used for the 1996 proton run was 3.2 cm long giving an interaction length of 8%. This target was positioned at about $x_\Omega = -90$ cm.

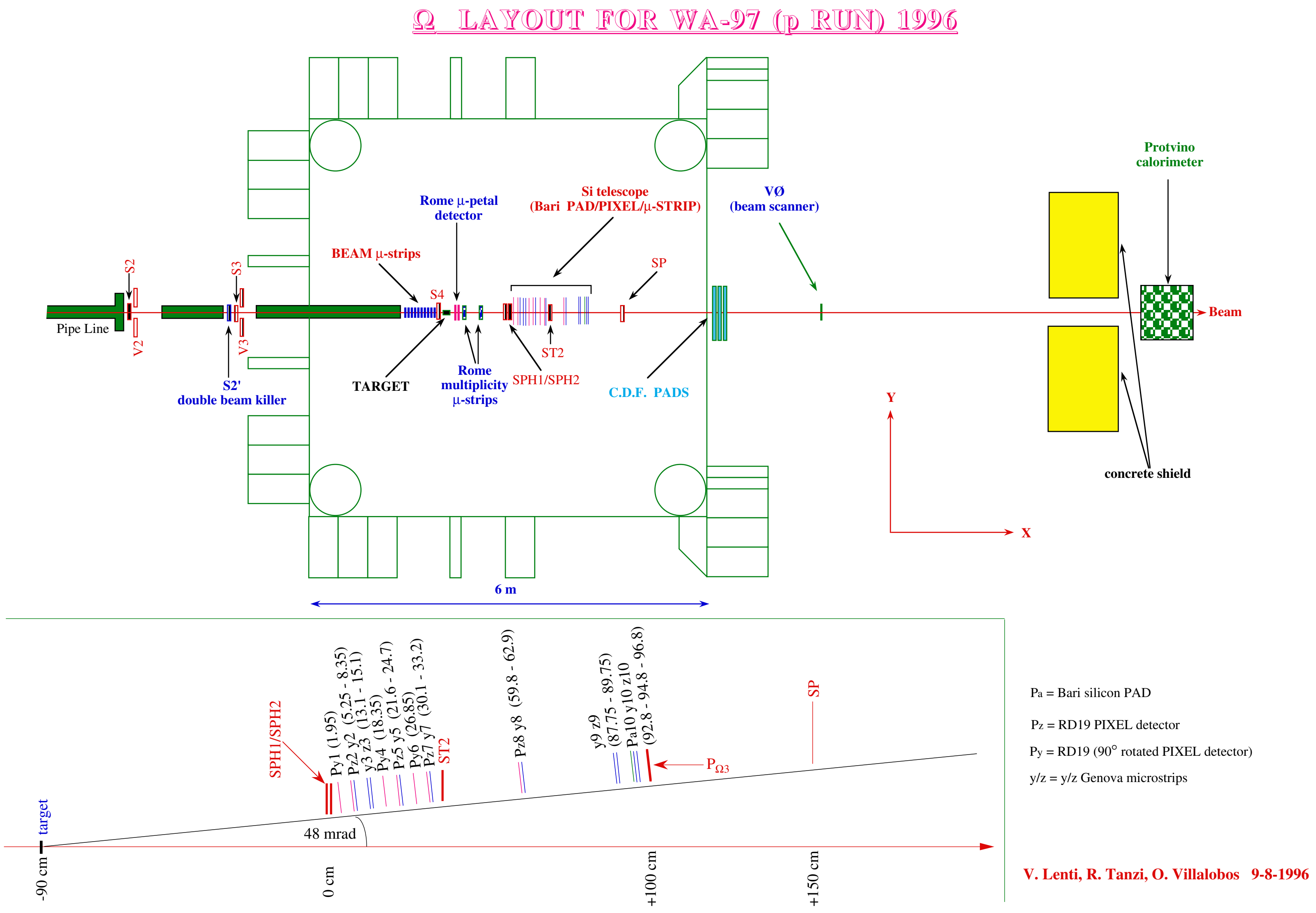

Figure 2.2: The WA97 experiment layout for the 1996 p-Be run.

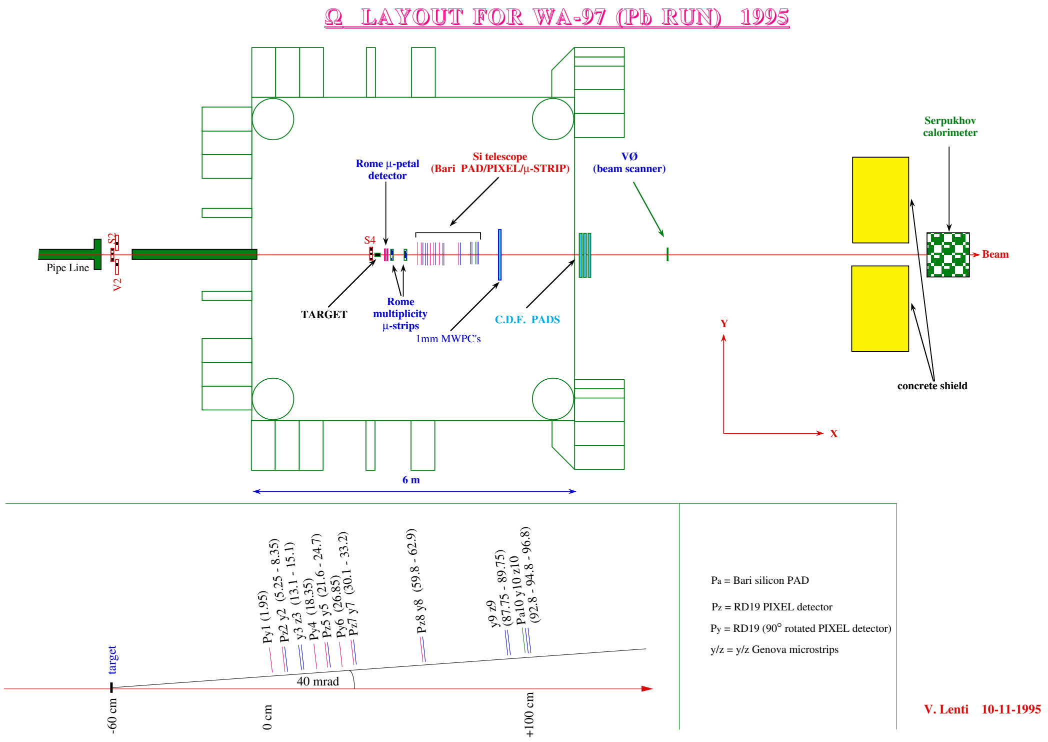

Figure 2.3: The WA97 experiment layout for the 1995 Pb-Pb run.

2.5 The Detectors

2.5.1 Tracking

The primary detector of the WA97 experiment was the silicon telescope, which was the main tracking system [43]. This detector was split into two sections and was composed of silicon based detectors. The main section, 30 cm in length and called the compact part, consisted of 5 microstrip planes (whose strips had a pitch of 50 μm) and 6 planes of silicon pixels (with pixel size 75 $\times$ 500 μm^2). This was placed 60 cm downstream of the target for the 1995 Pb-Pb run, to achieve the optimum balance between having a large number of tracks and having a high track reconstruction efficiency, and was positioned above the beam, inclined at 40 mrad in order to point back at the target. This positioning, combined with the 5 $\times$ 5 cm^2

active cross section of each plane, meant that the telescope occupied the kinematic window described previously (see page 25). To occupy the same kinematic window during the 1996 p-Be run, the telescope was positioned ~90 cm from the target, inclined at 48 mrad. Of the microstrip planes four had their strips orientated in the y-direction with the remaining plane orientated in the z-direction, in order to get both y and z information. Similarly, three pixel planes were orientated in such a way so that their resolution was greatest in the y-direction, while the other three were rotated by 90^o with respect to the y-planes to improve z resolution.

To further improve the tracking, additional microstrip and pixel planes were installed, together with three Multi-Wire Proportional Counters, downstream of (and on the same axis as) the compact part of the silicon telescope to act as a lever arm. Whereas the silicon detectors were situated just behind the compact part of the telescope (and as such were the second section of the telescope), the MWPC's were placed just outside the magnetic field, 4 m from the target. The MWPC's used had pad cathode readout, hence they were called *pad chambers*.

2.5.2 Beam Tracking

The high track multiplicity and thin target in Pb-Pb data taking allow the primary interaction vertex to be determined by tracing all the tracks back to the target plane. The point at which most of the tracks converge is taken as the primary vertex. In p-Be the number of tracks is typically one or two which, coupled with the large size of the target in x, requires a different method for finding the primary vertex. By placing microstrip detectors in the beam just upstream of the target the track of the beam particle can be found and intersected with the track(s) found in the main detectors (for more details of the vertex finding procedure see subsection 3.2.2). This *beam telescope* consisted of five pairs of microstrip planes spaced 11 cm apart, with one y-plane and one z-plane in each pair.

2.5.3 Multiplicity

In addition to tracking the WA97 apparatus also required detectors to measure the event multiplicity in the Pb-Pb runs, with three planes of such detectors being situated just downstream of the target. The first of these consisted of six scintillator petals, arranged around the beam axis as shown in figure 2.4. The petals formed part of the trigger system, which will be described in section 2.6. For a detailed, offline, investigation of the multiplicity in the event two planes of microstrips were installed just behind the petals, as shown in figure 2.4, with 34% azimuthal coverage. The first of these planes measured the multiplicity in the pseudorapidity range $2 \leq \eta \leq 3$ while the second sampled in the range $3 \leq \eta \leq 4$.

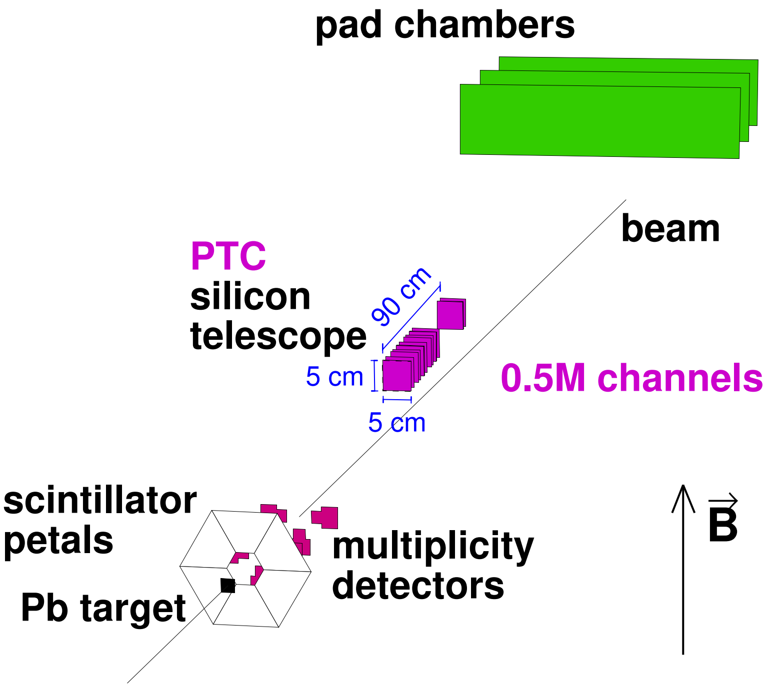

Figure 2.4: The layout of the WA97 detectors in the OMEGA magnet, for Pb-Pb collisions.

2.5.4 The Pixels

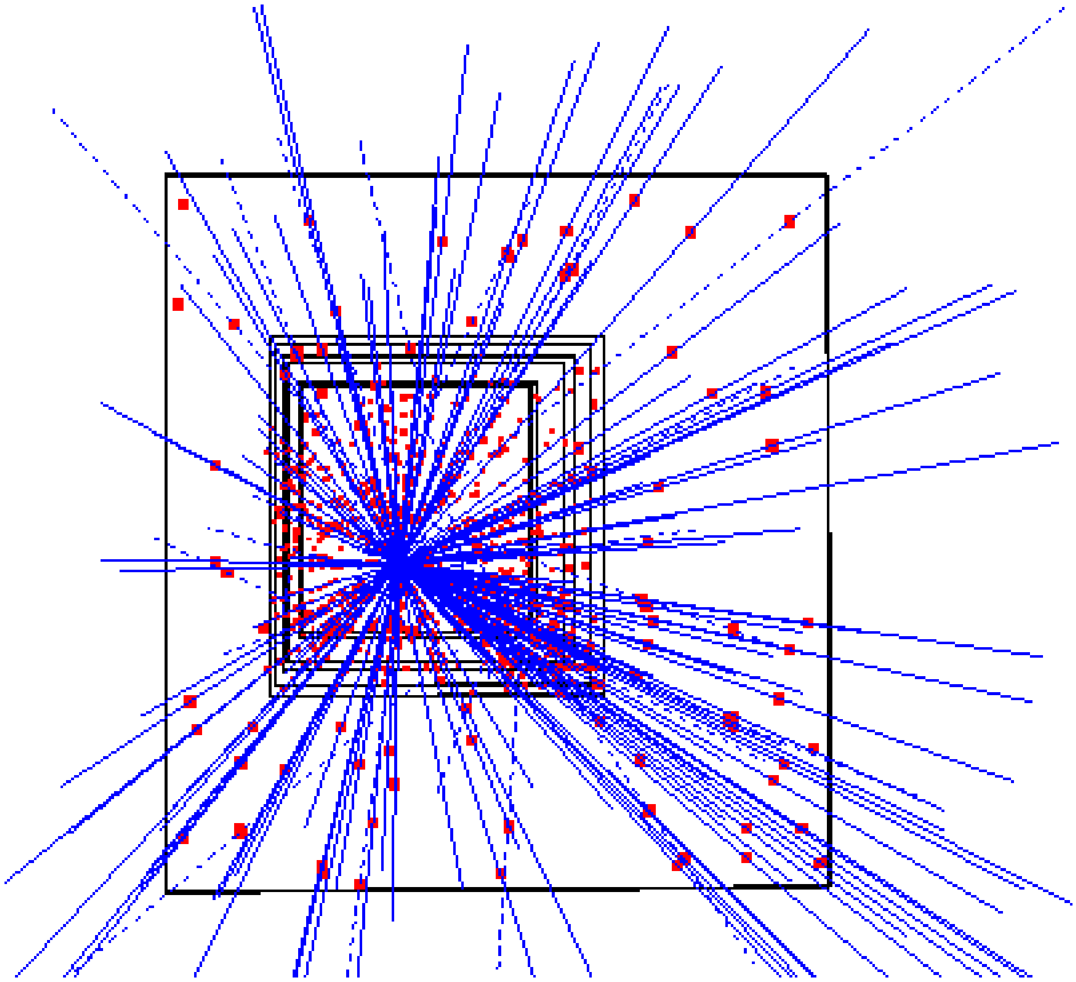

Figure 2.5: A view down the telescope, showing 153 reconstructed tracks. This data was taken without magnetic field and represents using only 0.2% of the 72K channels provided by each plane.

As previously mentioned, the main detectors of the WA97 experiment were the silicon pixels[1]. Developed in conjuction with the CERN RD19 group, the pixel planes are built up from *ladders* [44]. Each ladder consists of a matrix of 96 columns and 64 rows of rectangular diodes, which are the pixels, that have been ion-implanted on a high-resistivity ($> 5\mathrm{K}\Omega\mathrm{cm}$), n-type silicon substrate. This gives pixels of dimensions $75 \times 500\ \mu m^2$ and thickness 300 μm. In order to ground the pixels,

[1]In fact, WA97 was the first experiment to successfully use silicon pixels.

each pixel is connected to a front-end amplifier on a read-out chip by a Pb-Sn solder bump, of diameter 38 μm. To do this for every pixel requires the bump-bonding of 6 chips, each containing 16 $\times$ 64 pre-amp cells and requiring a bias voltage (typically 40 $\rightarrow$ 70 V) to be applied to the rear side.

An *array* is formed by gluing six ladders onto a 380 μm thick ceramic substrate, with a few mm between each ladder. The ceramic substrate carries the bus lines for the electronics, the connections between these and the read-out chip bonding pads being achieved using ultrasonic bonding. Two such arrays are mounted face-to-face, a few mm apart and staggered by about 4 mm, as shown in figure 2.6. The staggering means that there exists a slight overlap between the ladders on one array and those of the other, resulting in the whole 5 $\times$ 5 cm^2 area being covered with sensitive pixels. The net result of this is that each pixel plane has more than 72,000 pixels, with the sensitive part of the planes having a thickness of about 1.7% of a radiation length and an overall detection efficiency of at least 95%.

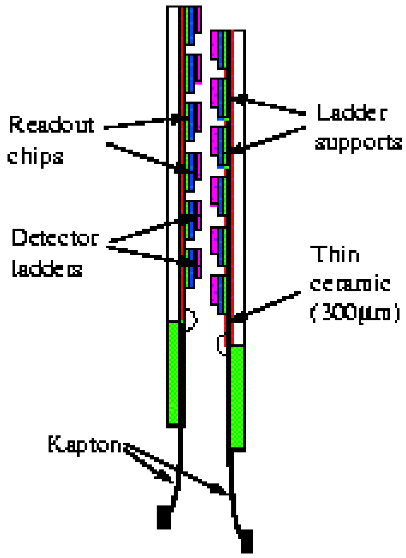

Figure 2.6: A schematic top view of a pixel plane.

2.6 The Trigger For The 1995 Pb-Pb Run

The purpose of the trigger used during the 1995 Pb-Pb run (figure 2.7) of the WA97 experiment was to select central Pb-Pb collisions, which constitute ∼30% of the inelastic cross section. The first trigger requirement was that there was a beam incident on the target for which a quartz Čerenkov counter, called S2 (see figure 2.3), was used. S2 identified an incoming particle as a Pb ion if the pulse height produced exceeded the threshold for Pb, since the pulse height is proportional to Z^2 [45]. The second component of the trigger was the centrality condition, using the petal detectors mentioned in section 2.5. A threshold was set on each petal corresponding to ∼10 mips (minimally ionizing particles), with the trigger condition being that the number of petals above threshold was at least 5.

Additionally, two further detectors were used to provide *veto* trigger signals. The first of these, a scintillation detector called V2 (see figure 2.3), had a hole cut in the middle through which passed the beam, if it was following its nominal trajectory. If the beam particle deviated significantly from its intended path, V2 was required to provide a signal in order for the event to be rejected. However, if the V2 threshold was set such that the passage of any charged particle through it caused a veto signal, then the rate of veto signals was very high. This resulted from δ-ray radiation produced by the Pb ions which were much more diffuse than the parent Pb beam. δ-ray radiation is a significant problem with Pb beams due to the nature of its cross section, σ_δ being proportional to Z^2 [45]. In fact, each Pb ion in the beam will produce ∼35 δ-rays, which led to the V2 threshold being set purely to veto Pb ions. The second veto counter, V0 (unlike V2, a quartz Čerenkov detector), was positioned downstream of the other detectors, as shown in figure 2.2. Its purpose was to veto events in which a high Z particle travelling along the beam axis existed on the downstream side of the OMEGA spectrometer.

The trigger just described provided a very high trigger rate, so high that the

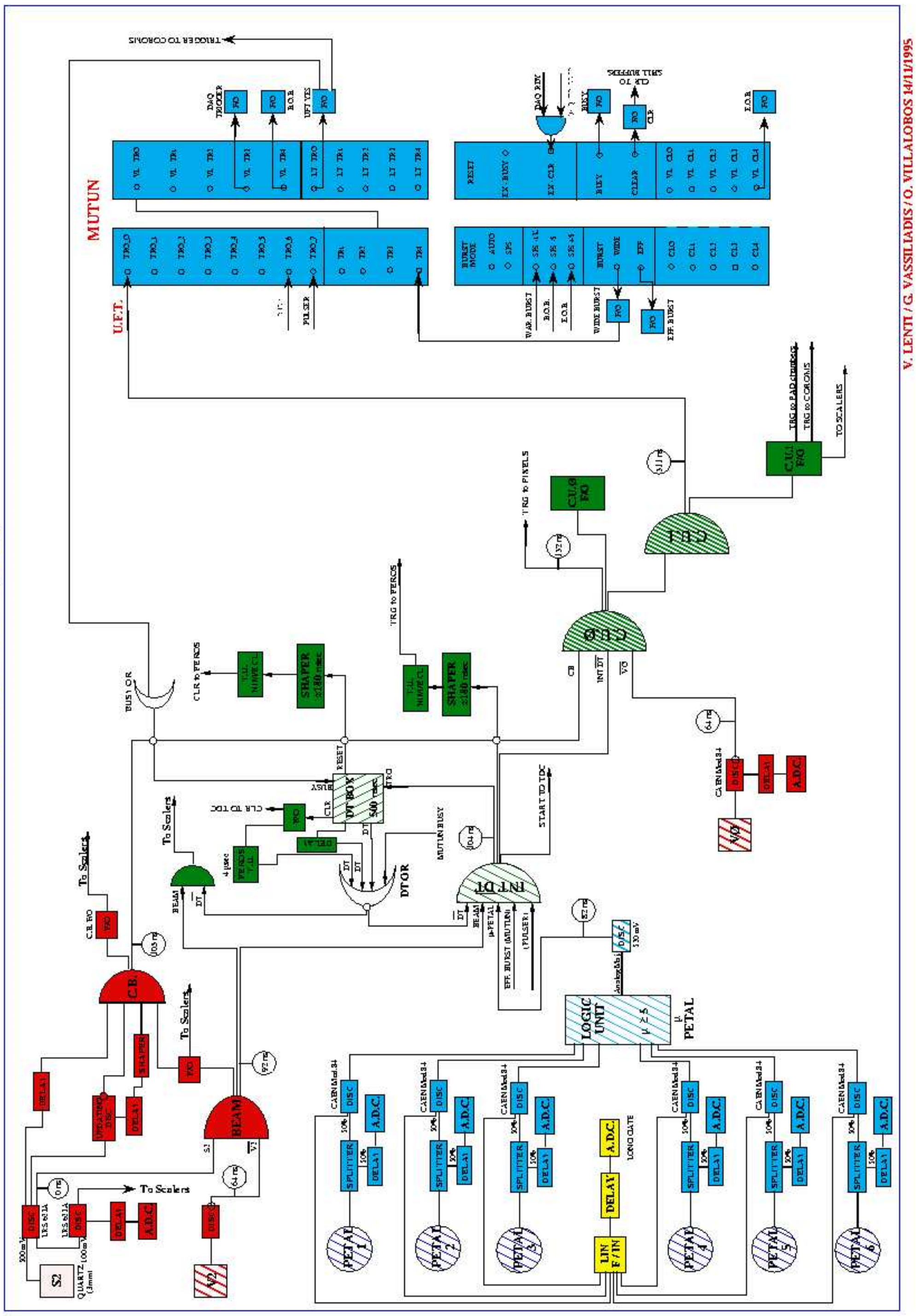

Figure 2.7: The WA97 trigger diagram for 1995 Pb-Pb run.

data acquisition rate was limited by time it took to read out all the detectors, which for 1995 Pb-Pb run was $\sim 1.4\ ms$ per event. This *dead time* accounted for 70% of the duration of a burst.

2.7 The Two-Track Trigger For The 1996 p-Be Run

The requirements for the trigger for proton beam data taking are somewhat different from those for the lead beam runs. A typical p-Be collision will produce only a few particles and only a small fraction of these will be hyperons whose decay particles pass through the detectors sufficiently to be reconstructed. As hyperons are the main particles of interest, the trigger needs to select those events in which a hyperon can be reconstructed. To do this scintillators were placed in front of the telescope, between the compact part and the lever arm and behind the lever arm (see figure 2.2). The trigger requirement was for at least two particles to enter the telescope and for at least one of these to traverse the whole telescope. Only one of the particles is required to go through the entire telescope as most of the protons produced in a hyperon decay will have most of the hyperon's momentum. It is much less likely, therefore, to be bent out of the telescope by the magnetic field than the mesonic decay products. Determining whether two particles have passed through a scintillator is done on the basis of the height of the produced pulse. For a single particle passing through the scintillator the pulse height has a Landau distribution. A single particle can, therefore, produce a pulse height in the tail of this distribution which is the same as the peak value of the two particle distribution. For this reason two pulse height scintillators, SPH1 and SPH2, were placed in front of the telescope as the likelihood that a single particle will produce pulse heights in the Landau tails of both scintillators is very low. Figure 2.8 shows the pulse heights measured in SPH2 plotted against those measured in SPH1. The concentration of events nearest the origin denotes the passage of a single particle while the other concentration is of two-track events. Events directly above or to the right of the single particle concentration have had one of the scintillators give a pulse height in the Landau tail, highlighting the need for two such scintillators.

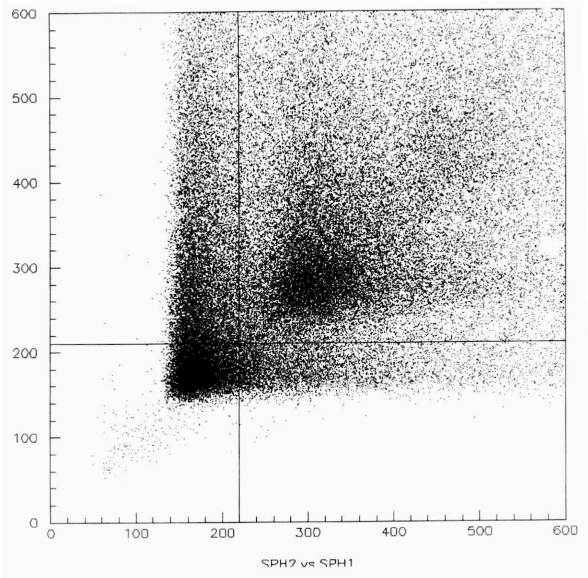

Figure 2.8: The pulse height measured in SPH1 against that measured in SPH2. Visible are the concentrations due to one-track and two-track events.

The two SPH scintillators and ST2, situated at the back of the compact part, were all the same size as the silicon planes, 5×5 cm^2. The scintillator placed behind the telescope, SP, was larger to allow for the curvature of a typical proton in the magnetic field.

The other component of the trigger concerns the beam. As mentioned previously, 60% of the secondary beam is pion contamination. By using ČErenkov Differential counters with Achromatic Ring focus (CEDARs) [42] this contamination was vetoed. As the beam particles passes through the gas inside the CEDAR it emits Čerenkov light. For a given refractive index protons and pions will emit at different angles leading to different sized rings. By varying the pressure of the gas, and hence its refractive index, the size of these rings could be controlled allowing one of the rings to be positioned over the CEDAR's eight photomultiplier (PM) tubes which formed a ring around the beam axis. Two CEDARs were used in order to have at least one at the correct pressure, as this could change with time. For the 1996 p-Be run the CEDAR pressure was set such that the proton ring fell on the PM tubes, meaning the trigger requirement was a positive signal from at least one of the CEDARs.

The beam was also required to reach the target area and be on-axis. To achieve this an S2 counter, this time with a scintillator element, and the V2 scintillator as mentioned in the previous section were used, though with different thresholds. A second veto scintillator V3 was also installed nearer to the target.

Chapter 3

Hyperon Decay Reconstruction

3.1 Introduction

As mentioned in Chapter 2, the WA97 experiment focused on the following weak decays (and the associated anti-particle decays)

$$\Xi^{-}(\Omega^{-}) \rightarrow \Lambda + \pi^{-}(\mathrm{K}^{-})$$

and

$$\Lambda \rightarrow \mathrm{p} + \pi^{-}$$

in order to determine whether the yields of strange particles had been enhanced, which might indicate the presence of a QGP phase. The first stage in the reconstruction involves matching two oppositely charged tracks together to form a Λ hyperon. To reconstruct a Ξ or Ω hyperon decay requires combining a Λ hyperon with a third track. The focus of this chapter will be the selection criteria for the p-Be Λ hyperon sample, as these were determined by the author. The selection criteria for the Ξ and Ω hyperon samples as well as those for all the hyperon types for the 1995 Pb-Pb data will de described briefly for completeness.

3.2 Λ Reconstruction For 1996 p-Be

3.2.1 V^0 Candidate Selection

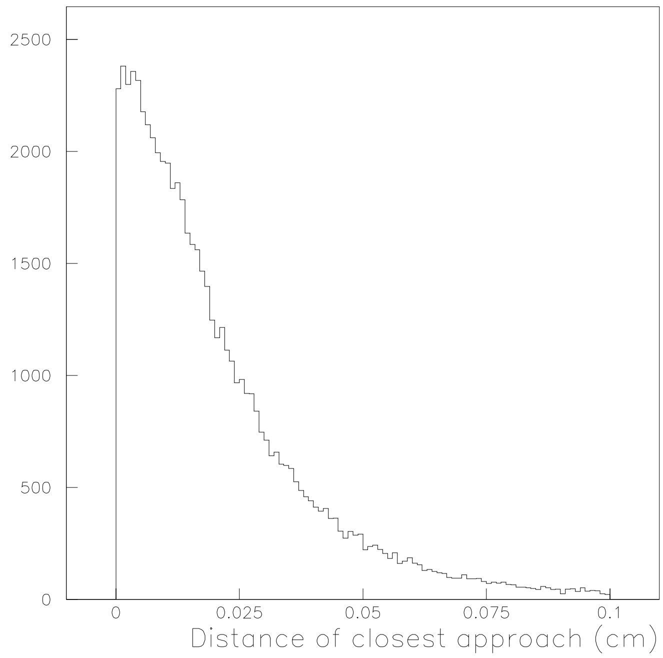

Figure 3.1: The distribution of the distance of closest approach for events satisfying all other selection criteria, except the Λ hyperon mass cut, for the 510 run sample.

Tracks are found in the raw data by the ORHION program and then traced back towards the target. The Λ hyperon selection begins by finding V^0 candidates from the reconstructed tracks, which is also performed by ORHION using loose criteria. The determination of the selection criteria was performed using the program ANALP96 to create ntuples with loose cuts. These could then be investigated and tightened using PAW [46]. To prevent the ntuples becoming too large this was done twice, firstly with a sample of 40 runs with very loose cuts. The cuts resulting from the analysis of this ntuple were then slightly loosened and used to produce a second ntuple, this time based on a sample of 510 runs. The analysis of this second

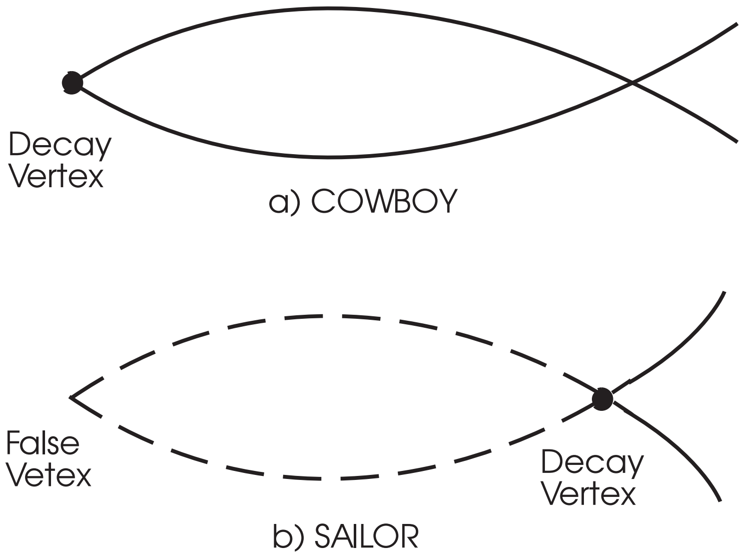

Figure 3.2: V^0 decay topologies in the bend plane of the magnetic field. It can be seen that every cowboy decay has an accompanying sailor vertex and that every sailor decay has a 'ghost' cowboy vertex.

ntuple produced the final Λ hyperon selection criteria. These were then included in ANALP96 and an ntuple of Λ and $\overline{\Lambda}$ hyperon candidates was produced.

V^0 candidates are found by examining each possible combination of a positive and a negative track, requiring that the distance of closest approach between the two tracks is less than 0.1 cm. Figure 3.1 shows the distribution of the distance of closest approach for the 510 run sample with the cut falling in the tail of the distribution. The decay vertex is taken half way between the tracks at the point of closest approach. Depending on the initial momentum of the decay products they will either be bent towards each other (a *cowboy*) or their tracks will diverge (a *sailor*), see figure 3.2. As the decay products remain close in space for longer the telescope favours cowboys, which leads to 70% of V^0 candidates being cowboys. By requiring cowboy decay topology the background can be significantly reduced, since the spurious V^0 candidates from target tracks resemble sailors, without losing too many genuine Λ hyperon events.

In addition, the cowboy decay vertex must lie in the decay region, defined as begining approximately 40 cm ($x_\Omega = -50$ cm) downstream of the target and ending just before the telescope (see figure 3.3). Any V^0 decays occuring within the telescope will have fewer space-points on the tracks of its decay products, leading to a worse determination of their momentum. For this reason the decay region stops at the front of the telescope. The cut of $x_\Omega > -50$ cm is used due to the low acceptance for real V^0's that decay a long way from the telescope; any V^0 candidates below this cut are likely to be spurious, caused by the chance crossing of two tracks direct from the target. Figure 3.4 (a) shows the distribution of the x-position of the cowboy decay vertex plotted against q_T (defined on page 45) for the 40 run sample, with all cuts applied except for the cut on the cowboy vertex position. The cut lies in the tail of the distribution, which is also the case for the 510 run sample, shown in figure 3.4 (b) with all cuts applied.

3.2.2 Primary Vertex Reconstruction

Further cuts are made on the sample of V^0 candidates, the first being that the V^0 comes from the target. This is achieved by performing cuts on the location of the primary interaction vertex. To calculate the position of the primary interaction vertex the beam telescope is used to determine the parameters of the beam particle. This beam track is traced forward towards the target and the point at which it intersects with the reconstructed V^0 or cascade from the main silicon telescope is taken as the interaction vertex. The intersection is done in two stages. Firstly the beam track and V^0 or cascade are intersected in the x-z plane, where both tracks are straight lines. This gives the x and z coordinates of the primary vertex. In the x-y plane the tracks are nearly parallel which makes intersection difficult. As this plane is the bend plane of the magnetic field the beam and cascade tracks

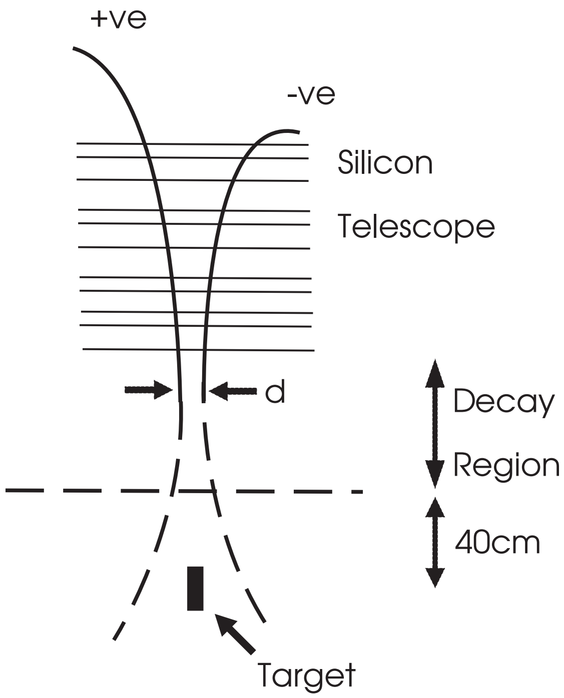

Figure 3.3: Schematic diagram of a V^0 decay showing the decay region. The solid track lines represent the tracks reconstructed in the telescope, the dashed parts represent the tracks traced back to the target (d is the distance of closest approach).

are parameterised using the equation of a circle. The y coordinate of the primary vertex is determined by substituting the x coordinate found in the x-z plane into the equation of the beam track. For events with more than one V^0 or cascade candidate the interaction vertex is calculated for each one and the resulting coordinates are averaged to find the primary vertex.

Once the position of the primary vertex has been found selection cuts can be applied. If the primary vertex position cannot be reconstructed the event is rejected. Due to the comparatively large target it is possible that the mean vertex position may change with time if there is fluctuation in the alignment of the beam. For this reason the mean vertex position for each run was calculated, with all vertex cuts being performed with respect to these means. In y and z the primary vertex must lie within 0.3 cm of the mean for the run from which the event originates while

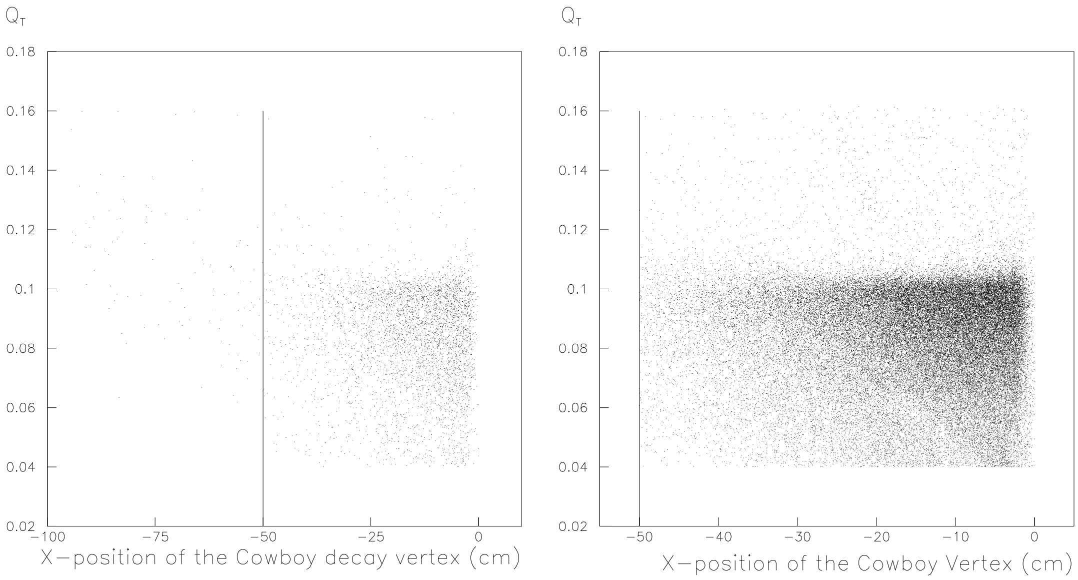

(a) (b)

Figure 3.4: q_T plotted against the x position of the cowboy vertex, for a) the 40 run sample and b) for the 510 run sample.

the cut in x is 5 cm from the mean. There is one further condition on the vertex which concerns the V^0. As described above, the y position on the primary vertex is actually the y coordinate of the beam track at the x and z of the intersection of the beam track and the V^0 in the x-z plane. It is possible, therefore, that the V^0 does not come from the primary vertex. To exclude V^0s not coming from the primary vertex the y position of the V^0 at the z of the vertex is required to lie within 0.3 cm of the y of the vertex. Figures 3.5 (a), (b) and (c) show the distributions of the differences in x, y and z between the vertex position reconstructed for an event and the mean for its run, for the 510 run sample. All the cuts have been applied except those on the variable plotted, which are shown as the vertical lines. Figure 3.5 (d) shows the difference between the y positions of the V^0 and the vertex, again for the 510 run sample. For all four, the distributions are peaked and centred at zero with the cuts falling in the tails of the distributions.

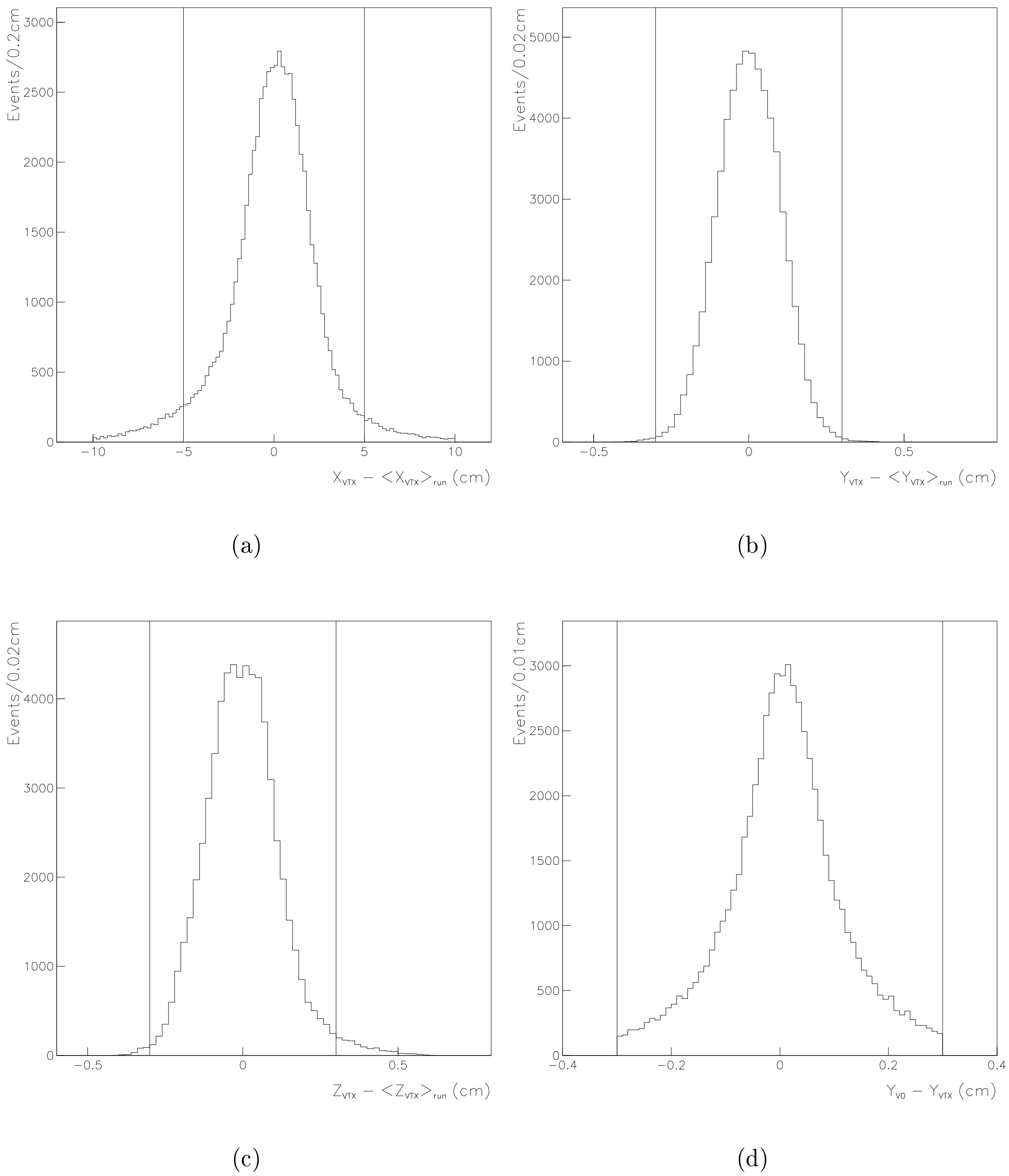

Figure 3.5: For the 510 run sample the differences between the reconstructed event vertex and the mean for that run in a) x b) y and c) z. Shown in d) is the difference in the y position of the V^0 and the vertex.

3.2.3 Λ Hyperon Selection

To mimic the trigger used for the p-Be data (see Chapter 2), from which the Λ hyperon sample is obtained, there are additional requirements on the decay tracks. The first of these is the requirement that at least one of the tracks traces through the sensitive area of both the SP and ST2 scintillators. The second condition is that both decay tracks trace through both the first and fourth pixel planes in the telescope.

Λ and $\overline{\Lambda}$ hyperons are selected from the V^0 sample on the basis of their Podolanski-Armenteros variable [47], α, and q_T.

$$\alpha = \frac{q_L^{lab}(+) - q_L^{lab}(-)}{q_L^{lab}(+) + q_L^{lab}(-)} \tag{3.1}$$

Equation 3.1, above, is the definition of α for a neutral particle decaying into a pair of oppositely charged particles, where the q_L^{lab} variables are the longitudinal momenta of the decay particles with respect to the direction of flight of the V^0. The magnitude of the momentum components transverse to the direction of flight of the V^0 for the two decay particles are the same (conservation of momentum) and is referred to as the q_T of the V^0 . For a more detailed description of the relation of α to q_T for different decays see Appendix A. By requiring $|\alpha| \geq 0.45$ most of the K^0 contamination was removed and demanding $q_T \leq 0.40$ GeV/c removes many spurious V^0 candidates.

Another source of contamination in the Λ hyperon sample comes from γ conversions within the detectors. These events are concentrated at low q_T, leading to the cut of $q_T \geq 0.040$ GeV/c. Figure 3.6 shows the Armenteros-Podolanski plot from the 40 run sample in which the broad band of γ conversion events at low q_T can be clearly seen. Secondary interactions in the detectors can occur which also provides a source of contamination. These can be seen in figure 3.7 (a), which plots q_T versus the x position of the *sailor* vertex for the 40 run sample, as the concentration of events at small positive x and low q_T. While figure 3.7 (a) would seem to indicate that these events have $q_T \leq 0.05$ GeV/c, using the 510 run sample shows that these events go up to $q_T = 0.065$ GeV/c. A simple q_T cut at this value would also remove a significant number of genuine Λ so this cut is restricted to events which have a sailor vertex in the range $3 < x_\Omega < 7$ cm.

The final selection criteria are the K^0 mass rejection cut and the Λ mass cut. Due to the lack of identification of the decay tracks, which prevents unambiguous rejection of K^0, the mass of the V^0 candidate is reconstructed twice, once assuming it was a K^0 and once assuming it was a Λ. Events with a K^0 mass close to the PDG value were rejected, the value of this cut being determined from the Armenteros-Podolanski plot of the 510 run sample (figure 3.8). Figure 3.8 shows the effect of the loose 15 MeV/c^2 cut that was applied when producing the ntuple for the 510 run sample. Based on this events were rejected if the reconstructed K^0 mass was within 30 MeV/c^2 of the PDG value for the K^0. Figure 3.9 shows the invariant mass distributions for Λ and $\overline{\Lambda}$ hyperons from the whole 1996 p-Be data after all cuts except for the Λ mass cut. Both distributions have very low backgrounds but are peaked at a mass $\sim$1 MeV/c^2 higher than the PDG value, as was the case with the 1995 p-Pb data. For this reason the cut of $\pm$15 MeV/c^2, chosen because of the clarity of the signal, was centred at 1.117 GeV/c^2.

3.3 Cascade Reconstruction For p-Be

The selection cuts described previously are designed to find Λ hyperons from the primary interaction. To find Λ hyperons from cascade decays requires slightly different cuts. The V^0 must, again, have cowboy topology, the requirement on the distance of closest approach is the same (less than 0.10 cm) though the q_T range is altered slightly, with $0.02 \leq q_T \leq 0.40$ GeV/c being required. The decay region is larger, with the x-position of the V^0 decay vertex required to be in the range $-80 < x_\Omega < 0$ cm. The tolerence on the M_Λ of the V^0 is $\pm$15 MeV/c^2 around the

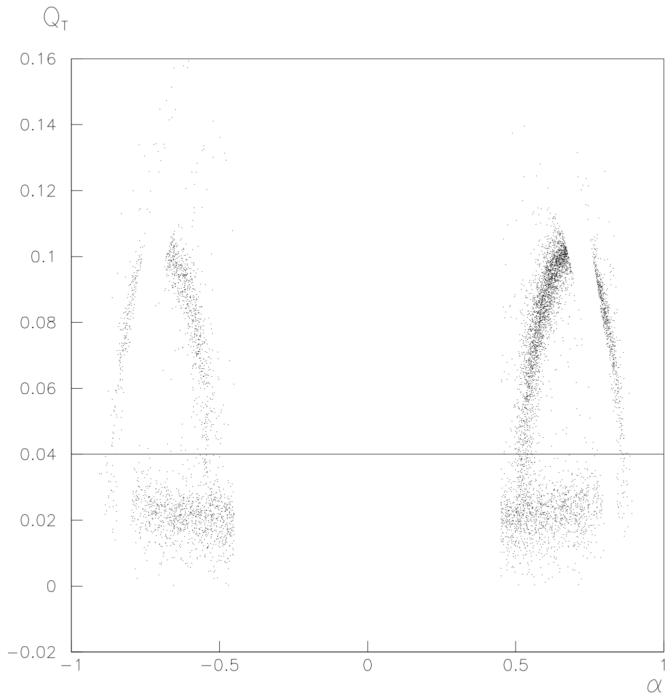

Figure 3.6: The Armenteros-Podolanski plot for events satisfying all selection criteria, except the Λ hyperon mass cut and q_T cut, for the 40 run sample.

PDG value for the Λ hyperon mass.

The distance of closest approach between the V^0 and the third track (a π or K) is also required to be less than 0.10 cm, with the cascade decay vertex in the region $-80 < x_\Omega < -2.5$ cm. The V^0 and the third track must also cross downstream of the decay vertex (*i.e.* be of cowboy topology). In the case of the V^0 being a Λ hyperon the third track must have negative charge while for a $\overline{\Lambda}$ anti-hyperon it must be positively charged. One of the three tracks is required to trace through the SP and ST2 scintillators while all three tracks must trace through the first and fourth pixel planes, again to simulate the two-track trigger. Although the decay regions for the V^0 and the cascade are the same, a causality condition that the x-position of the V^0 decay vertex is greater than that of the cascade decay vertex is imposed.

A cascade candidate is rejected if the event in which it is found does not have

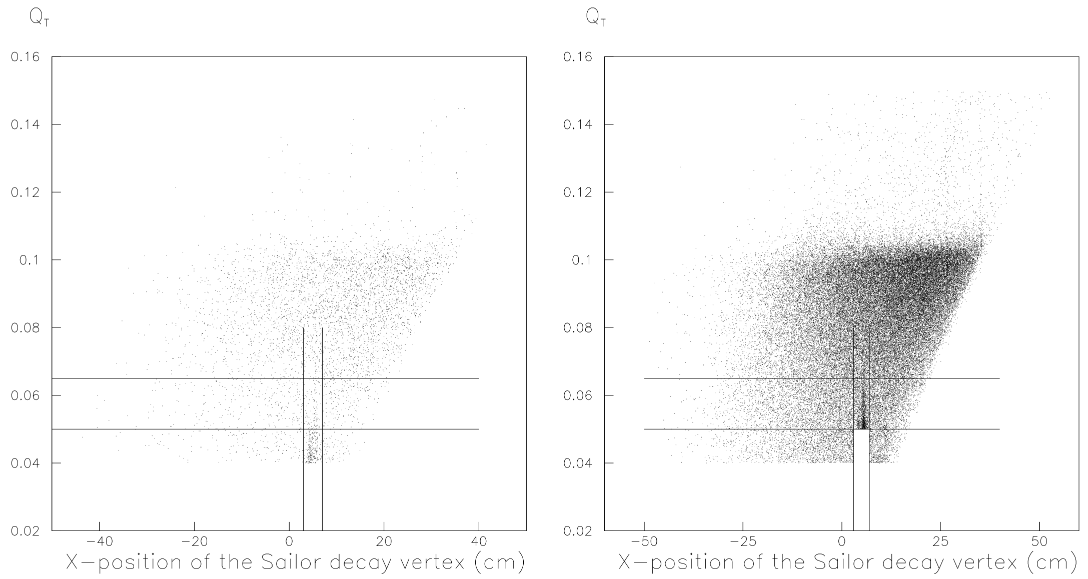

(a) (b)

Figure 3.7: q_T plotted against the x position of the sailor vertex, for a) the 40 run sample and b) for the 510 run sample.

a fully reconstructed beam track, which prevents the primary vertex from being found. The primary vertex must have its x position within 5 cm of -91.6 cm, its y within 0.4 cm of zero and its z must be less than 0.2 cm. The cascade is required to trace back to within 0.3 cm in y and 0.13 cm in z of this vertex. To exclude spurious cascade candidates the V^0 and the third track must not come from the primary vertex, with impact parameters in y greater than 0.14 and 0.4 cm respectively.

If a cascade decay is successfully reconstructed, there still remains the question of whether it is a Ξ or an Ω hyperon. Again, the lack of any particle identification makes it impossible to tell if the third track is a π or a K. So, as with the V^0, the cascade's mass and momentum are reconstructed twice, once assuming that the third track is a π and then assuming that it is a K. If the mass as an Ξ hyperon of the cascade is within 0.02 GeV/c^2 of the PDG Ξ hyperon mass then it is taken as an Ξ hyperon. If the Ξ hyperon mass lies outside this range further cuts are applied to determine whether the cascade is an Ω hyperon. The cascade must have

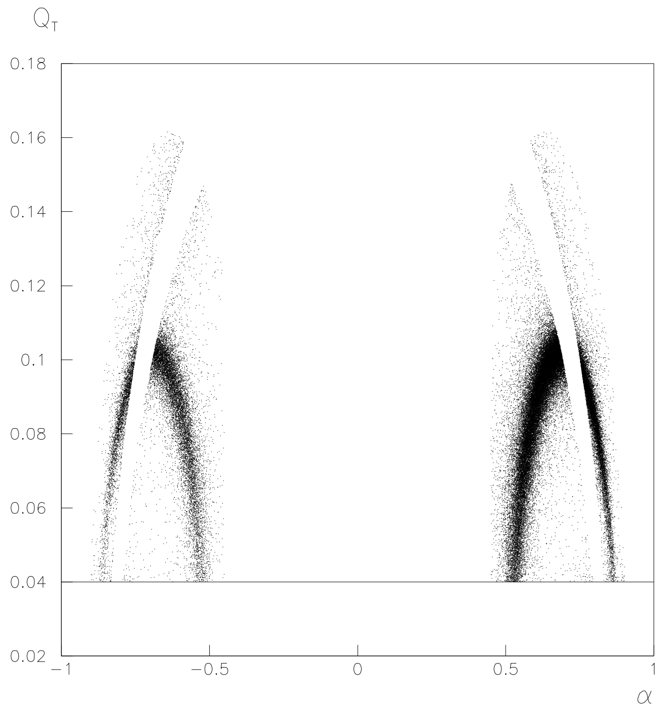

Figure 3.8: The Armenteros-Podolanski plot for events satisfying all selection criteria, except the Λ hyperon mass cut, final K^0 mass rejection cut and q_T cut, for the 510 run sample.

$|\alpha|$ between 0.2 and 0.6 and q_T greater than 0.12 GeV/c, while the Λ hyperon must have q_T greater than 0.032 GeV/c. The final selection for the Ω hyperon sample is a mass cut, with the Ω hyperon mass of the cascade being within 0.03 GeV/c^2 of the PDG Ω hyperon mass.

3.4 Hyperon Reconstruction For 1995 Pb-Pb

While the selection criteria for Pb-Pb are generally the same as those for p-Be there are, however, some differences. These stem mainly from the different detector geometries and different multiplicities of the two runs. The Pb target is thin enough to be treated as a single plane in x. By tracing all the tracks back to this plane the primary interaction vertex can be determined from the convergence of the majority of the tracks.

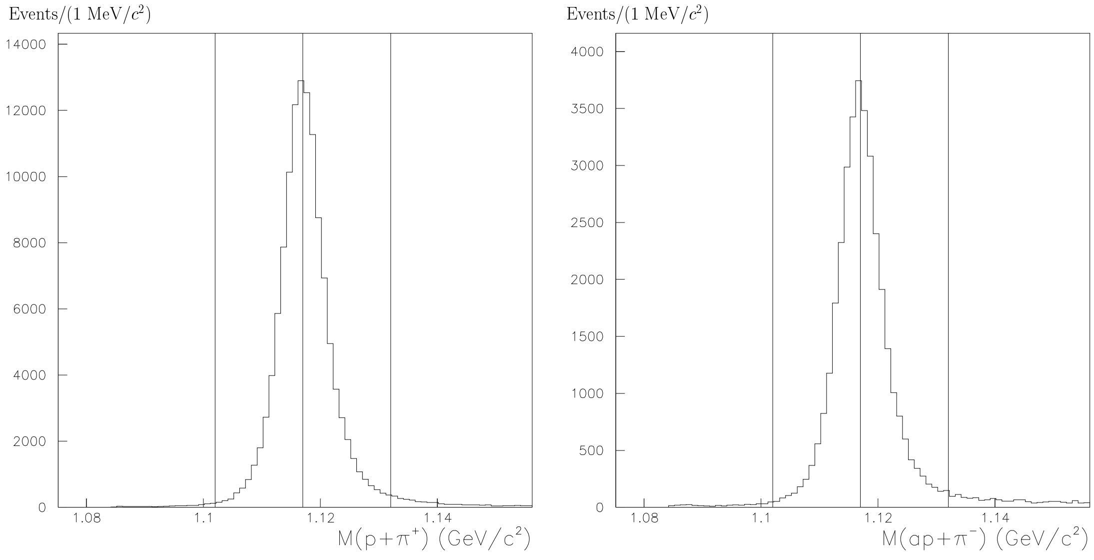

Figure 3.9: The a) Λ and b) $\overline{\Lambda}$ hyperon mass distributions for the whole 1996 p-Be data after all cuts except the final mass cut. Of the three vertical line in each plot the centre one is at 1.117 GeV/c^2 while the outer ones show the limits of the 15 MeV/c^2 cut.

3.4.1 Λ Hyperon Reconstruction

V^0 candidates are found by finding pairs of oppositely charged tracks. The distance of closest approach is required to be less than 0.06 cm. This is less than the p-Be value due to the greater likelihood of spurious V^0s in the higher multiplicity environment of a Pb-Pb collision. This also explains why the decay region, $-30 < x_\Omega < 0$ cm, occupies a smaller fraction of the distance between the target and the telescope.

The V^0 is required to trace back, in the target plane, to within an ellipse centred on the interaction vertex. This ellipse has a semi-major axis, which is in the bend plane of the magnet, of 0.15 cm and semi-minor axis of 0.10 cm.

From the V^0 sample the Λ and $\overline{\Lambda}$ hyperons are selected by demanding $|\alpha| \geq 0.45$ and $0.035 \leq q_T \leq 0.40$ GeV/c. The lower q_T cut is lower than for p-Be as there are relatively fewer γ-conversions in the data. The K^0 mass rejection cut is ± 30 MeV/c^2 of the PDG value. The reconstructed Λ or $\overline{\Lambda}$ hyperon mass must be within 10 MeV/c^2 of the PDG value for the Λ hyperon mass.

3.4.2 Cascade Reconstruction

For the Λ hyperons used in the reconstruction of cascades, the distance of closest approach is required to be less than 0.10 cm. As before the V^0 candidates must have cowboy topology and the decay region is $-30 < x_\Omega < 0$ cm. The allowed q_T range is the same as for the p-Be cascades, while the tolerance on the V^0 mass is $\pm$ 7.5 MeV/c^2 of the PDG value for the Λ hyperon mass.

In order to combine to form a cascade decay, the V^0 and the third track must come within 0.10 cm of each other. The resulting cascade decay vertex must have cowboy topology and lie in the region $-40 < x_\Omega < 0$ cm. There is also the causality condition that the V^0 decay vertex is downstream of the cascade decay vertex. For cascade decays the distance of the third track from the interaction vertex in the y-direction, B_y, must be greater than 0.5 cm while B_y must be less than -0.1 cm for the V^0. For the anti-cascades the opposite B_y values are employed (i.e. less than -0.5 cm and greater than 0.1 cm respectively). If both the V^0 and third track traced back to the same side of the interaction vertex this would violate the conservation of momentum.

Additionally, cascades must originate at the interaction vertex, for which they are required to trace back to within an ellipse defined by B_y of 0.2 cm and B_z of 0.1 cm. However some events do not have enough tracks for a well defined interaction vertex to be found. These events are not discarded since they contain a significant number, 5% of the final sample, of cascades. Cascade candidates in these events are then required to trace back to the target (i.e. a rectangle defined by B_y and B_z of 0.4 cm).

The cascade is taken as an Ξ hyperon if its reconstructed Ξ hyperon mass is within 15 MeV/c^2 of the PDG Ξ hyperon mass. If the cascade is not an Ξ hyperon but has a reconstructed Ω hyperon mass within 22.5 MeV/c^2 of the PDG Ω hyperon mass the cascade is classified as an Ω hyperon.

3.5 Summary Of Cuts For 1996 p-Be

3.5.1 Cuts For Λ Hyperon Reconstruction

1. At the V^0 vertex, the distance of closest approach is less than 0.10 cm.
2. The V^0 vertex lies in the region described by $-50 < x_\Omega < 0$ cm.
3. The decay must have cowboy topology.
4. One V^0 decay track must pass through the SP and ST2 scintillators.
5. Both V^0 decay tracks must pass through the first and fourth pixel planes.
6. The primary vertex must be reconstructed successfully.
7. The reconstructed primary vertex must lie within 0.3 cm in y and z and 5 cm in x from the mean position for that run.
8. The V^0 must trace to within 0.3 cm of the primary vertex in y.
9. $|\alpha| \geq 0.45$
10. $0.040 \leq q_T \leq 0.40$ GeV/c.
11. The sailor vertex of the V^0 must lie outside the region given by $3 < x_\Omega < 7$ cm for $q_T < 0.065$.
12. $M_{V^0} \neq M_{\mathrm{K}^0}(PDG) \pm 30$ MeV/c^2.
13. $M_{V^0} = 1.117$ GeV/$c^2 \pm 15$ MeV/c^2.

3.5.2 Cuts For Cascade Reconstruction

1. At the V^0 vertex the distance of closest approach is less than 0.10 cm.
2. The V^0 decay must have cowboy topology.
3. The V^0 decay vertex must lie in the region given by $-80 < x_\Omega < 0$ cm.
4. $0.02 \leq q_T(V^0) \leq 0.40$ GeV$/c$
5. $M_{V^0} = M_\Lambda(PDG) \pm 15$ MeV$/c^2$
6. At the cascade decay vertex the distance of closest approach is less than 0.10 cm.
7. The cascade decay vertex lies in the region described by $-80 < x_\Omega < -2.5$ cm.
8. The cascade decay must have cowboy topology.
9. One decay track must pass through the SP and ST2 scintillators.
10. All three decay tracks must pass through the first and fourth pixel planes.
11. The x-position of the V^0 vertex is greater than the x-position of the cascade vertex (causality).
12. The event must have a fully reconstructed beam track.
13. The reconstructed primary vertex must lie in the region defined by $|x+91.6| <$ 5 cm, $|y| < 0.4$ cm and $z < 0.2$ cm.
14. The cascade must come from the primary vertex, within 0.3 cm in y and within 0.13 cm in z.
15. The V^0 must *not* come from the primary vertex, with $|B_y| > 0.14$ cm.
16. The third track must *not* come from the primary vertex, with $|B_y| > 0.4$ cm.

17. Cascade taken to be an Ξ hyperon if $M_{\Xi} = M_{\Xi}(PDG) \pm 0.02$ GeV/c^2.

18. $0.2 < |\alpha(\text{cascade})| < 0.6$

19. $q_T(\text{cascade}) > 0.12$ GeV/c

20. $q_T(V^0) > 0.032$ GeV/c

21. Cascade taken to be an Ω hyperon if $M_{\Omega} = M_{\Omega}(PDG) \pm 0.03$ GeV/c^2.

3.6 Summary Of Cuts For 1995 Pb-Pb

3.6.1 Cuts For Λ Hyperon Reconstruction

1. At the V^0 vertex, the distance of closest approach is less than 0.06 cm.

2. The V^0 vertex lies in the region described by $-30 < x_{\Omega} < 0$ cm.

3. The decay must have cowboy topology.

4. The V^0 must come from the interaction vertex, within an ellipse given by $|B_y| \leq 0.15$ cm and $|B_z| \leq 0.10$ cm.

5. $|\alpha| \geq 0.45$

6. $0.035 \leq q_T \leq 0.40$ GeV/c

7. $M_{V^0} \neq M_{\mathrm{K}^0}(PDG) \pm 30$ MeV/c^2

8. $M_{V^0} = M_{\Lambda}(PDG) \pm 10$ MeV/c^2

3.6.2 Cuts For Cascade Reconstruction

1. At the V^0 vertex, the distance of closest approach is less than 0.10 cm.

2. The V^0 decay must have cowboy topology.
3. The V^0 vertex lies in the region described by $-30 < x_\Omega < 0$ cm.
4. $0.02 \leq q_T(V^0) \leq 0.40$ GeV/c
5. $M_{V^0} = M_\Lambda(PDG) \pm 7.5$ MeV/c^2
6. The cascade decay vertex lies in the region described by $-40 < x_\Omega < 0$ cm.
7. At the cascade vertex, the distance of closest approach is less than 0.10 m.
8. The cascade decay must have cowboy topology.
9. The V^0 must *not* come from the interaction vertex, with $B_y \leq -0.1$ cm (for cascades) or $B_y \geq 0.1$ cm (for anti-cascades).
10. The third track must *not* come from the interaction vertex, with $B_y \geq 0.5$ cm (for cascades) or $B_y \leq -0.5$ cm (for anti-cascades).
11. The x-position of the V^0 vertex is greater than the x-position of the cascade vertex (causality).
12. The cascade must come from the interaction vertex (or target), within an ellipse defined by $B_y \leq 0.2$ cm and $B_z \leq 0.1$ cm (or rectangle with $B_y = B_z = 0.4$ cm).
13. Cascade taken as an Ξ hyperon if its $M_\Xi = M_\Xi(PDG) \pm 15$ MeV/c^2, otherwise it is taken as an Ω hyperon if its $M_\Omega = M_\Omega(PDG) \pm 22.5$ MeV/c^2.

3.7 Reconstructed Hyperons In The Pb-Pb And p-Be Data

The results of the reconstruction and selection criteria on the raw data are shown in table 3.1. These numbers are uncorrected for geometrical acceptance, detector efficiency, reconstruction efficiency (all of which are corrected for by calculating the event weight, to be described in the next section) and feed-down.

Table 3.1: Hyperons yields for the full 1995 Pb-Pb and 1996 p-Be data.

Particle Species	Pb-Pb	p-Be
$\Lambda+\overline{\Lambda}$	14403	153669
$\Xi^{-}+\overline{\Xi}^{+}$	2171	554
$\Omega^{-}+\overline{\Omega}^{+}$	250	33

3.8 Event Weighting

The different hyperon species have different geometrical acceptances, detector efficiencies and reconstruction efficiencies, which need to be corrected for in order to allow a comparison of the results for the different hyperon species. To do this, a *weight* is calculated by performing a Monte Carlo simulation.

3.8.1 Monte-Carlo Generation

GEANT [48] was used to generate hyperons with the same p_T, Y and position of the primary vertex as those of the real particle. The decay products of these are then traced through a simulation of the WA97 detectors, with the measured detector efficiencies included. To produce a weight with a reasonably small error 2500 generated particles are required to have their decay products trace through the silicon telescope, meaning that several thousand particles have to be generated for each real particle.

3.8.2 Background Mixing

The track reconstruction efficiencies depend on the track multiplicity in the telescope, so background tracks have to be added to the generated events. These background tracks came from a sample of real data events chosen to be representative of the whole data sample. For the p-Be data, for example, the background sample used for the hyperon weights were real two-track events taken every 200^{th} event. It was found that for the p-Be data that the exact choice of which events to use from the background sample had no significant effect on the resulting weight. For the Pb-Pb however, with its greater range of multiplicities, the background events used were chosen to have a similar track multiplicity to that of the real particle being weighted. In addition, the electronic noise in the detectors' read-out electronics was simulated and included at this stage.

3.8.3 V^0 And Cascade Reconstruction

The next stage was to process the mixed events with ORHION, just as with the real data. They were then processed by the same analysis programs used to select the real data samples. For the p-Be data there was one important change made to the analysis programs concerning the primary vertex reconstruction. In the mixed events the beam track is that of the background event, so it cannot be used to reconstruct the primary vertex. As mentioned above, the primary vertex position is an input to GEANT and is passed from one stage to another until it is read in by the analysis program. Hence, for the Λ hyperons the requirement that the primary vertex is reconstructed successfully changes to checking that the vertex position has been read in successfully from the ORHION output. For the cascades, the requirement that the beam track is reconstructed is simply removed.

3.8.4 Calculating The Weight

The final stage of the chain is the actual calculation of the weight and the associated error. The output of the relevant analysis program is compared with the output of GEANT to determine which of the generated particles were found. In this way hyperons from the background event which may have passed the selection criteria can be rejected. The weight is simply the *total* number generated by GEANT divided by the number found.

3.8.5 Weighted Hyperons In The 1995 Pb-Pb And 1996 p-Be Data

Table 3.2 shows the hyperon yields resulting from the reconstruction, selection and weighting procedures for the 1995 Pb-Pb and 1996 p-Be data. It can be appreciated that due to the number of generated events needed, calculating weights is a time consuming operation. The result of this is that it has been possible to weight only a small sub-sample of the hyperons. The small size of the Ω hyperon sample in both data sets and the Ξ hyperon sample in p-Be has, however, permitted all of these particles to be weighted.

Table 3.2: Hyperon samples which have been weighted for 1995 Pb-Pb and 1996 p-Be data. Also shown are typical values for the weights.

Particle Species	Pb-Pb	p-Be	Average Weights
Λ	2915	5229	~ 800
$\overline{\Lambda}$	807	5035	~ 800
Ξ^-	1194	397	~ 8000
$\overline{\Xi}^+$	303	157	~ 8000
Ω^-+$\overline{\Omega}^+$	250	33	~ 8500

3.9 Feed-Down

The data samples shown above in table 3.2 are not corrected for feed-down from other decay processes. The Λ and $\overline{\Lambda}$ hyperon samples can be contaminated by cascade decays in which only the Λ or $\overline{\Lambda}$ hyperon is reconstructed while Ξ hyperon samples can themselves be contaminated by Ω hyperon decays. In addition to the decay mode used by WA97 for Ω hyperon reconstruction, Ωs can decay into Ξs *via* the following decay mode (and the corresponding charge conjugate mode)

$$\Omega^- \rightarrow \Xi^- + \pi^0$$

The π^0 will not be detected thereby causing contamination of the Ξ^- hyperon (and $\overline{\Xi}^+$ anti-hyperon) samples.

A detailed calculation of the effects of feed-down has yet to be performed, so the data has yet to be corrected for feed-down. An estimation has been made, however, of its effects given the detector geometry of WA97. Feed-down is expected to have an effect of <5% for Λ hyperons and <10% for $\overline{\Lambda}$ anti-hyperons, while the effect for both Ξ^- and $\overline{\Xi}^+$ hyperons should be <2% [41].

3.10 Summary

By reconstructing decay topologies and applying selection criteria, samples of Λ, Ξ and Ω hyperons have been found in both the 1995 Pb-Pb and 1996 p-Be data samples. Subsets of these samples have been weighted to correct for geometrical acceptance, detector efficiency and reconstruction efficiency.

Chapter 4

Enlarging The Kinematic Window for 1995 Pb-Pb

4.1 Introduction

Due to the layout of the silicon telescope, the kinematic acceptance window for WA97 has a curved shape. Particles near the edge of this window will have low acceptance and consequently high weights, which can have a disproportionate effect on the experiment's results. In order to eliminate these events, additional, kinematic cuts are performed, with the result that the weighted data sample does not represent the final data sample. A further complication arising from the shape of the acceptance window is its varying width in rapidity. This means it is non-trivial to extract m_T distributions and inverse slopes. One solution to this is to try to transform the acceptance window into a rectangle, using the symmetry property described in Chapter 1. This gives a rectangular region in which slopes can be found. A significant fraction of the data, however, lies outside this region. To make use of more of the data the acceptance window can be further enlarged by either extrapolating or interpolating the data into the small gaps below and besides the previous reactangular region. As the extrapolation and interpolation only give the number of particles in the gaps, the enlarged kinematic window can only be used in analyses which do not involve distributions. Hence the main use of the enlarged kinematic window is in the determination of particle ratios. This chapter will describe the methods used to enlarge the kinematic window for the sub-sample of the 1995 Pb-Pb data shown in table 4.1. This data sample is smaller than that given at end of the last chapter since the analysis described in this chapter was performed while the weighting process for the 1995 Pb-Pb data was ongoing. In particular, less than half of the Ω hyperon sample had been weighted, giving too low statistics to include them.

Table 4.1: 1995 Pb-Pb data samples used in this analysis.

Particle Species	Total
$\Lambda+\overline{\Lambda}$	750
$\Xi^{-}+\overline{\Xi}^{+}$	902

4.2 Kinematic Cuts

Figure 4.1 shows the $Y - p_T$ distribution for reconstructed events for 1995 Pb-Pb Ξ hyperon data, with the shape evident. This shape is the result of the geometry of the telescope. The scattering angle of a particle's track must lie within certain limits for that particle to pass through the telescope. The relationship between this angle, Θ, Y and p_T can be expressed in the following equation (see Appendix B)

$$p_T = \frac{msinhY sin\Theta}{\sqrt{cos^2\Theta - sin^2\Theta sinh^2 Y}} \tag{4.1}$$

which leads to the curved shape. The upper and lower curves of the acceptance window correspond to the maximum and minimum values of Θ respectively.

Although all the particles within the acceptance window have met all the relevant

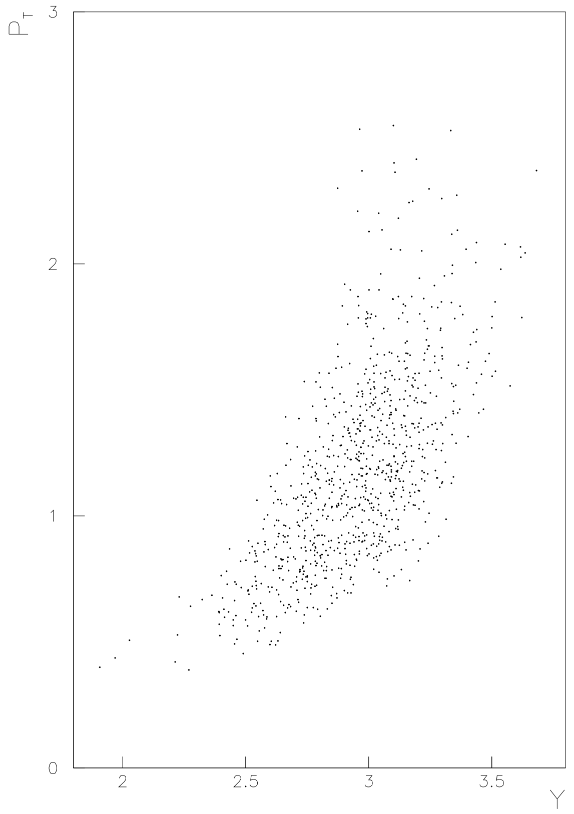

Figure 4.1: The $Y - p_T$ distribution for Ξ hyperons from the 1995 Pb-Pb data.

reconstruction and selection criteria, those at the edges turn out to have significantly higher weights than those in the middle. It is therefore necessary to perform further cuts, in Θ, Y and p_T, which are shown in table 4.2. While the Ω hyperon sample was not used at this stage in the analysis, the kinematic cuts for them are shown for completeness. These cuts further reduce the size of the data samples, down to those shown in table 4.3.

Table 4.2: p_T, Y and Θ cuts for the 1995 Pb-Pb data.

Particle Species	p_T (GeV/c)	Y	Θ (mrad)	
	Min	Min	Min	Max
Λ+$\overline{\Lambda}$	0.4	2.4	47	95
Ξ^-+$\overline{\Xi}^+$	0.6	2.4	48	90
Ω^-+$\overline{\Omega}^+$	0.7	2.45	50	90

Table 4.3: 1995 Pb-Pb data samples used in this analysis after the kinematic cuts.

Particle Species	Total
Λ+$\overline{\Lambda}$	655
Ξ^-+$\overline{\Xi}^+$	813

4.3 Reflecting About Central Rapidity

As outlined in the introduction, the first step in extending the acceptance region is to make use of its symmetry about central rapidity. For the work detailed in this chapter central rapidity was taken to be 2.9 (later work used the correct value of 2.92). This reflection was, therefore, achieved using the transformation

$$Y' = 5.8 - Y \tag{4.2}$$

Figure 4.2 shows, for the Λ, the acceptance window and the reflected window, it also illustrates the common region between the two. In order to avoid double counting the weights of the particles inside the common region are halved.

Reflecting the acceptance window about central rapidity immediately creates a rectangular acceptance region, the *full* region, as depicted in figure 4.3, with limits as shown in table 4.4. However, this region ignores a large amount of the data. It is therefore desirable to have an acceptance region bounded by the minimum p_T cut, the minimum Y cut and its reflected counterpart in order to include a greater per-

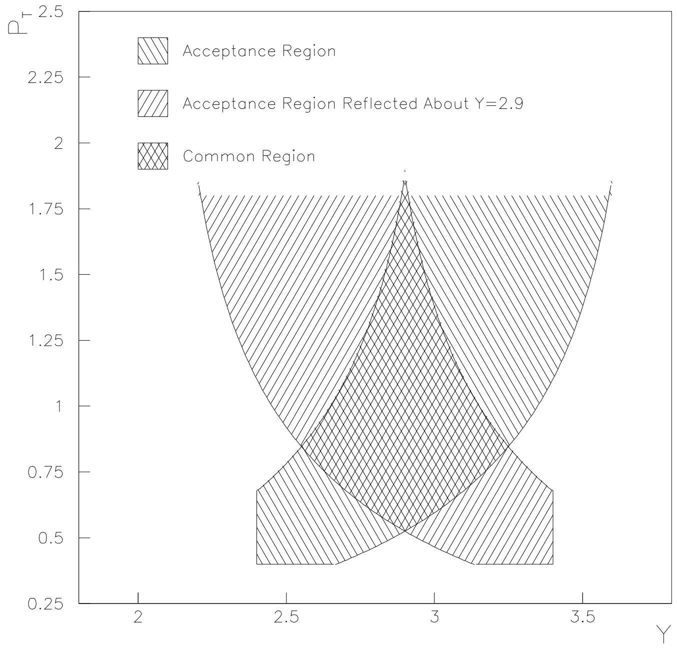

Figure 4.2: The $Y - p_T$ acceptance region for the 1995 Pb-Pb Λ hyperon sample. Also shown is its reflection about central rapidity and the common overlap between them.

Table 4.4: The boundaries of the full regions for the 1995 Pb-Pb data.

Particle Species	Y cuts		p_T
	Min	Max	(GeV/c)
Λ	2.55	3.25	0.525
Ξ	2.59	3.21	0.638

centage of the data. To do this requires filling in two (by symmetry, the two regions at the side are the same) small regions, the one illustrated in figure 4.3 being the subject of the author's work while the one at the bottom will be discussed in the next chapter. There exist two ways of filling this region: *interpolation* and *extrapolation*. When performing the interpolations or extrapolations it is preferable to use the variable m_T instead of p_T, as it is much better represented by an exponential than p_T. m_T is the *transverse mass* and is defined by

$$m_T^2 = m^2 + p_T^2 \tag{4.3}$$

There are two possible parameterisations of the m_T distribution, the one used for this analysis being

$$\frac{dN}{dm_T} = m_T^{3/2} \times f(Y)e^{-m_T/T} \tag{4.4}$$

where $\frac{dN}{dm_T}$ gives the experimental distribution in m_T, $f(Y)$ is the Y distribution and T is the inverse slope (which gives an indication of the temperature of the fireball). By dividing the weights by $m_T^{3/2}$ the data can be fitted by a simple exponential. The second parameterisation, along with the reasons for the existence of two parameterisations, will be described in Chapter 6. The vertical error bars, in all the plots, are calculated as

$$Err_j = \sqrt{\sum_i WGT_i^2} \tag{4.5}$$

where Err_j is the error on the j^{th} bin and WGT_i is the weight of the i^{th} event within bin j.

4.4 Extrapolation

One way to fill the gap shown in figure 4.3 is to extrapolate the data within the full region. To do this involves integrating the m_T distribution of the data inside the full region, first in m_T and then in Y. The data within the full region are assumed to satisfy two conditions, the first of which is that the Y distribution is flat. In fact the Y distribution is assumed to be flat not only in the whole full region (i.e. when integrated in p_T throughout the full region) but also in any p_T strip across the full region. To check the shape of the Y distribution, the full region was split into two parts, by a p_T cut which was chosen such that each region contained approximately the same amount of data (see table 4.5). Figure 4.4 shows, for both the Ξ and Λ

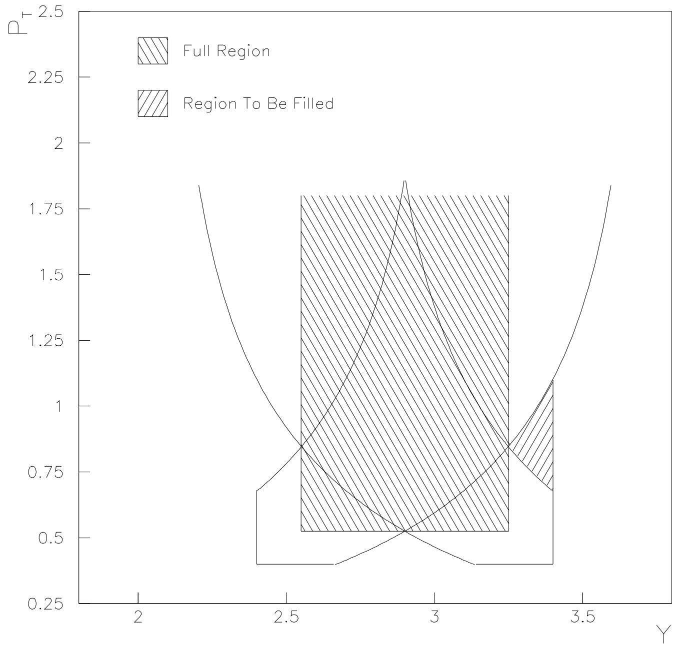

Figure 4.3: The full region for Λ hyperons from the 1995 Pb-Pb data. Also shown is the region which is required to be filled.

Table 4.5: p_T cuts to partition full region.

Particle Species	p_T (GeV/c)
Λ	0.965
Ξ	1.1375

hyperons, that the Y distributions are, within errors, flat in both p_T regions. This means that the Y distribution, $f(Y)$, in equation 4.4 is a constant.

The second assumption is the requirement that the m_T distribution has no Y dependence. To check this requires splitting the full region into two parts, a central part and one made of the two remaining strips (see figure 4.5). The sizes of these regions were again determined so that each part contained the same amount of data, the cuts used to create them being shown in table 4.6.

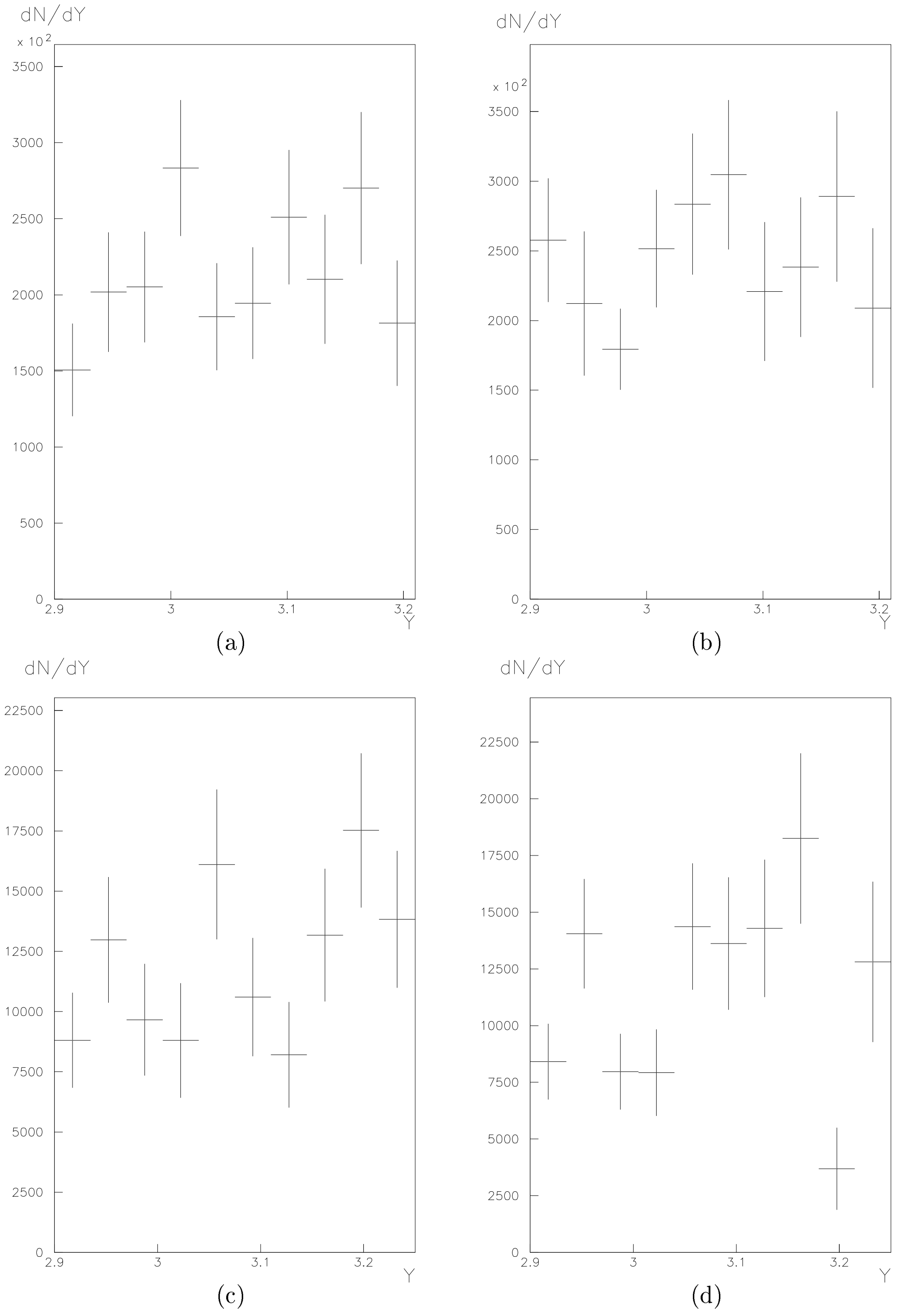

Figure 4.4: The Y distributions for a) Ξ hyperons in the upper p_T region b) Ξ hyperons in the lower p_T region c) Λ hyperons in the upper p_T region d) Λ hyperons in the lower p_T region.

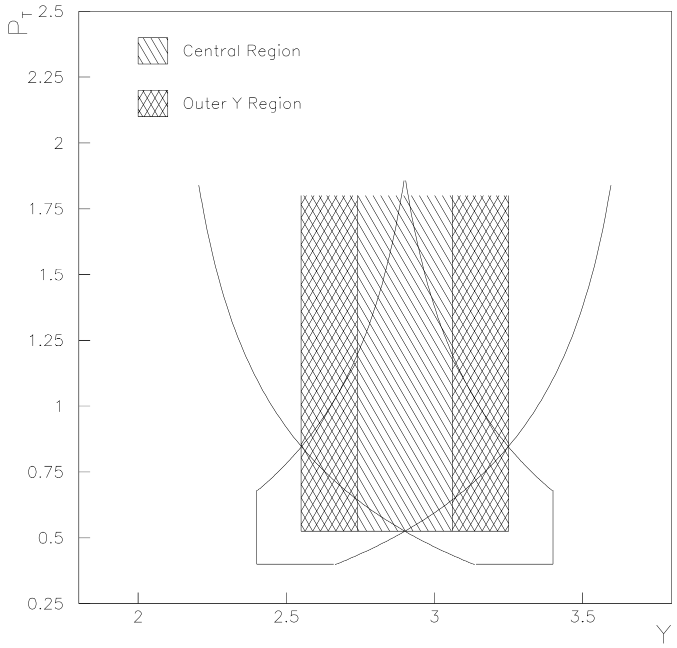

Figure 4.5: The partitioned full region used in the determination of the Y dependence of the m_T distributions, for the 1995 Pb-Pb Λ hyperon sample.

Table 4.6: Y cuts to partition full region.

Particle Species	Y cuts	
	Min	Max
Λ	2.739	3.061
Ξ	2.768	3.032

The resulting m_T distributions, fitted using MINUIT [49] with an exponential of the form

$$e^{P1+P2m_T} \tag{4.6}$$

are shown in figure 4.6 for both Ξs and Λs. The resulting values for $P1$ and $P2$ show that the m_T distributions are Y independent.

Having established that the data are suitable for extrapolation, the m_T distribu-

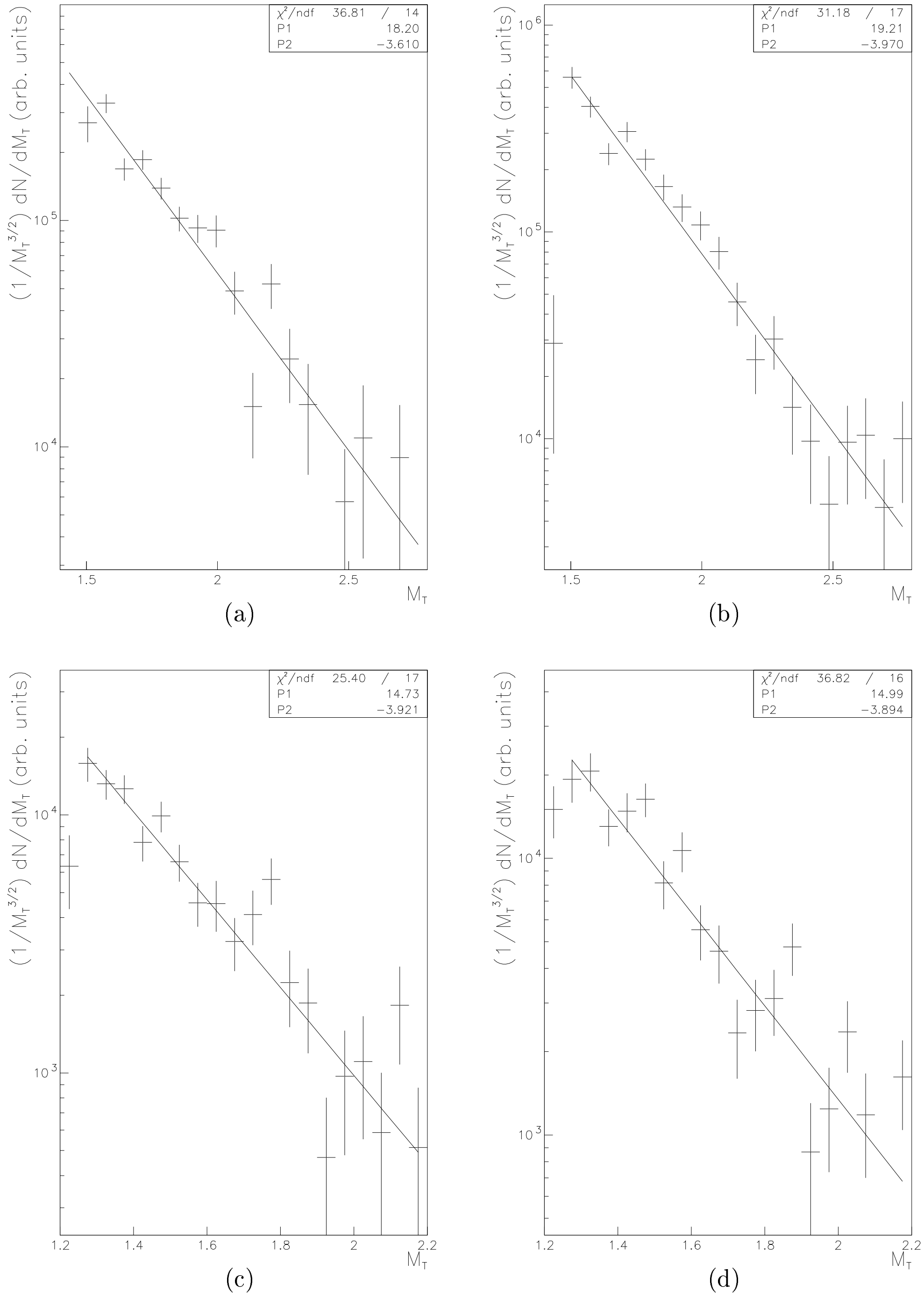

Figure 4.6: The m_T (GeV) distributions for a) Ξ hyperons in the central Y region b) Ξ hyperons in the outer Y region c) Λ hyperons in the central Y region d) Λ hyperons in the outer Y region.

tions for the whole full region are required, these being shown in figures 4.7(a) and (b) for the Ξ and Λ hyperons respectively. The Y distributions are not required since, being flat, they are accounted for in the m_T distributions. These total m_T distributions were fitted in a slightly different way to the previous partial ones, in that the intercept, α, was no longer a fit parameter. It had been found that not only was there a strong correlation between the intercept and the inverse slope but that when integrating the fitted function across the whole full region the result was greater than the sum of the data. Therefore, the fitting routine was altered, with the fit being normalised which removes the need to use the intercept in the fit. The intercept was instead determined from the normalisation by multiplying the input value by the normalisation factor.

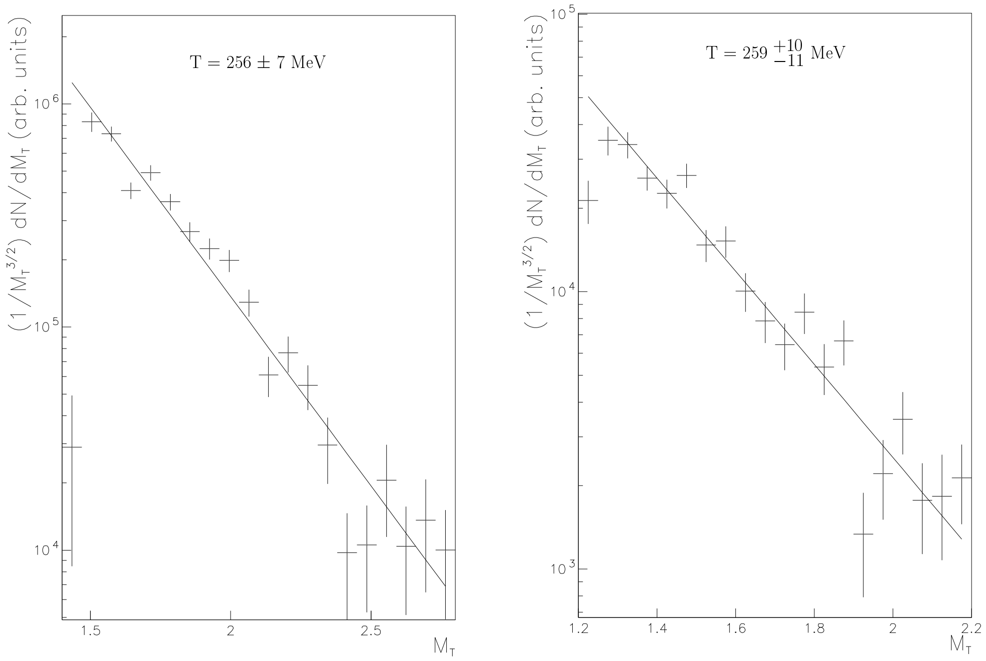

(a) (b)

Figure 4.7: The fitted m_T (GeV) distributions for a) Ξ hyperons in the whole full region b) Λ hyperons in the whole full region.

To do the integrations, these distributions have to be expressed in units of per unit m_T and per unit Y, this being achieved by dividing the value of the intercept from the fits by the bin size and by the width in rapidity of the full region respectively.

In order to integrate the m_T distribution in the gap the integral in m_T is done first, since the limits given by combining equations 4.1 and 4.3 are Y dependent. Integrating again, in Y using the limits given in table 4.7, then gives the required number. However, to be able to compare with the interpolation method (INT, to be described in the next section) requires the number of particles to be calculated within a rectangular region, whose constant upper and lower m_T limits (see table 4.7) are the maximum and minimum m_T of the gap. There are two ways to do this, the first of which is to add the real data inside this rectangle to the result of the integration in the gap (EXT I). Alternatively, the integration can be performed in the whole rectangle (EXT II).

Table 4.7: Y and constant m_T limits used in the integrations.

Particle Species	Y		m_T (GeV)	
	Min	Max	Min	Max
Λ	3.25	3.4	1.30	1.55
Ξ	3.21	3.4	1.54	1.89

4.5 Interpolation

An alternative way to fill the gap is to interpolate (INT) the strip of data which contains the gap, shown in figure 4.9. While this method makes no assumptions as to the shape of the rapidity distribution it uses a much lower percentage of the data, so it is of interest to see which method is the most accurate for the Λ and Ξ hyperon data. For the Ωs, the small percentage of the data used by this method means that it will give larger errors than the extrapolations.

Figures 4.8(a) and (b) show, for respectively Ξs and Λs, the m_T distributions for the whole of the respective strip. Both distributions show a dip caused by the shape of the gap, with the affected bins being removed from the fits. In addition, for the Ξs, the first bin was also removed from the fit. The parameters of the fits, again normalised, were then integrated between the relevant m_T limits (see table 4.7), hence determining the number of particles in the rectangle depicted in figure 4.9.

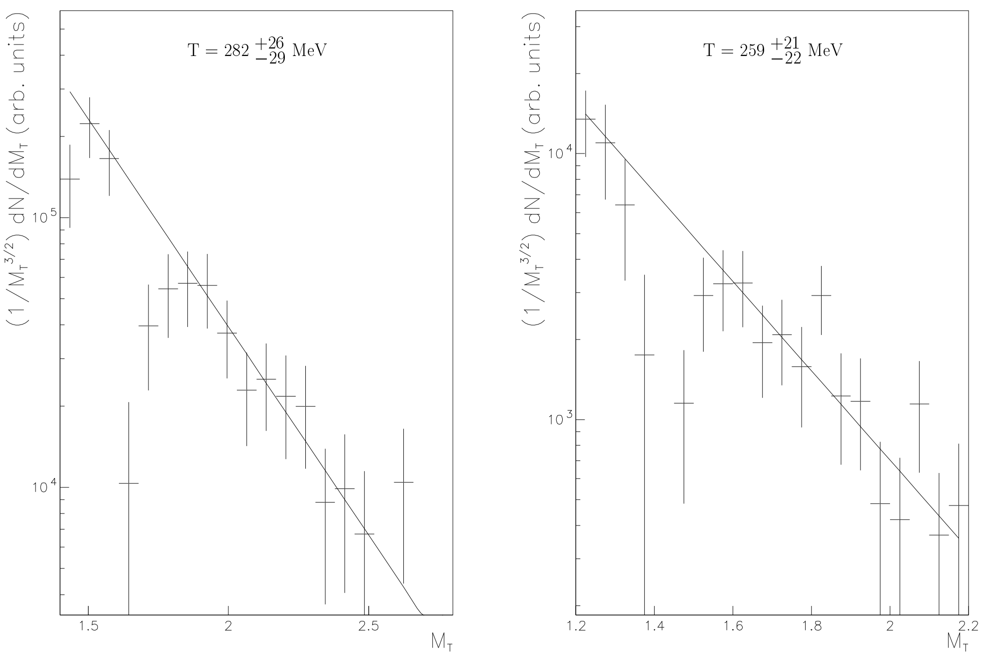

(a) (b)

Figure 4.8: The fitted m_T (GeV) distributions for a) Ξ hyperons in the strip b) Λ hyperons in the strip.

4.6 Errors

The extrapolation and interpolation methods described above do not automatically produce errors on their results. One method is to use the positive and negative errors, δT_+ and δT_- respectively, on the inverse slopes produced by MINOS [49] in

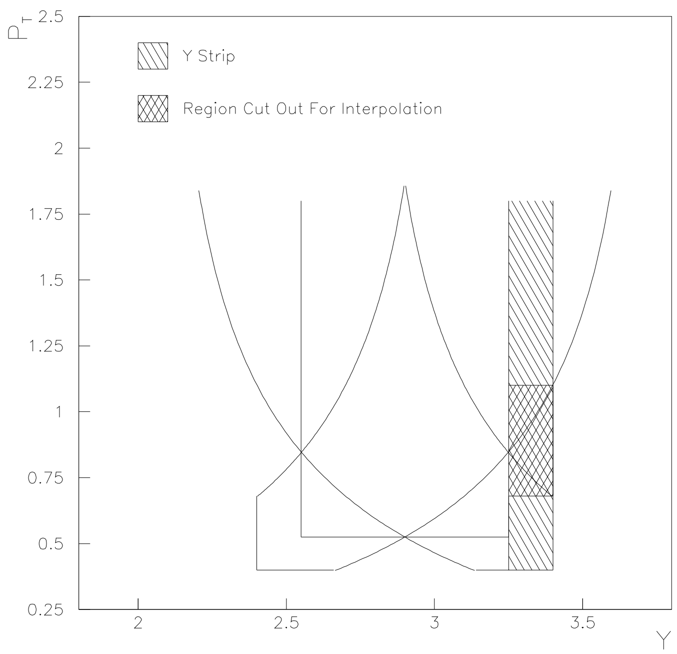

Figure 4.9: The strip used in INT, for Λ hyperons. Also illustrated is the region in which the interpolation and the comparison with the extrapolations are performed.

a calculation very similar to that used to obtain the result. To do this also requires knowing the shifts on the intercept, $\delta\alpha_+$ and $\delta\alpha_-$ respectively. The intercept is determined by the slope if the curve is normalised to the data sample. Thus, for example the shift $\delta\alpha_+$ can be calculated using the expression (with a similar one for $\delta\alpha_-$)

$$\alpha + \delta\alpha_+ = \frac{I}{C' \int e^{-m_T/(T+\delta T_+)} dm_T} \tag{4.7}$$

where I is sum of the data in the bins used in the fit, C' is the reciprocal of the bin size times the rapidity width and the integration is performed solely within the bins used in the fit. This procedure preserves the normalisation of the fit. By integrating, with the appropriate limits, using the slope $T + \delta T_+$ and the intercept $\alpha + \delta\alpha_+$ (or $T - \delta T_-$ and $\alpha - \delta\alpha_-$), the positive (negative) error, $err_\pm$, on the result, A, can be determined from the difference between this value and the result. However, in calculating the $\delta\alpha_\pm$'s the error on I, err_I, is not accounted for. To do so necessitates use of the following expression,

$$E = A\sqrt{\frac{err_{\pm}^2}{A^2} + \frac{err_I^2}{I^2}} \tag{4.8}$$

where E is the true error.

Another method is to scatter each m_T data point within its error according to a Gaussian distribution. This is done 1000 times to generate 1000 data sets. Each of these 1000 data sets is then fitted (using the non-normalised method, which is valid since only the spread of the values is of interest). The resulting 1000 sets of fit parameters are then integrated, using the appropriate limits. The R.M.S of the distribution of the integration results is taken as the error, this procedure being used for both extrapolations and the interpolation.

For EXT I, the total error, E_{tot}, is determined from

$$E_{tot} = \sqrt{E_{Data}^2 + E_{Calc}^2} \tag{4.9}$$

where E_{Calc} is the calculated error in the gap and E_{Data}^2 is the sum of the squares of the errors from the real data within the rectangle defined in table 4.7.

4.7 Systematics

The errors described in the previous section are purely statistical, with no account being taken of systematic effects. While no attempt has so far been made to determine the systematic errors, a check of the accuracy of the methods was performed. This involved taking a strip just inside the full region, having the same width in rapidity as the strip used for the interpolation, and performing the same m_T cuts as for INT (see figure 4.10). The m_T distributions for these strips are shown in figure 4.11 and were used to perform an interpolation to determine the number of particles in the rectangle defined by the limits in table 4.8. This could be compared with the actual data that had been removed from the rectangle and the result of

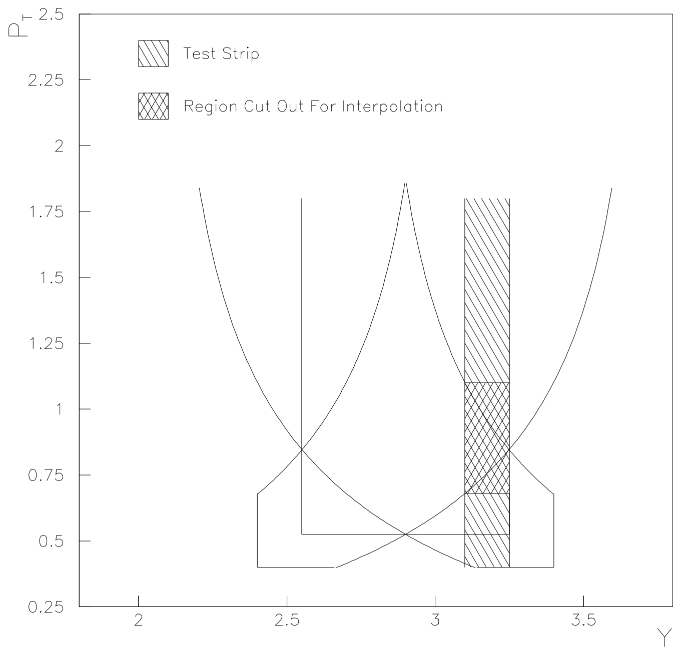

Figure 4.10: The test strip used, for Λ hyperons, to check the accuracy of the methods illustrating the region in which the data was removed.

EXT II calculated previously. The latter could be used since the m_T limits are the same and the rapidity distribution is flat. Likewise the results of EXT I are also the same, however obtaining the corresponding value for the data, necessary to make up the rectangle, is not so easy. Once the data in the test rectangle has been isolated the data is then 'moved' to occupy the same region as the rectangle containing the gap. This is achieved by adding (or subtracting, if the rapidity of the real particle is less than 2.9) the width of the rectangle in rapidity. The Θ cuts can then be applied with the remaining data used in EXT I.

Table 4.8: Y and m_T limits of the test area.

Particle Species	Y		m_T (GeV)	
	Min	Max	Min	Max
Λ	3.1	3.25	1.30	1.55
Ξ	3.02	3.21	1.54	1.89

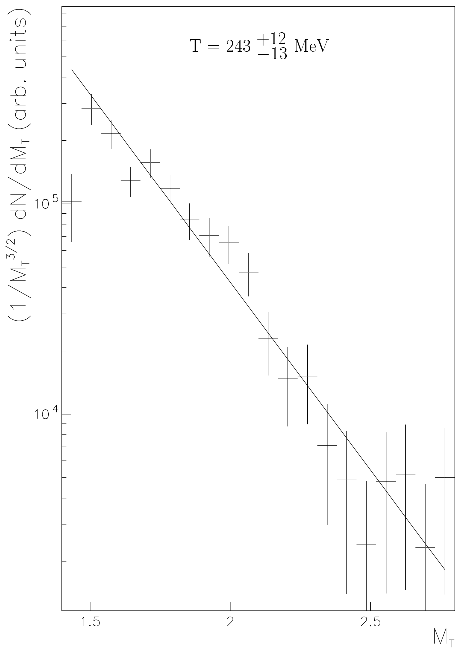

(a) Ξ

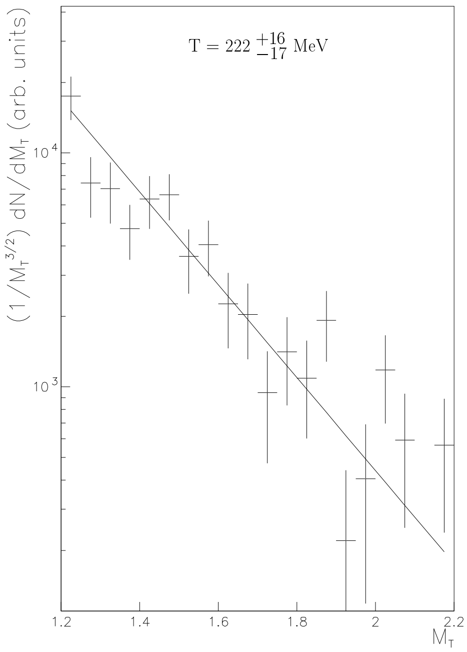

(b) Λ

Figure 4.11: The fitted m_T (GeV) distributions in the test strip.

4.8 Results

The inverse slopes found using the parameterisation shown in equation 4.4, in the full regions and strips for both Λs and Ξs, are shown in table 4.9. The data sample column shows the number of *real* particles used in the calculation of the inverse slope. The results for the full regions and the strips agree for both Ξs and Λs.

The results of the three methods for determining the number of particles within the rectangle shown in figure 4.9 are displayed in table 4.10. There appears to be good agreement, for both particle types, between the two extrapolation methods. However, for the Λs EXT I is also consistent with interpolating. Therefore for determining which is the more accurate method, these results are inconclusive. As for the two error determination methods, it can be seen that both methods give similar errors. Therefore, the choice of which errors method to use can be made on the basis of ease of use. The 1000 fits method is the most automated and so will be used henceforth.

The results for the test areas are shown in table 4.11, with errors on the extrapolations and interpolations being found using the 1000 fits method. Comparison with the data in the test areas leads to the conclusion that EXT II significantly underestimates the data and can therefore be rejected. EXT I, however, is in good agreement with both the data and INT. As EXT I will give better results for lower statistics (*i.e.* the Ω hyperon data), it seems sensible to use this method for all the data samples.

Table 4.9: Inverse slopes (using eqn 4.4).

Particle Species	Region	Data Sample	Inverse Slope (MeV)
Λ	Full	477	259^{+10}_{-11}
	Strip	101	259^{+21}_{-22}
$\Xi^-+\overline{\Xi}^+$	Full	660	256 ± 7
	Strip	86	282^{+26}_{-29}

Table 4.10: The calculated number of particles in the rectangular region.

Particle Species	Method	Result	Errors (Calculated using 1000 fits & integrations)
Λ	EXT I	18400 ± 700	± 1000
	(Data)	$+20100 \pm 6000$	–
	(Total)	$= 38500 \pm 6000$	± 6100
	EXT II	36500 ± 1400	± 1500
	INT	47400 ± 6600	± 6700
$\Xi^- + \overline{\Xi}^+$	EXT I	652000^{+51000}_{-61000}	± 31000
	(Data)	$+710000 \pm 117000$	–
	(Total)	$= 1362000^{+128000}_{-132000}$	± 121000
	EXT II	1156000 ± 38000	± 37000
	INT	$969000^{+147000}_{-141000}$	± 163000

4.9 Summary

Due to the nature of the WA97 detector, the experiment's kinematic acceptance window has a curved shape. In order to ease comparisons between WA97 results and theoretical calculations, a method of converting WA97's acceptance window into a rectangular window is required. Using Pb-Pb interaction data obtained by the WA97 experiment during 1995, the author has studied three possible methods. The first step in all three methods is to use the symmetry of the system, by reflecting the data about central rapidity. Although this by itself generates a rectangular window, there are small regions just beyond this window which, if filled, would enlarge the acceptance window even further. The three methods for filling these regions, two extrapolations and one interpolation, have been evaluated. One of the extrapolation

Table 4.11: The calculated number of particles in the test area.

Particle Species	Method	Result
Λ	Data	47900 ± 5700
	INT	45300 ± 4900
	EXT I (Data) (Total)	18400 ± 1000 $+24500 \pm 4200$ $= 42900 \pm 4300$
	EXT II	36500 ± 1500
$\Xi^{-}+\overline{\Xi}^{+}$	Data	1545000 ± 115000
	INT	1250000 ± 128000
	EXT I (Data) (Total)	652000 ± 31000 $+796000 \pm 77000$ $= 1448000 \pm 83000$
	EXT II	1156000 ± 37000

methods has been discarded because it underestimates the number of particles. The interpolation method, while agreeing with the remaining extrapolation method for Λs and Ξs, would give greater statistical errors for Ωs, so it is also discarded in the interests of consistency.

Chapter 5

Hyperon Ratios and Inverse Slopes for 1995 Pb-Pb

5.1 Introduction

Once the choice had been made as to which method would be used to enlarge the acceptance window, this method was used to produce physics results. These results could then be compared with those obtained using the log likelihood method which was the method used by WA97 for its published results. The comparison of these two methods in terms of particle ratios was performed in two regions, the region of overlap between the acceptance windows of the three particle species and extrapolated to all p_T (as in the published WA97 results). This made it possible to check the consistency of the results in these two regions. The m_T distributions were again fitted using the parameterisation given in equation 4.4 (page 65). For this stage of the analysis the total weighted hyperon 1995 Pb-Pb samples shown in table 3.2 (page 58) were used.

5.2 Kinematic Regions

While the kinematic cuts for the three particle species were unchanged from those given in table 4.2 (on page 63), the more accurate value of 2.92 was used for central rapidity in this analysis. The reflection transformation shown in equation 4.2, therefore, becomes

$$Y' = 5.84 - Y \tag{5.1}$$

This obviously changes the size of the full regions and the gaps compared with those used in the work outlined in the last chapter. The new values for the full regions are shown in table 5.1, below. The m_T distributions obtained in these regions were used by the reflection method in both comparison regions. For the log likelihood method these Y and p_T cuts were used with the Θ cuts of the acceptance window (see table 4.2) to define a *data* region.

By studying table 4.2 it can be seen that the $p_T > 0.7$ GeV/c region between the particle species is determined by the minimum p_T and minimum Y of the Ω acceptance window. The other region used for comparison of the two methods is the standard WA97 window, within which all published ratios and yields are calculated. This region is one unit of rapidity wide centred on central rapidity and covers all p_T. Both these regions are detailed in table 5.2. Table 5.3 summarises the total data used for this analysis, the data within the relevant acceptance window and the data in the full/data region appropriate for that particle species.

5.3 Reflection Method

When using the reflection about central rapidity method (REF), the m_T distributions were determined in the full regions for both comparison regions. The way in which double counting, due to the $p_T > 0.7$ GeV/c region between the acceptance window and its reflection, was avoided was simplified compared with before. Pre-

Table 5.1: The boundaries of the full regions for the 1995 Pb-Pb data.

Particle Species	Y cuts		p_T
	Min	Max	(GeV/c)
Λ	2.57	3.27	0.539
Ξ	2.605	3.235	0.655
Ω	2.625	3.215	0.8726

Table 5.2: The p_T and Y regions used for the comparison.

Region	p_T (GeV/c)	Y	
	Min	Min	Max
Overlap	0.7	2.45	3.39
All p_T	0.0	2.42	3.42

viously this had been achieved by counting both real weights and their reflected counterparts with the weights in the overlap region being halved. The simplification was to leave the weights in the overlap region unmodified but to double the weights outside the overlap region and to only count real weights. The errors on the bins of the distributions were calculated using the unmodified weights, as reflection does not increase the statistics, with equation 4.5 (page 65).

5.3.1 $p_T > 0.7$ GeV/c Region

To calculate the number of a particle species in the $p_T > 0.7$ GeV/c region required calculating the sum of the weights within the region and then adding the extrapolation of the m_T distributions from the full region into the gaps. When calculating the sum of the weights, as with the m_T distributions, care had to be taken to avoid double counting, with the same solution as described above being used.

Table 5.3: 1995 Pb-Pb data samples used in this analysis.

Particle Species	Total	Acceptance Window	Full/Data Region
Λ	2915	2395	1826
$\overline{\Lambda}$	807	670	521
Ξ^-	1194	1043	844
$\overline{\Xi}^+$	303	282	233
$\Omega^-+\overline{\Omega}^+$	250	228	174

For the Λ and Ξ hyperon data the only gaps to be filled were the ones at the sides of the overlap region. Figure 5.1 illustrates the relationship between the $p_T > 0.7$ GeV/c region and the acceptance windows, both real and reflected, for Λs. By symmetry the two gaps shown in figure 5.1 are the same, therefore the extrapolation was performed in only one of them with the resulting value being doubled and then added to the sum of the weights. In all cases the gap chosen was the one at the high rapidity side of the overlap region.

With the size of the $p_T > 0.7$ GeV/c region being determined by the Ω hyperon acceptance window, not only the gaps at the sides but also the gap at low p_T had to be filled for the Ω hyperon data. As this lower gap is centred on central rapidity the extrapolation only needed to be performed in one half of it. As shown in figure 5.2, the half below central rapidity was chosen. The number of Ωs in the overlap region was, therefore, the sum of the weights in this region plus twice the sum of the two extrapolations. The upper and lower limits for the extrapolation regions are detailed in table 5.4.

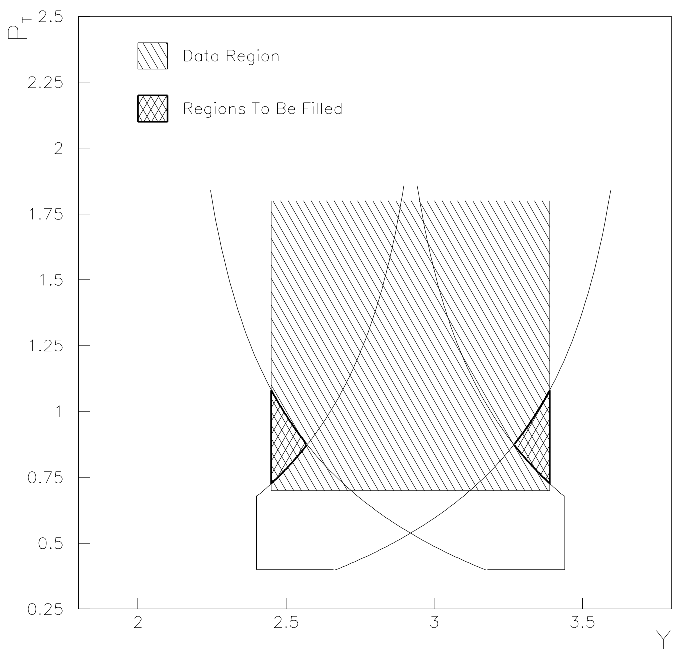

Figure 5.1: The $p_T > 0.7$ GeV/c region imposed on the Λ hyperon acceptance region. The single hatched area depicts the region from which the data is taken while the cross hatched areas are the gaps filled by extrapolation.

5.3.2 All p_T

A slightly different approach had to be taken with the "All p_T" region, as the minimum rapidity of this region was less than the minimum rapidity of the Ω hyperon acceptance window. The full region was used in order to determine the data in the "All p_T" region. This was done by summing the weights inside the full region, adjusting them as before to prevent double counting, and dividing the result by its width in rapidity. This gave the number per unit of rapidity around central rapidity, effectively the number in the "All p_T" region above the minimum p_T of the full region. The m_T distribution in the full region was then extrapolated down to $p_T = 0$ from the base of the full region within one unit of rapidity about central rapidity. The sum of these two results gave the number of particles in the "All p_T" region.

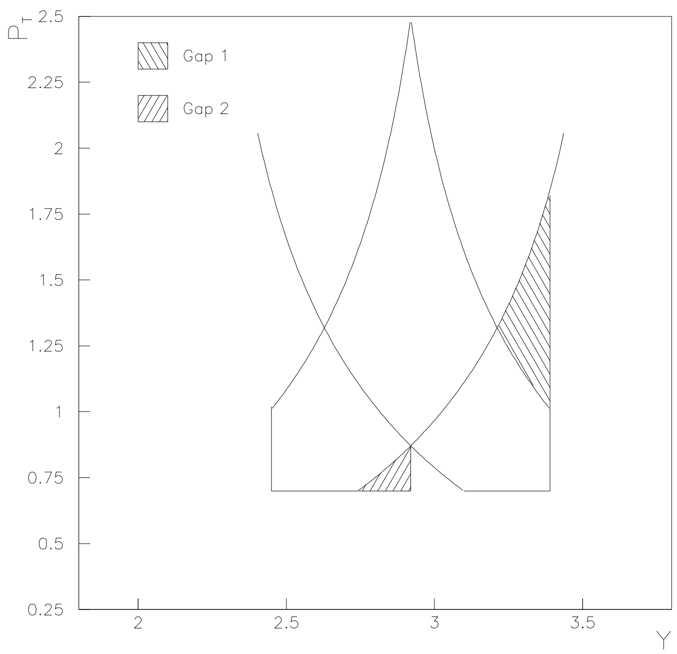

Figure 5.2: The real and reflected acceptance windows for Ωs. The shaded areas are the two gaps into which the m_T distribution was extrapolated.

5.3.3 Errors

The error on the sum of weights was calculated for the $p_T > 0.7$ GeV/c region using

$$Error = \sqrt{\sum_i WGT_i^2} \tag{5.2}$$

where WGT_i is the unmodified weight of the i^{th} event within the $p_T > 0.7$ GeV/c region. For the "All p_T" region, this same procedure was followed with the addition of dividing the expression in equation 5.2 by the width in rapidity of the full region. The errors on the extrapolations were calculated by using a Gaussian distribution to scatter the m_T distributions according to their errors 1000 times. These 1000 m_T distributions were then each extrapolated into the appropriate area with the standard deviation of the resulting distribution being taken as the error for that area. For the $p_T > 0.7$ GeV/c region, these errors were then doubled and linearly

Table 5.4: The p_T and Y limits for the extrapolations.

Particle Species	p_T (GeV/c)		Y	
	Min	Max	Min	Max
Λ	0.73	1.08	3.27	3.39
Ξ	0.8	1.34	3.235	3.39
Ω Gap 1	1.01	1.85	3.215	3.39
Ω Gap 2	0.7	0.87	2.74	2.92

added to the error on the sum of the weights to get the error on the number of particles. The extrapolation error was simply added linearly to the error on the sum of the weights for the "All p_T" region.

5.4 Log Likelihood Method

The standard means by which m_T distributions are fitted to the data is the Log Likelihood Method (LOG). This is based on the Principle of Maximum Likelihood, which is outlined in Appendix C. In fact this method minimises the negative of the log likelihood, using MINUIT [49]. The expression which is minimised is the following sum over all the particles

$$-ln(\mathcal{L}) = -\sum_i WGT_i \times ln(P_i(Y, m_T)) \tag{5.3}$$

where $ln(\mathcal{L})$ is the log likelihood, WGT_i is the weight of the i^{th} particle and $P_i(Y, m_T)$ is the probablity of particle i having rapidity Y and transverse mass m_T. In general, this probability is given as the product of the probabilities $P_i(Y)$ and $P_i(m_T)$ divided by the integral of the Y and m_T distributions, with the current fit parameters, in the data region. For a flat Y distribution and a m_T distribution given by equation 4.4 (page 65)

$$P_i(Y) = 1 \tag{5.4}$$

and

$$P_i(m_T) = m_T^{3/2} \times e^{-m_T/T} \tag{5.5}$$

Once the best fit has been obtained, the Y and m_T distributions can be integrated to give the number of particles in the desired region. This is done by dividing the integration of the distributions in the desired region ($p_T > 0.7$ GeV/c or "All p_T") by the result of integrating the same distributions in the data region. This gives the *scale factor*, S, by which the number of particles in the comparison region is greater than than the number of particles in the data region. The number of particles in the comparison region is, therefore, the sum of the weights of the particles used in the fit multiplied by the scale factor. The error on this value is given by

$$Err = \sqrt{(S \times Er_{WGT})^2 + (Er_S \times WGT)^2} \tag{5.6}$$

where Er_{WGT} is the error on the sum of the weights (calculated as in equation 5.2), Er_S is the error on the scale factor and WGT is the sum of the weights. Er_S is calculated from the derivative of S with respect to the inverse slope (which is the only fit parameter).

5.5 Calculating Ratios

Both of the methods described calculate the number of particles in a given acceptance window based upon the weighted events used. Further corrections are necessary before particle ratios can be calculated. As only one decay mode is studied for each hyperon, allowance has to be made for the unseen decay modes. This is achieved by dividing the output of REF or LOG by the branching ratio for that decay mode, which are shown in table 5.5. For Λs the branching ratio is the PDG value [45], while for the cascades they are the PDG branching ratio for decaying into a Λ hyperon and a meson multiplied by the Λ hyperon value.

Table 5.5: Branching ratios used to correct for unseen decay modes.

Particle Species	Branching Ratio
$\Lambda + \overline{\Lambda}$	0.639
$\Xi^- + \overline{\Xi}^+$	0.99887 $\times$ 0.639
$\Omega^- + \overline{\Omega}^+$	0.678 $\times$ 0.639

Due to the nature of the weighting procedure (described in Chapter 3) only a fraction of the Λs and Ξs could be used. This was taken into account by multiplying the number of particles by the ratio of reconstructed particles to weighted particles, for which the relevant numbers are shown in table 5.6. The size of the Λ hyperon sample used is less than that given in table 3.1 since all the weighted Λs were taken from a sub-set of the data. This could have been corrected for by dividing the number of particles by the number of triggers from which that data had been obtained, which are shown in table 5.7. As this correction only affected ratios between cascades and Λs, in which the cascade value was always divided by the Λ hyperon value, a correction was only applied to the Λ hyperon values. This required multiplying the number of Λs by the ratio of the triggers used for the cascade samples to the triggers used for the Λ hyperon sample.

Table 5.6: Data samples used, for Λs and Ξs.

Particle Species	Total	Weighted
Λ	6796	2915
$\overline{\Lambda}$	886	807
$\Lambda + \overline{\Lambda}$	7682	3722
Ξ^-	1738	1194
$\overline{\Xi}^+$	433	303
$\Xi^- + \overline{\Xi}^+$	2171	1497

Table 5.7: Number of triggers from which data was obtained.

Particle Species	Triggers
$\Lambda + \overline{\Lambda}$	2.01×10^6
$\Xi + \Omega$	110.29×10^6

These corrections were also applied to the errors on the number of particles given by the two methods. The errors on the ratios were calculated using the following expression

$$\frac{a \pm \delta a}{b \pm \delta b} = \frac{a}{b} \pm \frac{a}{b}\sqrt{\frac{\delta a^2}{a^2} + \frac{\delta b^2}{b^2}} \tag{5.7}$$

5.6 Results

The m_T distributions for all the hyperon species are shown in figures 5.3 to 5.7. The m_T distributions found using REF are shown in the (a) plots while the (b) plots show those obtained using LOG. In all the plots the lines are fits to the distributions, which for REF give the values for the inverse slopes written on the plots and given in table 5.8. For LOG the values are the results from the event-by-event log likelihood fit and *not* from the fit to the binned data in the plots.

The results of the two methods for the inverse slopes of the hyperons are given in table 5.8 and displayed in figure 5.8. There is agreement within the errors between the two methods for all particle species.

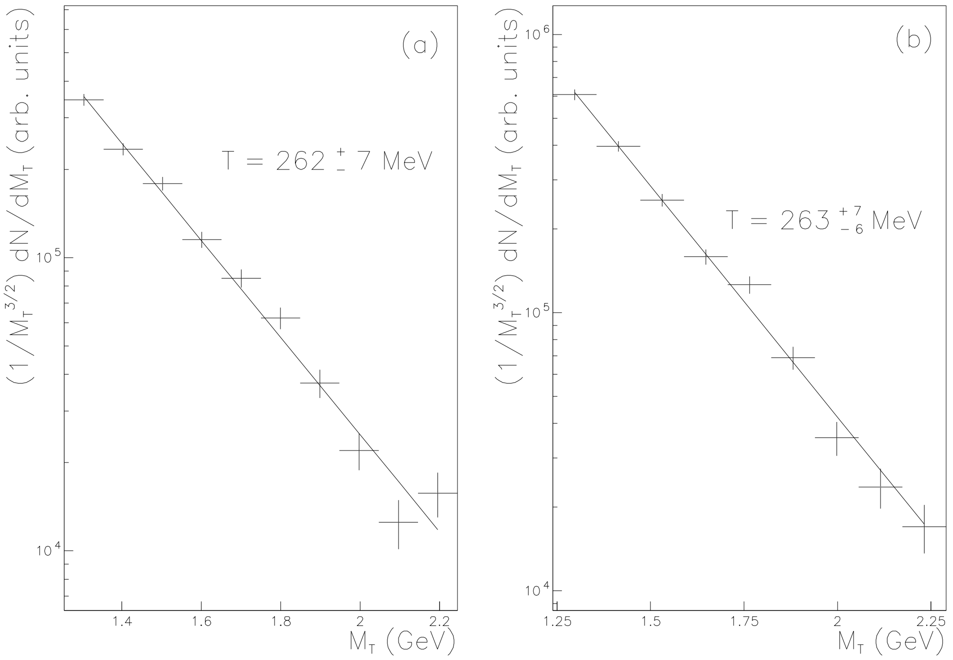

(a) (b)

Figure 5.3: The m_T distributions for a) Λs + $\overline{\Lambda}$s using REF b) Λs + $\overline{\Lambda}$s using LOG.

Table 5.8: Inverse slopes (MeV) (using eqn 4.4).

Particle Species	REF	LOG
Λ	258 ± 8	260 ± 7
$\overline{\Lambda}$	265^{+15}_{-14}	277^{+16}_{-14}
$\Lambda + \overline{\Lambda}$	262 ± 7	263^{+7}_{-6}
Ξ^-	313^{+17}_{-16}	316^{+17}_{-15}
$\overline{\Xi}^+$	284^{+27}_{-24}	322^{+34}_{-29}
$\Xi^- + \overline{\Xi}^+$	312^{+15}_{-14}	317^{+15}_{-14}
Ω^-	302^{+44}_{-38}	326^{+61}_{-45}
$\overline{\Omega}^+$	216^{+42}_{-37}	235^{+60}_{-41}
$\Omega^- + \overline{\Omega}^+$	279^{+31}_{-28}	297^{+43}_{-34}

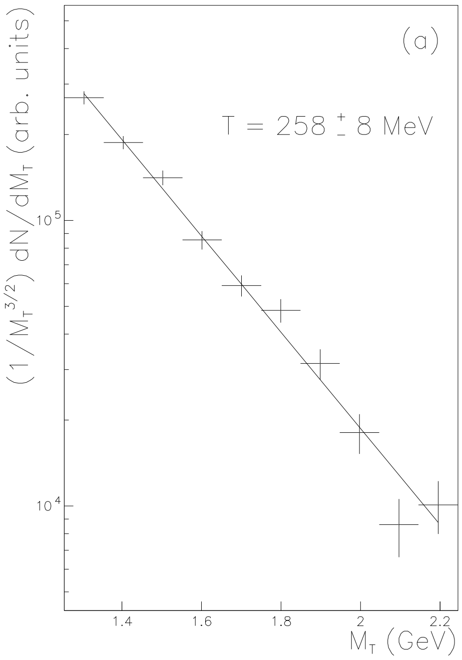

(a)

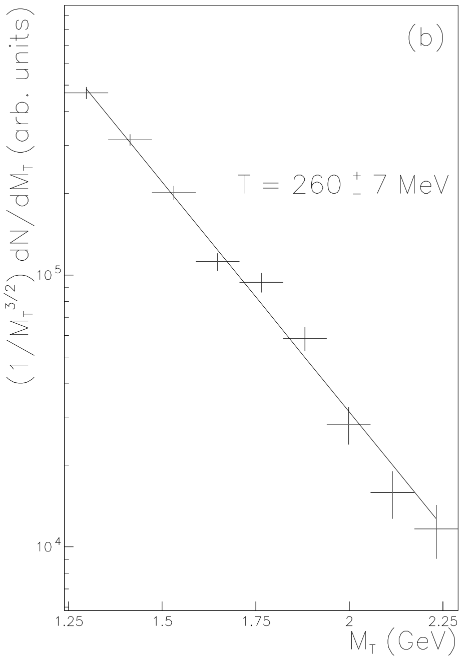

(b)

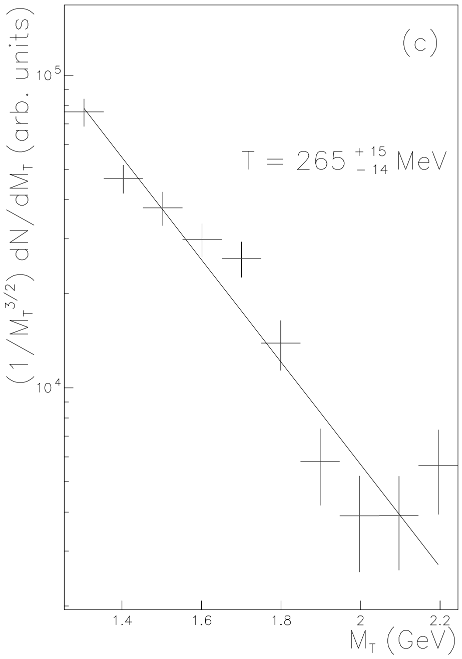

(c)

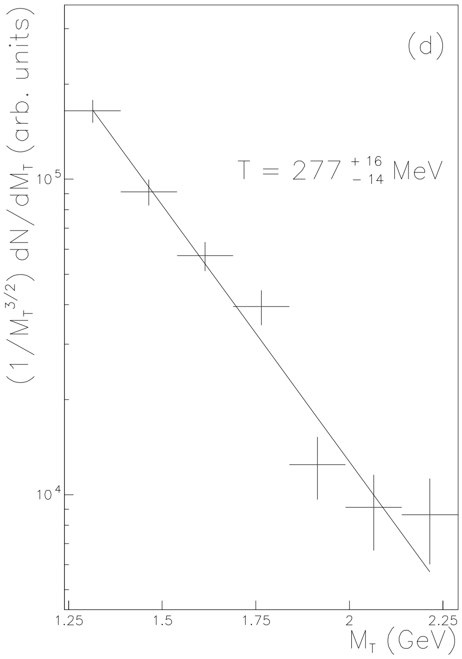

(d)

Figure 5.4: The m_T distributions for a) Λs using REF b) Λs using LOG c) $\overline{\Lambda}$s using REF d) $\overline{\Lambda}$s using LOG.

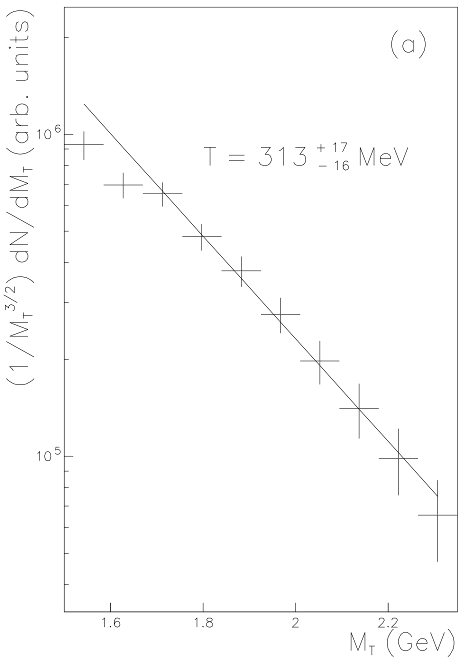

(a)

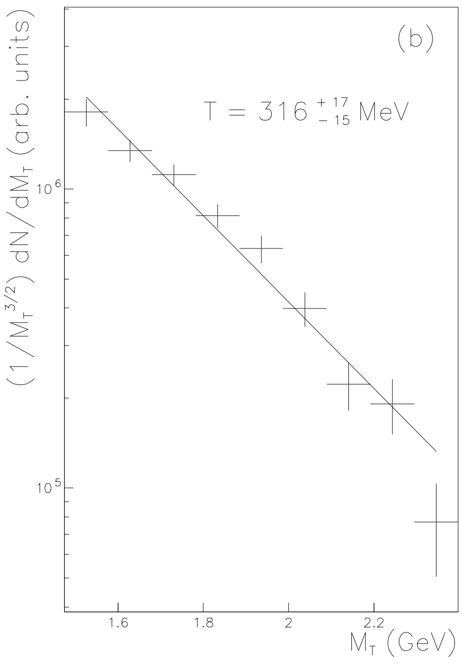

(b)

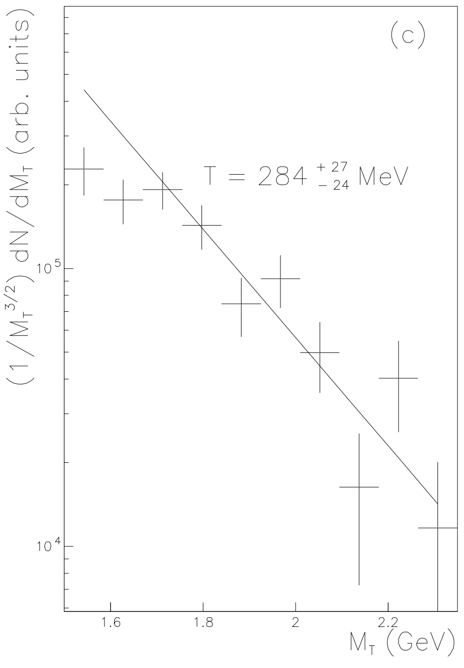

(c)

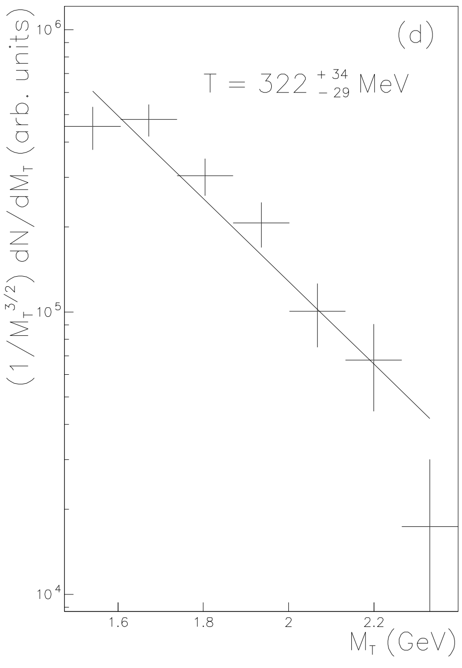

(d)

Figure 5.5: The m_T distributions for a) Ξ^-s using REF b) Ξ^-s using LOG c) $\overline{\Xi}^+$s using REF d) $\overline{\Xi}^+$s using LOG.

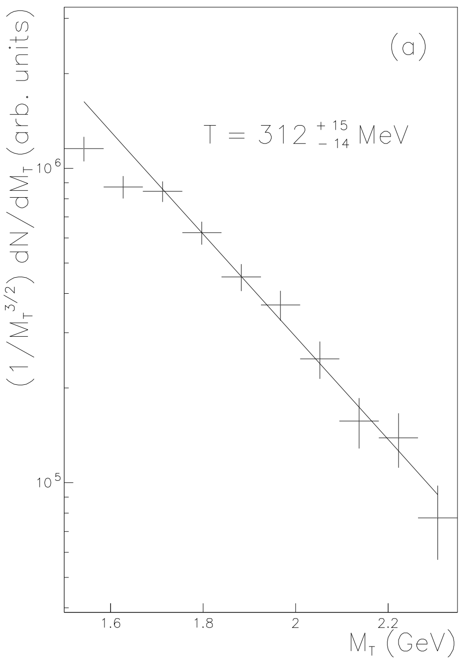

(a)

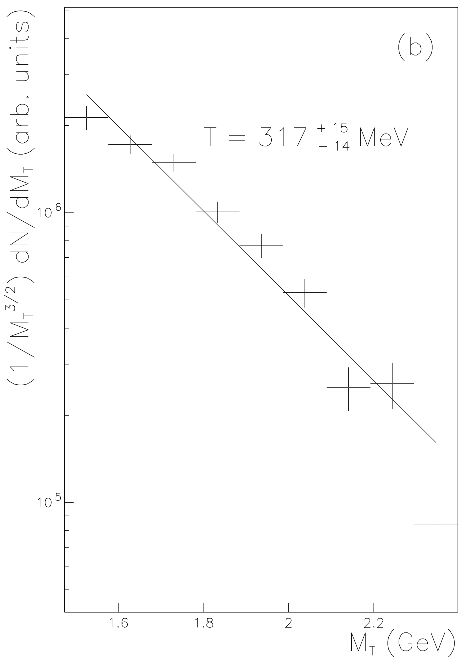

(b)

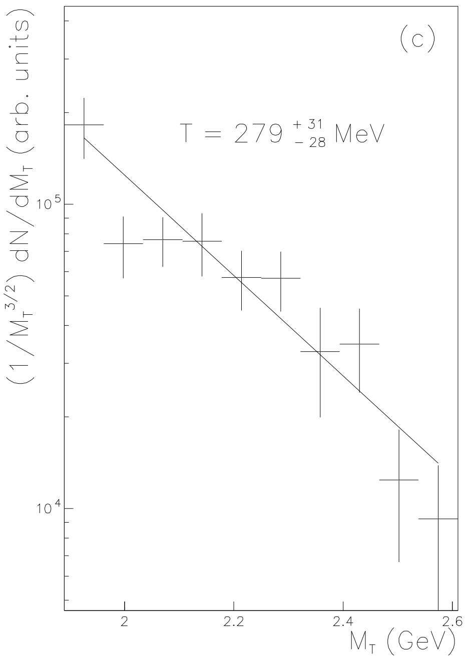

(c)

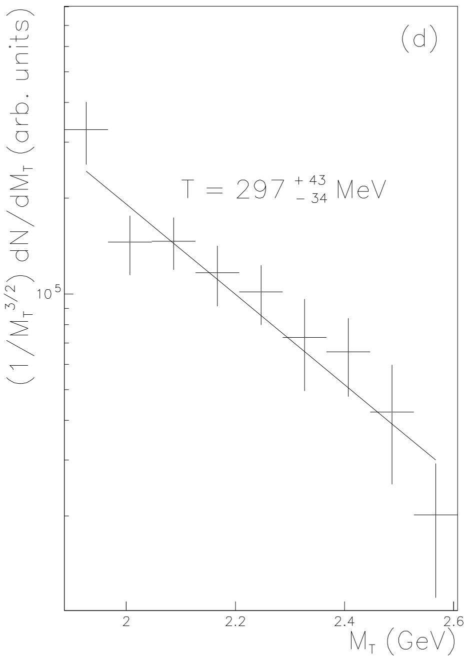

(d)

Figure 5.6: The m_T distributions for a) Ξ^-s + $\overline{\Xi}^+$s using REF b) Ξ^-s + $\overline{\Xi}^+$s using LOG c) Ω^-s + $\overline{\Omega}^+$s using REF d) Ω^-s + $\overline{\Omega}^+$s using LOG.

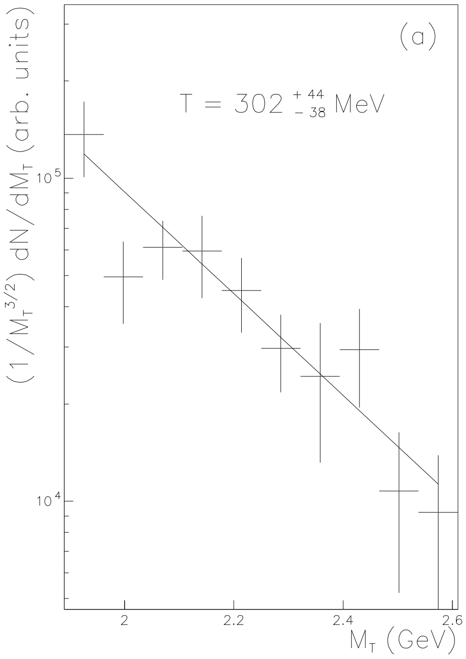

(a)

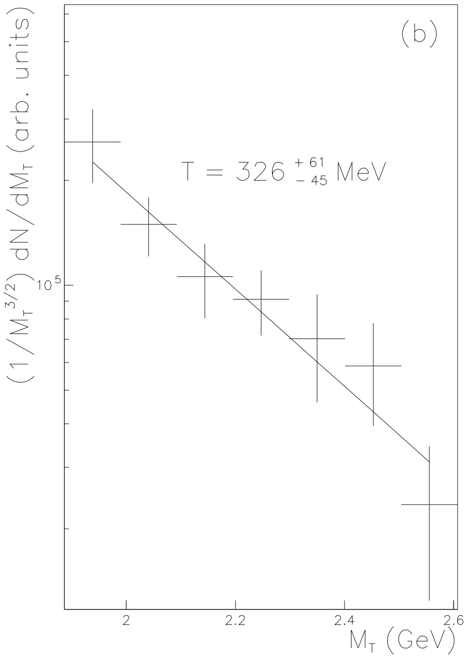

(b)

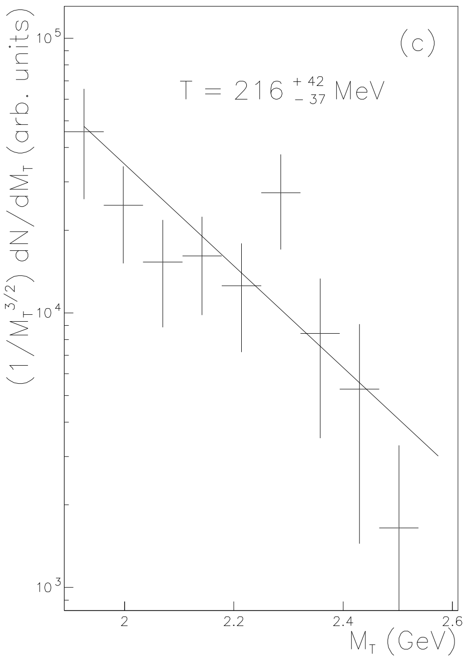

(c)

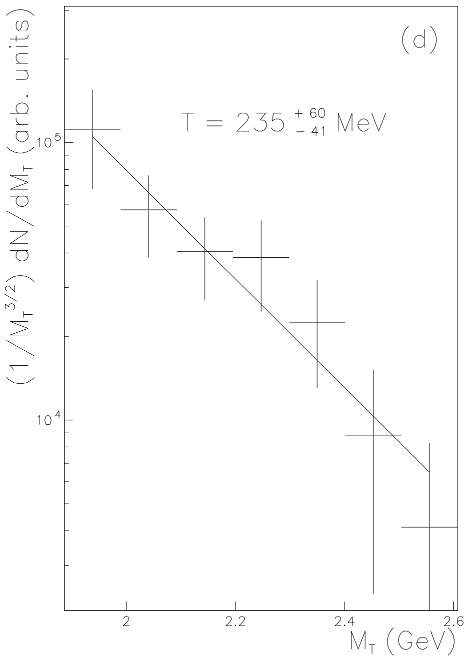

(d)

Figure 5.7: The m_T distributions for a) Ω^-s using REF b) Ω^-s using LOG c) $\overline{\Omega}^+$s using REF d) $\overline{\Omega}^+$s using LOG.

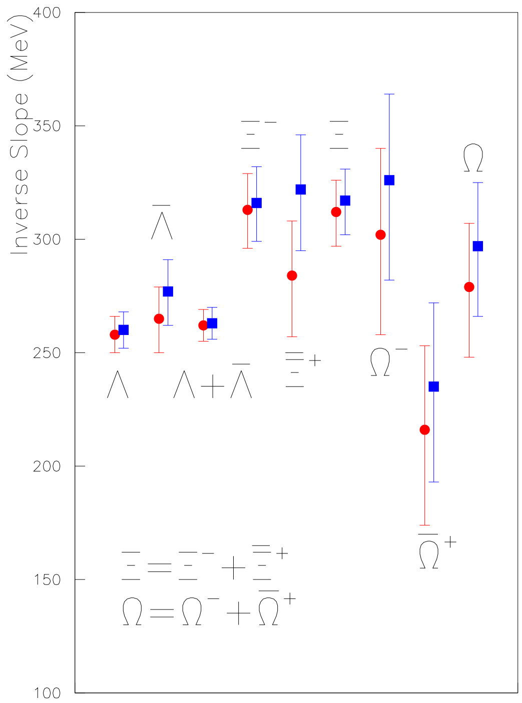

Figure 5.8: The inverse slopes for each particle species. The circles are the slopes determined using REF and the squares are the slopes using LOG.

Tables 5.9 and 5.10 show the particle ratios calculated by the two methods in the $p_T > 0.7$ GeV/c and the "All p_T" regions, respectively. For both regions there is, again, agreement between the methods within errors. Ratios such as these can be used to determine parameters of the central fireball by fitting them with a thermal model. This has been done [50] using the results of several experiments, the parameters extracted being consistent with the expected properties of a deconfined QGP.

Despite the good agreement between the methods, LOG has several advantages over REF which make it more suitable for future use. In addition to being the standard method in use by the WA97 Collaboration, LOG has two, more technical, advantages over REF. LOG is capable of using all the data within the acceptance window whereas REF discards some as well as losing the event-by-event information contained in the weights which LOG includes.

Table 5.9: Particle Ratios, $p_T > 0.7$ GeV/c.

Particle Ratio	REF	LOG
$\frac{\overline{\Lambda}}{\Lambda}$	0.141 ± 0.008	0.140 ± 0.008
$\frac{\overline{\Xi}^+}{\Xi^-}$	0.261 ± 0.021	0.253 ± 0.021
$\frac{\overline{\Omega}^+}{\Omega^-}$	0.365 ± 0.068	0.404 ± 0.083
$\frac{\Xi^-}{\Lambda}$	0.083 ± 0.004	0.087 ± 0.004
$\frac{\overline{\Xi}^+}{\overline{\Lambda}}$	0.152 ± 0.013	0.157 ± 0.014
$\frac{\Omega^-}{\Xi^-}$	0.226 ± 0.024	0.200 ± 0.022
$\frac{\overline{\Omega}^+}{\overline{\Xi}^+}$	0.316 ± 0.055	0.317 ± 0.062
$\frac{\Xi^- + \overline{\Xi}^+}{\Lambda + \overline{\Lambda}}$	0.090 ± 0.004	0.095 ± 0.004
$\frac{\Omega^- + \overline{\Omega}^+}{\Xi^- + \overline{\Xi}^+}$	0.244 ± 0.022	0.223 ± 0.021

Table 5.10: Particle Ratios, All p_T.

Particle Ratio	REF	LOG
$\frac{\overline{\Lambda}}{\Lambda}$	0.138 ± 0.009	0.135 ± 0.008
$\frac{\overline{\Xi}^+}{\Xi^-}$	0.256 ± 0.027	0.251 ± 0.022
$\frac{\overline{\Omega}^+}{\Omega^-}$	0.414 ± 0.121	0.464 ± 0.127
$\frac{\Xi^-}{\Lambda}$	0.074 ± 0.004	0.075 ± 0.004
$\frac{\overline{\Xi}^+}{\overline{\Lambda}}$	0.138 ± 0.015	0.139 ± 0.013
$\frac{\Omega^-}{\Xi^-}$	0.187 ± 0.026	0.187 ± 0.026
$\frac{\overline{\Omega}^+}{\overline{\Xi}^+}$	0.302 ± 0.084	0.347 ± 0.088
$\frac{\Xi^- + \overline{\Xi}^+}{\Lambda + \overline{\Lambda}}$	0.081 ± 0.004	0.082 ± 0.004
$\frac{\Omega^- + \overline{\Omega}^+}{\Xi^- + \overline{\Xi}^+}$	0.208 ± 0.025	0.217 ± 0.026

5.7 Summary

The method of reflecting the data about central rapidity has been compared with the log likelihood method, the standard method used in analysis of WA97 data. Good agreement between the two methods has been found in obtaining inverse slopes and particle ratios when analysing exactly the *same* data. The log likelihood method, however, is able to use all the data within the acceptance window and use event-by-event information given by the individual particle weights. For these reasons the reflection method will not be pursued further.

Chapter 6

Analysis of Hyperons in the 1996 p-Be Data

6.1 Introduction

The analysis of the weighted data samples for the 1996 p-Be data began, as with the Pb-Pb data, by determining the acceptance windows. The distributions within these windows were fitted using the log likelihood method. For this analysis, only the "All p_T" region, described in the previous chapter, was considered. Rather than calculate particle ratios, the particle yields per event were calculated and plotted with the p-Pb and Pb-Pb values versus the number of nucleons which participated in the collision.

6.2 Kinematic Limits

As with the Pb-Pb data, kinematic cuts had to be performed in order to remove events with very high weights. These were determined by applying Y, p_T and Θ

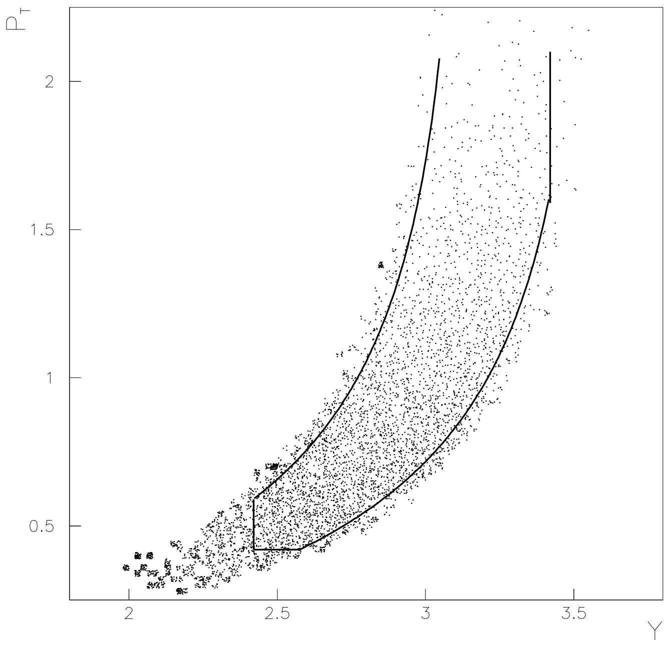

Figure 6.1: The $Y - p_T$ distribution for weighted Λ and $\overline{\Lambda}$ hyperons from the 1996 p-Be data with the boundaries of the acceptance window superimposed.

cuts and comparing the lowest and highest weight within those cuts. The cuts were varied, changing only one cut at a time, to try to maximise the number of particles accepted whilst keeping the maximum accepted weight about ten times the minimum weight. This procedure resulted in the cuts shown in table 6.1. Figure 6.1 shows the $Y - p_T$ distribution for all the weighted Λ and $\overline{\Lambda}$ hyperons plotted with the acceptance window.

Table 6.1: p_T, Y and Θ cuts for the 1996 p-Be data.

Particle Species	p_T (GeV/c)	Y	Θ (mrad)	
	Min	Min	Min	Max
Λ+$\overline{\Lambda}$	0.42	2.42	54	84
Ξ^-+$\overline{\Xi}^+$	0.65	2.50	61	85
Ω^-+$\overline{\Omega}^+$	0.80	2.55	57	87

6.3 Inverse Slopes

The fitting of the m_T distributions in the acceptance windows was performed using the log likelihood method (see previous chapter). For this analysis they were fitted twice, with the final yields being calculated from the fit using the parameterisation given in equation 4.4 (page 65). To be able to compare this analysis with results from other experiments, the inverse slopes of the m_T distributions were also obtained using the alternative parameterisation,

$$\frac{dN}{dm_T} = m_T \times f(Y)e^{-m_T/T} \tag{6.1}$$

This parameterisation is suitable for particles emitted from a thermal source at a single value of Y, whereas the one shown in equation 4.4 describes particles emitted from a source which occupies a range in Y [51].

Figures 6.2, 6.3 and 6.4 show, respectively, the m_T distributions for Λs, $\overline{\Lambda}$s and Λs+$\overline{\Lambda}$s from the 1996 p-Be data. Those fitted with the parameterisation given in equation 6.1 are shown in figures 6.2(a), 6.3(a) and 6.4(a) while those in figures 6.2(b), 6.3(b) and 6.4(b) were fitted using equation 4.4. The inverse slopes found from these fits are summarised in table 6.2. It can be seen that using equation 4.4 gives a systematically lower inverse slope than using equation 6.1 as one might expect.

Table 6.2: Inverse slopes for Λs from the 1996 p-Be data.

Particle Species	Inverse Slope (MeV) Using Eqn 4.4	Inverse Slope (MeV) Using Eqn 6.1
Λ	170 ± 2.2	$180^{+2.5}_{-2.4}$
$\overline{\Lambda}$	151 ± 2.0	157 ± 2.2
$\Lambda+\overline{\Lambda}$	160 ± 1.5	169 ± 1.6

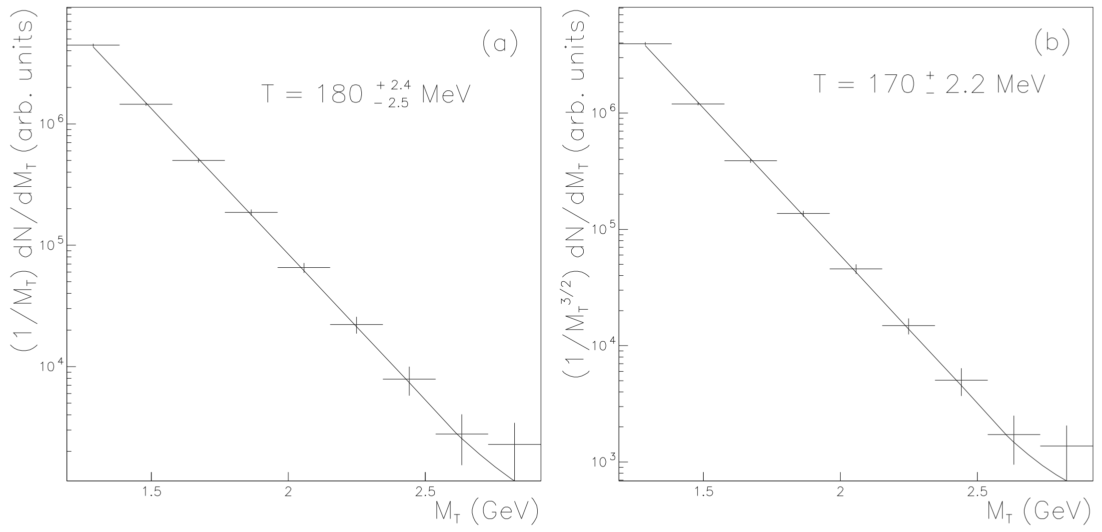

(a) (b)

Figure 6.2: m_T distributions for Λ hyperons fitted using a) equation 6.1 and b) equation 4.4.

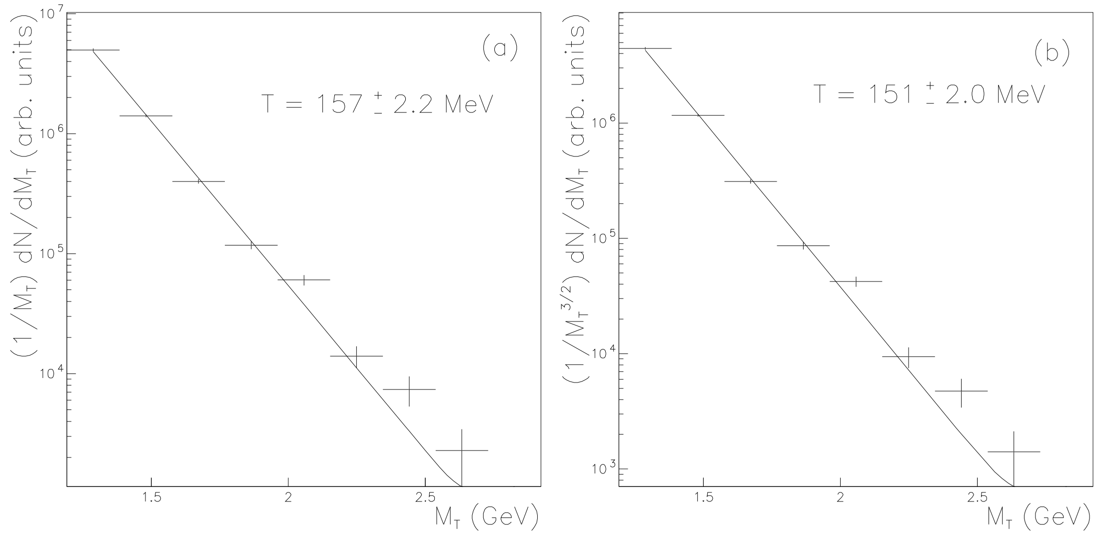

(a) (b)

Figure 6.3: m_T distributions for $\overline{\Lambda}$ hyperons fitted using a) equation 6.1 and b) equation 4.4.

6.4 Yields per Event

The yields of various particle species in the "All p_T" region calculated by the log likelihood method require further corrections to become the yields per event. To

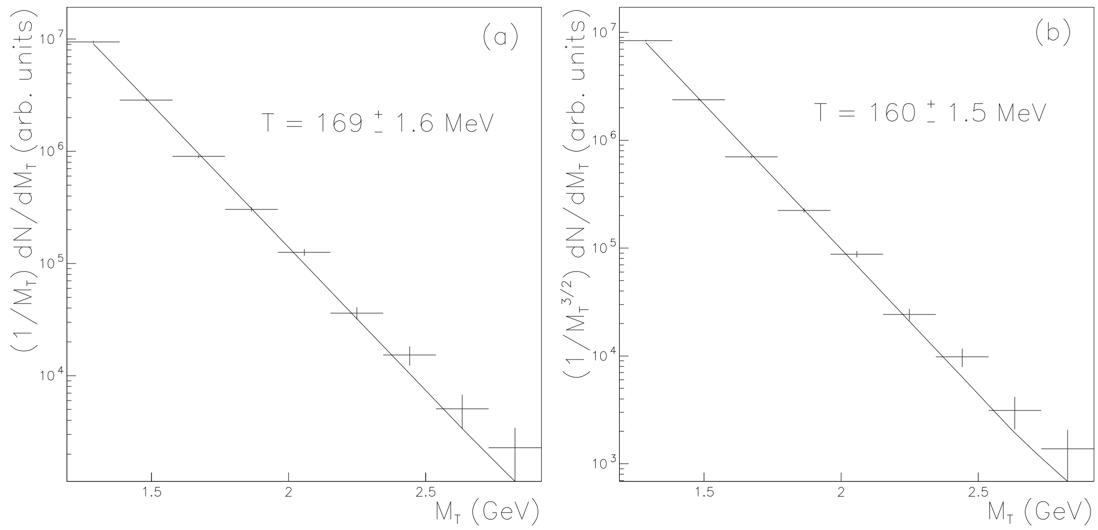

(a) (b)

Figure 6.4: m_T distributions for Λ+$\overline{\Lambda}$ hyperons fitted using a) equation 6.1 and b) equation 4.4.

allow for the unseen decay modes the yields are, as before, divided by the branching ratios given in table 5.5 (page 88). The yields are also divided by the efficiencies of the beam telescope and the two-track trigger while the thickness of the target and the number of beam particles were also taken into account. For the Λ and $\overline{\Lambda}$ hyperons the yields were scaled up by the ratio of the size of the whole sample to the size of the weighted sample. The yields per event for the 1996 p-Be Λ hyperon sample are given in table 6.3. Similar corrections were applied to the p-Pb and Pb-Pb data.

Table 6.3: Yields per event for Λs from the 1996 p-Be data.

Particle Species	Yield per event
Λ	0.0334 ± 0.0006
$\overline{\Lambda}$	0.0111 ± 0.0002
Λ+$\overline{\Lambda}$	0.0457 ± 0.0006

6.5 Number Of Participants

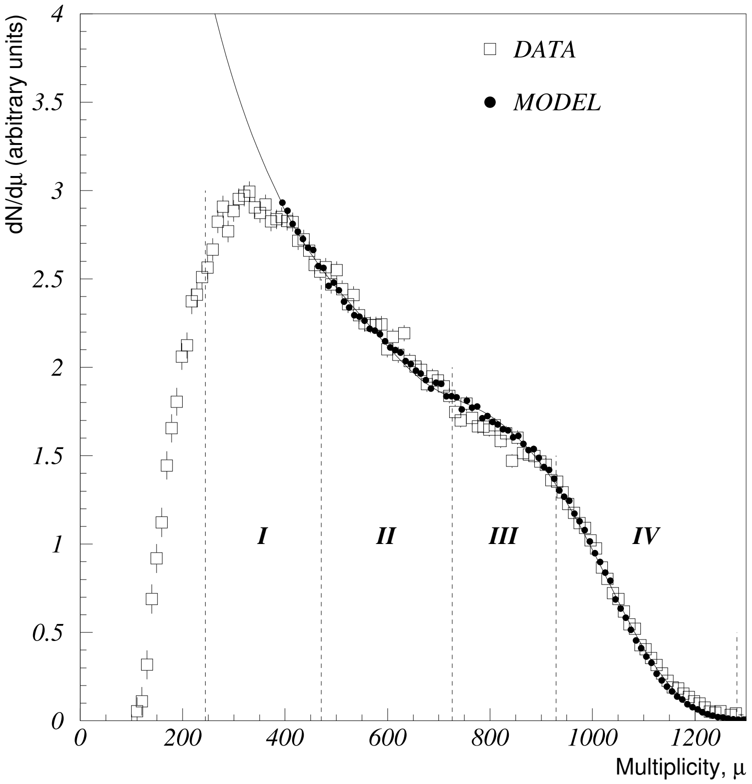

Figure 6.5: The measured multiplicity distribution for Pb-Pb with the Glauber model fit. Also visible are the four multiplicity classes into which the Pb-Pb data is subdivided.

To be able to compare the yields per event found for the different collision systems the average number of participant nucleons is required. To study the Pb-Pb data as a function of centrality the data are divided into four bins in multiplicity. These bins were chosen such that there were approximately the same number of Ω particles within each bin. These bins are shown in figure 6.5 which shows the measured multiplicity distribution corrected for acceptance, detector response, empty target contributions and secondary interactions in the target. For multiplicities less than 400 the rejection of peripheral events by the trigger causes the decrease in the distribution. Also shown in figure 6.5 is a fit to the data using a Glauber model [52] modified to account for the resolution of the multiplicity detectors. The fit is achieved for multiplicities above 400 with only one free parameter, the ratio of the multiplicity to the number of participants [53]. This allows the average number of participants to be obtained for each bin, though for bin **I** this is a weighted mean with the weight being the ratio of the measured multiplicity to the model calculation. For both the p-Pb and p-Be data the number of participants is calculated from minimum bias collisions.

6.6 Results

Table 6.4: Inverse slopes (MeV) for WA97 hyperon data.

Particle Species	Using Eqn 4.4			Using Eqn 6.1		
	p-Be	p-Pb	Pb-Pb	p-Be	p-Pb	Pb-Pb
Λ	170 ± 2.2	191 ± 8	267 ± 15	$180^{+2.5}_{-2.4}$	203 ± 9	291 ± 18
$\overline{\Lambda}$	151 ± 2.0	170 ± 14	257 ± 17	157 ± 2.2	180 ± 15	280 ± 20
Ξ^-	191 ± 12	222 ± 12	269 ± 11	202 ± 13	235 ± 14	289 ± 12
$\overline{\Xi}^+$	173 ± 16	211 ± 19	251 ± 19	182 ± 17	224 ± 21	269 ± 22
$\Omega^-+\overline{\Omega}^+$	163 ± 36	312 ± 86	225 ± 22	169 ± 40	334 ± 99	237 ± 24

Table 6.4 shows the p-Be Λ hyperon inverse slopes shown previously together with the inverse slopes for the p-Be Ξs and Ωs [54] and the corresponding values for the p-Pb and 1995 Pb-Pb data [55]. For both parameterisations of the m_T distributions the inverse slopes for Λs and Ξs show an increase with the size of the collision system. The errors on the Ω hyperon data prevent any trend from being seen.

The yields per event for the hyperon species for all WA97 data samples as a function of the average number of participants are shown in the left plot of figure 6.6. The right plot of figure 6.6 shows the yields relative to the p-Be values (*i.e.* all the

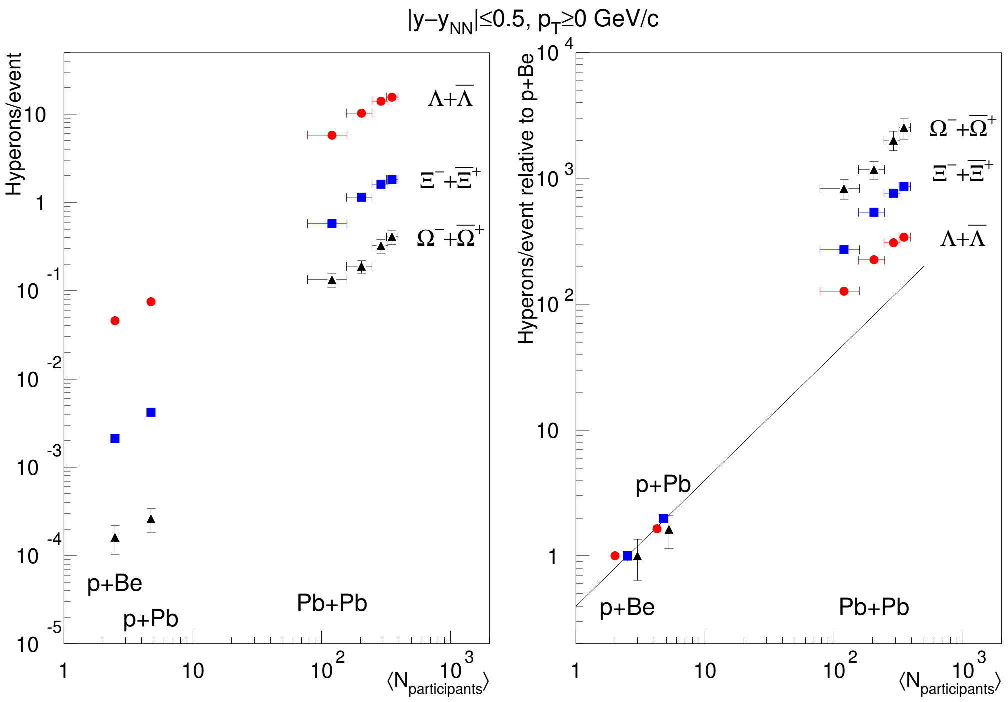

Figure 6.6: The yields per event as a function of the number of participants for the combined hyperons from all data samples (left). The yields per event normalised to the p-Be values plotted against the number of participants (right). The diagonal line represents linear scaling with the number of participants.

Λs+$\overline{\Lambda}$s yields are divided by the p-Be Λs+$\overline{\Lambda}$s yield *etc.*). The diagonal line represents a linear increase with the number of participants fixed to pass through the p-Be data. The p-Pb data lies on this line but the Pb-Pb data does not, showing that the yields per participant are the same in p-Be and p-Pb but higher in Pb-Pb. This can be seen more clearly in figure 6.7 in which the yields per event per participant relative to p-Be are plotted against the number of participants. The Pb-Pb data is clearly enhanced with respect to the proton beam data, with the enhancement increasing with the strangeness content of the particle. It is also noticable that the enhancement is constant with centrality within the Pb-Pb data, suggesting that the production of strangeness has saturated even in the most peripheral Pb-Pb collisions studied by WA97.

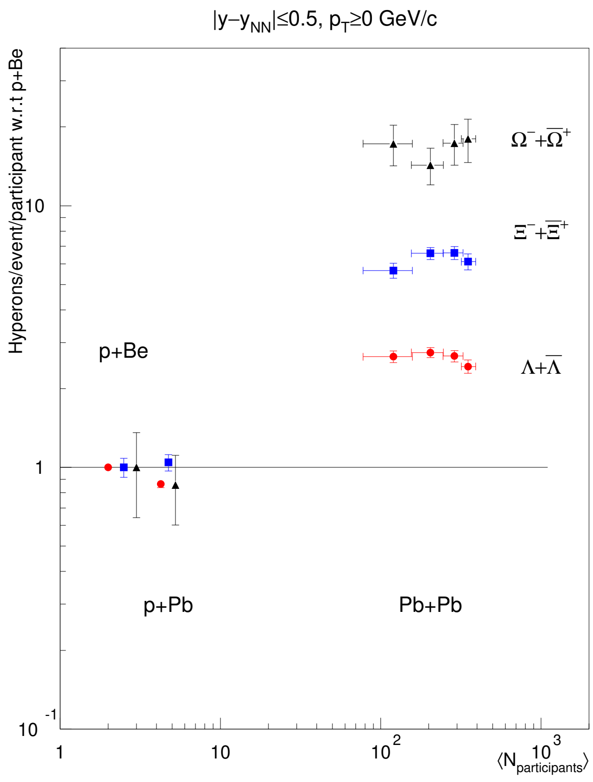

Figure 6.7: The hyperon yields normalised to p-Be per participant as a function of the number of participants.

The relative abundance of light (u and d) quarks in the central fireball due to the high stopping of SPS Pb-Pb collisions and the relative scarcity of light anti-quarks due to Pauli blocking will affect the production of different particle species. In figure 6.8, therefore, particles containing one or more light quarks are shown separately (left side plots) from those which do not (right side plots). In addition to the hyperons, the yields per event for negative hadrons (h^-) are also plotted. The upper plots show the yields per event with respect to p-Be while the lower plots show the yields per event per participant relative to p-Be. Once again the hierarchy of enhancements can be seen with the Ξ^-s being enhanced more than the Λs and the Ω^-s+$\overline{\Omega}^+$s enhancement is greater than that for $\overline{\Xi}^+$s which is in turn greater than the enhancement for $\overline{\Lambda}$s. The negative hadrons also appear to be enhanced, which could also be evidence for the formation of a QGP phase in the Pb-Pb collisions

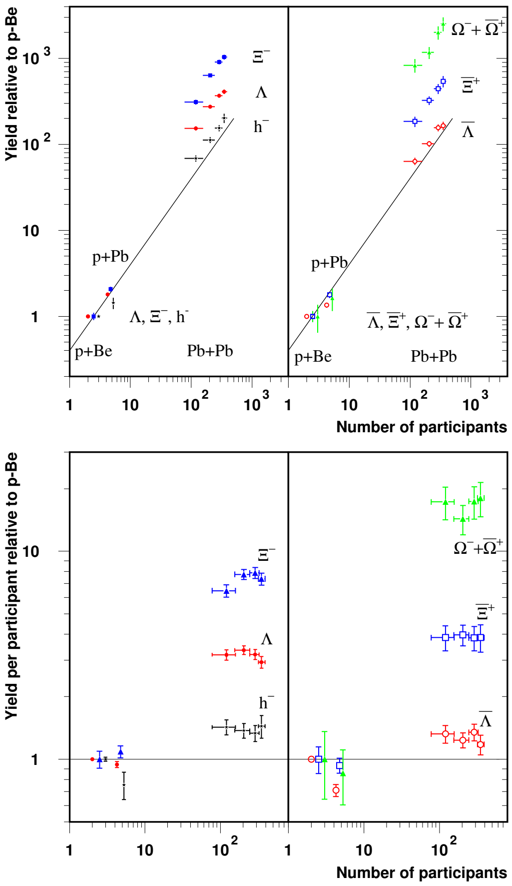

Figure 6.8: The top plots show yields normalised to p-Be for particles with a quark in common with the initial state (left) and those which do not (right). The lower plots show the yields per participant normalised to p-Be.

studied. As stated in Chapter 1 the phase transition to a QGP phase will lead to an increase in entropy which would manifest itself as an increase in the production of all particles including non-strange h^- particles. Alternatively, it is possible that the Pb-Pb h^- data represents a greater fraction of the total number of such particles produced than in the proton beam data. This could result from the different shapes of the rapidity distributions for negative hadrons in p-A and A-A collisions [56] combined with the narrow acceptance in rapidity of the WA97 detectors.

6.7 Future Prospects for Heavy Ion Physics

Absent from the discussion of WA97 results in the previous section were results on K^0. Such results have been published for the p-Pb and 1995 Pb-Pb data [41] and analysis of the p-Be K^0 sample is entering the final stages. The first results from the 1996 Pb-Pb run are, likewise, expected in the near future. It is also anticipated that use of a new data correction method, *data unfolding* [57], will allow all the WA97 data to be analysed. It has already been shown that this method is consistent with the weighting method [58].

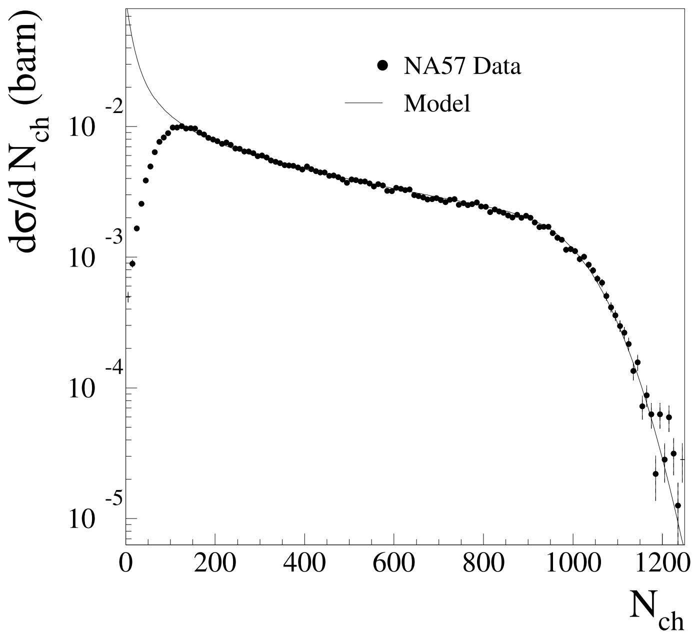

Figure 6.9: The charged particle multiplicity distribution measured by NA57. The curve is a Glauber model fit.

The successor to WA97, NA57 [40], started data taking in 1998 with a Pb-Pb run, which was performed using the standard 158 GeV/c per nucleon beam. The reduced δ-ray radiation of the beam line used by NA57 allows a wider centrality trigger, which is illustrated in figure 6.9. This means NA57 will be able to measure strangeness yields at lower values of the number of participants. During 1999 both p-Pb and Pb-Pb data has been taken using 40 GeV/c per nucleon beams, which should give further information on the phase boundary region as QGP formation is *not* expected to occur in such collisions.

The long-term future of heavy ion collisions is in collidiing beam experiments, the first of which will start taking data in May 2000 using the Relativistic Heavy Ion Collider (RHIC) at Brookhaven. The STAR Collaboration [59] will study the hadronic signals of QGP formation in the 100 + 100 GeV/c per nucleon gold beam collisions of RHIC. Another RHIC experiment, PHENIX [60], will concentrate on J/ψ suppression and photon production.

CERN is also planning to build a heavy ion colliding beam experiment. ALICE [61] will be one of the experiments using the Large Hadron Collider (LHC) which is due to be commisioned in 2005. For one month a year the LHC will switch from its nominal p-p running and will use Pb-Pb. These lead beams provide a total collision energy in excess of 1250 TeV [61], which is thirty times that of RHIC collisions. Such high energies should result in the formation of a pure QGP state , whereas SPS collisions are thought to lie very close to the phase boundary. ALICE has been designed to study many of the signatures of the QGP and the high multiplicity environment will permit some of these to be examined on an event-by-event basis. Just as the LHC will use the LEP tunnel, ALICE will use not only the collision point of the current L3 experiment but also its magnet. The layout of the ALICE detector is displayed in figure 6.10.

6.8 Conclusions

Following on from experiments WA85 and WA94, the WA97 experiment has studied strangeness production in Pb-Pb, p-Pb and, most recently, p-Be collisions at 158 GeV/c per nucleon. The geometry of the detector leads to a $Y - p_T$ accpetance window of a peculiar shape and several methods for correcting for this shape to be

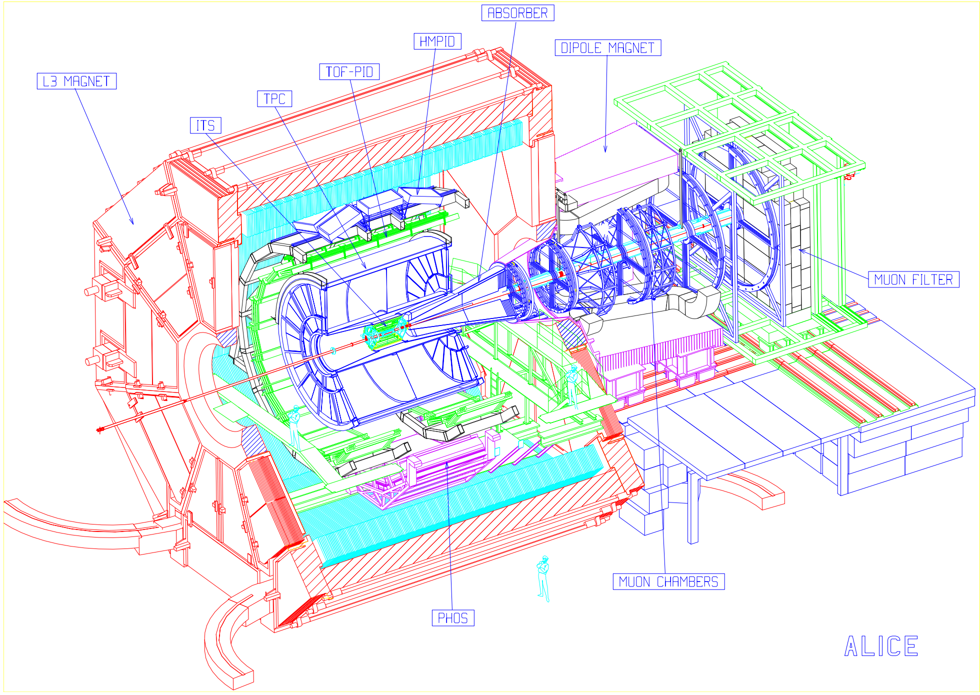

Figure 6.10: The ALICE detector.

able to extract m_T distributions have been evaluated. The best method was found to be the log likelihood method which was already in use by WA97.

Hyperons and negative hadrons have been reconstructed in the p-Be data, and the results, when combined with the previously published p-Pb and Pb-Pb data, show a significant enhancement in the yields of hyperons going from proton induced interactions to Pb-Pb collisions. The nature of this enhancement, being greater the greater the strangeness content of the particle, is very difficult to explain without invoking QGP formation. Future results from the CERN SPS heavy ion experiments and the colliding beam experiments at RHIC and ALICE will further increase the understanding of hadronic matter under extreme conditions.

Appendix A

Podolanski-Armenteros Plots

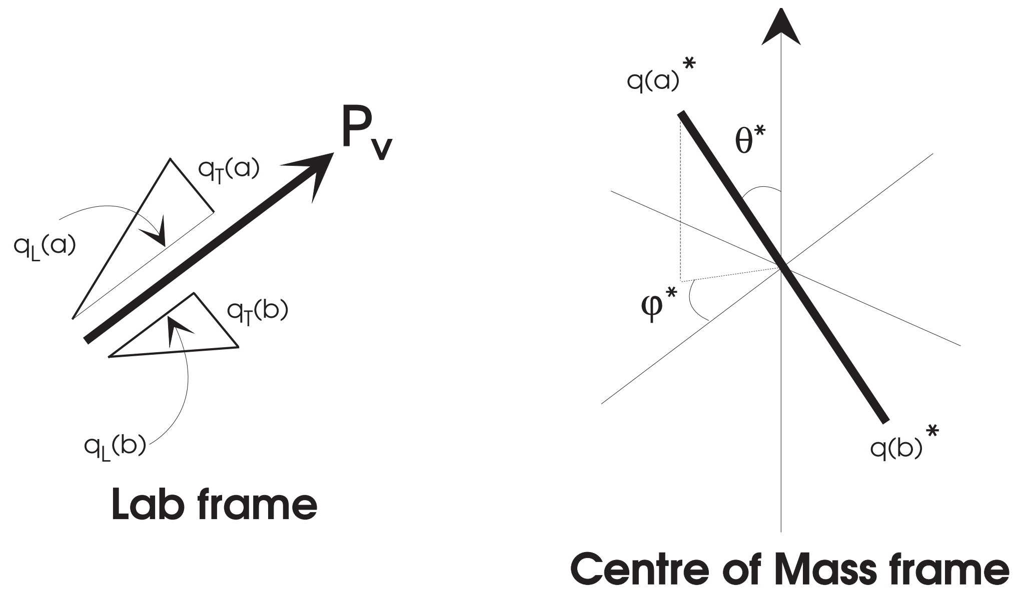

(a) (b)

Figure A.1: The decay of massive particle V into two particles in a) the laboratory frame and b) the rest frame of V. In both cases the momentum of the decay particles is with respect to the line of flight of V, P_V.

When a massive particle decays into two particles, as shown in fig A.1 (b), conservation of momentum results in

$$|q^*(a)| = |q^*(b)| = q^* \tag{A.1}$$

(the superscript * denotes quantities in the centre of mass frame) Using the definition of Θ^* in fig A.1 (b) the longitudinal and transverse momentum components of particle a relative to the line of flight of V are given by

$$q_L^*(a) = q^* \cos\Theta^* \tag{A.2}$$

$$q_T^*(a) = q^* \sin\Theta^* \tag{A.3}$$

while the total energy of a is

$$E^*(a) = \sqrt{q^{*2} + m^2(a)} \tag{A.4}$$

where $m(a)$ is the rest mass of particle a. To transform from the centre of mass frame to the laboratory frame requires use of the Lorentz transformations [5]

$$\begin{pmatrix} E \\ q_L \end{pmatrix} = \begin{pmatrix} \gamma & \gamma\beta \\ \gamma\beta & \gamma \end{pmatrix} \begin{pmatrix} E^* \\ q_L^* \end{pmatrix} \tag{A.5}$$

$$q_T = q_T^* \tag{A.6}$$

where β is the velocity of the laboratory frame in the centre of mass frame and

$$\gamma = \frac{1}{\sqrt{1-\beta^2}} \tag{A.7}$$

The resulting expressions for the energy, longitudinal and transverse momentum of a (again relative to the direction of V) are

$$E^{lab}(a) = \gamma E^*(a) + \gamma\beta q_L^*(a) \tag{A.8}$$

$$q_L^{lab}(a) = \gamma q_L^*(a) + \gamma\beta E^*(a) = \gamma q^* \cos\Theta^* + \gamma\beta E^*(a) \tag{A.9}$$

$$q_T^{lab}(a) = q_T^*(a) = q^* \sin\Theta^* \tag{A.10}$$

As can be seen from fig A.1 (b) that

$$q_L^*(b) = q^* \cos(\Theta^* + \pi) \tag{A.11}$$

Given that

$$\cos(\Theta + \pi) = -\cos\Theta \tag{A.12}$$

it follows that the laboratory frame longitudinal momentum of b is given by

$$q_L^{lab}(b) = -\gamma q^* \cos\Theta^* + \gamma\beta E^*(b) \tag{A.13}$$

Therefore

$$q_L^{lab}(a) - q_L^{lab}(b) = 2\gamma q^* \cos\Theta^* + \beta\gamma[E^*(a) - E^*(b)] \tag{A.14}$$

$$q_L^{lab}(a) + q_L^{lab}(b) = \beta\gamma[E^*(a) + E^*(b)] = \beta\gamma m_V^0 \tag{A.15}$$

where m_V^0 is the rest mass of particle V. The Podolanski-Armenteros variable, α, is defined by [47]

$$\alpha = \frac{q_L^{lab}(a) - q_L^{lab}(b)}{q_L^{lab}(a) + q_L^{lab}(b)} \tag{A.16}$$

Using the previous expressions gives [47]

$$\alpha = \frac{2q^* \cos\Theta^*}{\beta m_V^0} + \frac{E^*(a) - E^*(b)}{m_V^0} \tag{A.17}$$

This can be simplified to

$$\alpha = \zeta \cos\Theta^* + \varphi \tag{A.18}$$

using

$$\zeta = \frac{2q^*}{\beta m_V^0} \tag{A.19}$$

and

$$\varphi = \frac{E^*(a) - E^*(b)}{m_V^0} \tag{A.20}$$

Rearranging equation A.19 gives

$$\cos\Theta^* = \frac{\alpha - \varphi}{\zeta} \tag{A.21}$$

while equation A.3 gives

$$\sin\Theta^* = \frac{q_T^*}{q^*} \tag{A.22}$$

These lead to the trignometric identity

$$\cos^2\Theta^* + \sin^2\Theta^* = 1 = (\frac{\alpha - \varphi}{\zeta})^2 + (\frac{q_T^*}{q^*})^2 \tag{A.23}$$

This is the equation of an ellipse centred at (φ,0) with a semi-axis in α of ζ and a semi-axis of q^* in q_T. The values of these parameters are summarised in table A.1 for the weak decays observed by the WA97 experiment. By convention, the decay particle with the greatest charge is assigned as particle a. For the decay of a Λ hyperon to pπ^-, therefore, the proton is a while for the charge conjugate decay of a $\overline{\Lambda}$ anti-hyperon the π^+ is a. It follows from equations A.4 and A.20 that φ is positve for Λs and negative for $\overline{\Lambda}$s, as shown in fig A.2. For K^0 decays into two pions the centre of mass energies are the same, so α is determined soley by the first term of equation A.17. The result is a distribution symmetric about $\alpha = 0$, as in fig A.2. For cascade decays (both Ξ^-s and Ω^-s) the Λ hyperon is assigned as a, while it is the meson for anti-cascades. The greater mass of the kaon compared with the pion results in $|\varphi|$ being smaller for Ω hyperon decays than for Ξ hyperon decays, as illustrated in figure A.3.

Table A.1: Podolanski-Armenteros properties for weak decays studied by WA97.

Decay	ζ	q^* (GeV/c)	α_{min}	α_{max}	φ
$K^0_s \rightarrow \pi^+\pi^-$	0.8282	0.206	-0.8282	0.8282	0
$\Lambda \rightarrow p\pi^-$	0.179	0.101	0.515	0.873	0.694
$\overline{\Lambda} \rightarrow \overline{p}\pi^+$	0.179	0.101	-0.873	-0.515	-0.694
$\Xi^- \rightarrow \Lambda\ \pi^-$	0.210	0.139	0.4918	0.9118	0.7018
$\overline{\Xi}^+ \rightarrow \overline{\Lambda}\ \pi^+$	0.210	0.139	-0.9118	-0.4918	-0.7018
$\Omega^- \rightarrow \Lambda$ K$^-$	0.257	0.211	0.1009	0.6149	0.3579
$\overline{\Omega}^+ \rightarrow \overline{\Lambda}$ K$^+$	0.257	0.211	-0.6149	-0.1009	-0.3579

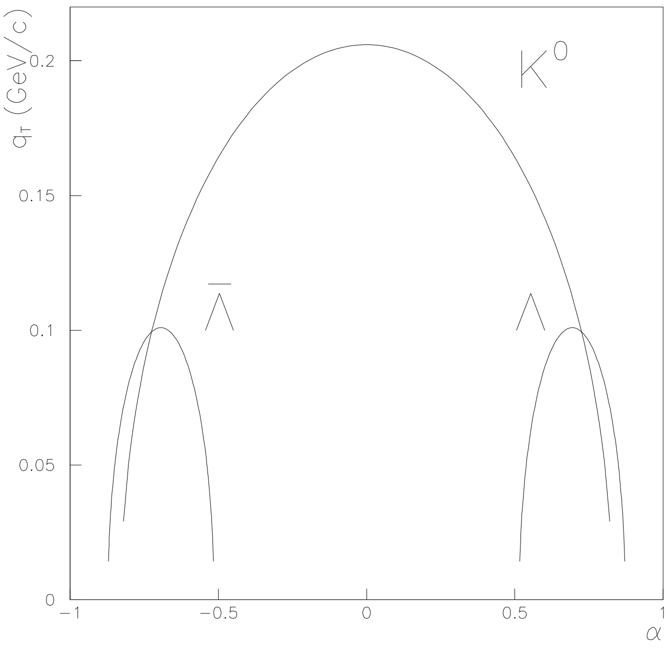

Figure A.2: The Armenteros-Podolanski curves for K^0s, Λs and $\overline{\Lambda}$s.

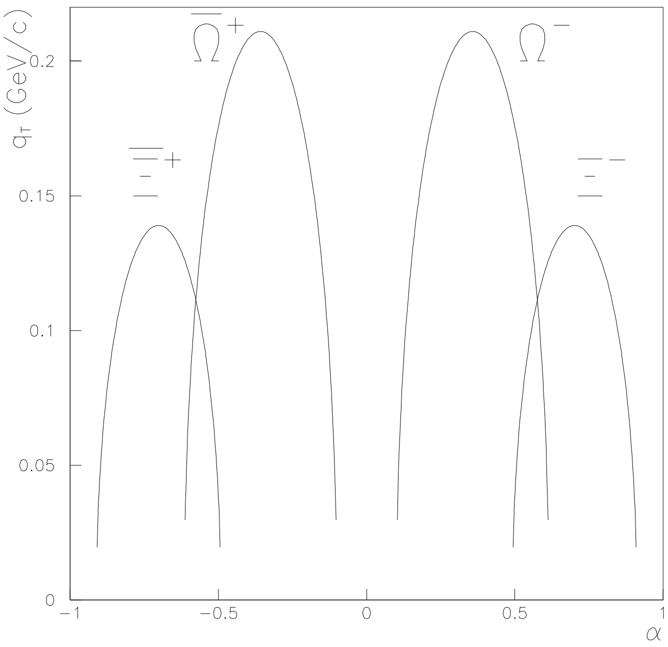

Figure A.3: The Armenteros-Podolanski curves for Ξ^-s, $\overline{\Xi}^+$s , Ω^-s and $\overline{\Omega}^+$s.

Appendix B

Evaluating p_T As A Function Of Y and Θ

Due to the shape of the silicon telescope used in the WA97 experiment, it is necessary to determine p_T as a function of rapidity Y and Θ, the angle in the x-z plane of a particle's track with respect to the beam. The starting point is the definition of rapidity

$$Y = \frac{1}{2} \ln \frac{E + p_L}{E - p_L} \tag{B.1}$$

where E and p_L are the energy and longitudinal momentum of the particle respectively. Rearranging and taking the exponent gives

$$e^{2Y} = \frac{E + p_L}{E - p_L} \tag{B.2}$$

which can be further rearranged to give

$$Ee^{2Y} - p_L e^{2Y} = E + p_L \tag{B.3}$$

Collecting terms results in the following expression

$$p_L = E \frac{(e^{2Y} - 1)}{(e^{2Y} + 1)} \tag{B.4}$$

which becomes

$$p_L = E\frac{(e^Y - e^{-Y})e^Y}{(e^Y + e^{-Y})e^Y} \tag{B.5}$$

when factorising both the denominator and numerator. Using the definition of $\tanh x$ and squaring, this simplifies to

$$p_L^2 = E^2 \tanh^2 Y \tag{B.6}$$

From the trigonometric identities

$$\cosh^2 x - \sinh^2 x = 1 \tag{B.7}$$

and

$$\frac{\sinh^2 x}{\cosh^2 x} = \tanh^2 x \tag{B.8}$$

it can be shown that

$$\tanh^2 x = 1 - \frac{1}{\cosh^2 x} \tag{B.9}$$

Substituting this into equation B.6 gives

$$p_L^2 = E^2 - \frac{E^2}{\cosh^2 Y} \tag{B.10}$$

which is equivalent to

$$E^2 - p_L^2 = \frac{E^2}{\cosh^2 Y} \tag{B.11}$$

The energy E is defined by

$$E^2 = m^2 + p^2 \tag{B.12}$$

which using the definitions of p,

$$p^2 = p_L^2 + p_T^2 \tag{B.13}$$

and m_T,

$$m_T^2 = m^2 + p_T^2 \tag{B.14}$$

becomes

$$E^2 = m_T^2 + p_L^2 \tag{B.15}$$

Sustituting this into equation B.11 gives

$$m_T^2 \cosh^2 Y = E^2 \tag{B.16}$$

which can be rewritten using equation B.7 as

$$m_T^2(1 + \sinh^2 Y) = E^2 \tag{B.17}$$

Expanding this and rearranging results in

$$m_T^2 \sinh^2 Y = E^2 - m_T^2 \tag{B.18}$$

Using equation B.15 yields

$$p_L^2 = m_T^2 \sinh^2 Y \tag{B.19}$$

Using the definitions of the longitudinal and transverse components of momentum,

$$p_L = p \cos \Theta \tag{B.20}$$

and

$$p_T = p \sin \Theta \tag{B.21}$$

with the definition of m_T given in equation B.14 allows equation B.19 to be expanded into

$$p^2 \cos^2 \Theta = m^2 \sinh^2 Y + p^2 \sin^2 \Theta \sinh^2 Y \tag{B.22}$$

Collecting terms in p gives

$$p^2(\cos^2 \Theta - \sin^2 \Theta \sinh^2 Y) = m^2 \sinh^2 Y \tag{B.23}$$

which becomes

$$p^2 = \frac{m^2 \sinh^2 Y}{(\cos^2 \Theta - \sin^2 \Theta \sinh^2 Y)} \tag{B.24}$$

From equations B.24 and B.21 we obtain the required formula

$$p_T = \frac{m \sinh Y \sin \Theta}{\sqrt{\cos^2 \Theta - \sin^2 \Theta \sinh^2 Y}} \tag{B.25}$$

Appendix C

The Principle of Maximum Likelihood

If one has a finite set of measured values $(x_1, \ldots, x_n)$ which are related to a set of parameters α_i, then $P(x_j, \alpha_i)$ is the probability that a measurement x lies between x_j and $x_j + dx_j$. The probability of obtaining the set $(x_1, \ldots, x_n)$ is, therefore,

$$P(x_1, \ldots, x_n; \alpha_i) = \prod_{j=1}^{n} P(x_j, \alpha_i) \tag{C.1}$$

This probability is the *likelihood*, $\mathcal{L}(\alpha_i)$, of obtaining the measurements $(x_1, \ldots, x_n)$ given the parameters α_i. Varying the parameters α_i will change the likelihood, so by finding the α_i's which maximise the likelihood the best fit to the data will be obtained - this is the Principle of Maximum Likelihood [62].

For a large data set, the product of the individual probabilities will become very large. By taking the logarithm this becomes a sum, giving

$$ln(\mathcal{L}(\alpha_i)) = \sum_{j=1}^{n} ln(P(x_j, \alpha_i)) \tag{C.2}$$

By maximising the logarithm of the likelihood, $ln(\mathcal{L}(\alpha_i))$, the set of best fit parameters found will the same set found by maximising $\mathcal{L}(\alpha_i)$, but the calculation will be more manageable.

Bibliography

[1] J.C. Collins and M.J. Perry, Phys. Rev. Lett. **34** (1975) 1353.

[2] L. Van Hove, *"Quark Gluon Plasma and Multiparticle Production"*, CERN-TH.5236/88.

[3] B. Müller, *"The Physics of the Quark Gluon Plasma"*, Springer-Verlag (1985).

[4] D. J. Gross and F. Wilczek, Phys. Rev. **D8**, (1973) 3633.

[5] D.H. Perkins, *"Introduction to High Energy Physics"*, Addison-Wesley Publishing Company, Third Edition (1987) 291-297.

[6] F. Halzen and A. D. Martin, *"Quarks and Leptons: An Introductory Course in Modern Particle Physics"*, John Wiley & Sons (1984).

[7] W. E. Burcham and M. Jobes, *"Nuclear and Particle Physics"*, Longman Scientific & Technical (1995).

[8] F. Karsch *et al.*, Z. Phys. **C 37** (1988) 617-622.

[9] T. Matsui and H. Satz, Phys. Lett. **B 178** (1986) 416.

[10] S. Gottlieb *et al.*, Phys. Rev. **D35** (1987) 3972.

[11] T. C. Awes (WA80 Coll.), Nucl. Phys. **A590** (1995) 81c-92c.

[12] P. Wurm, Nucl. Phys. **A590** (1995) 103c-116c.

[13] S. Ramos (NA38 Coll.), Nucl. Phys. **A590** (1995) 117c-126c.

[14] M. Masera (HELIOS Coll.), Nucl. Phys. **A590** (1995) 93c-102c.

[15] J. Letessier, A. Tounsi, U. Heinz, J. Sollfrank and J. Rafelski, Phys. Rev. Lett. 70 (1993) 3530.

[16] J. Rafelski and B. Müller, Phys. Rev. Lett. **48** (1982) 1066.
J. Rafelski and B. Müller, Phys. Rev. Lett. **56** (1986) 2334.

[17] U. Heinz, Nucl. Phys. **A566** (1994) 205c.

[18] R. Albrecht *et al.* (WA80 Coll.), Phys. Rev. Lett. **76** (1996) 3506-3509.

[19] D. K. Srivastava and B. C. Sinha, Eur. J. Phys. C (1999).

[20] B. Lenkeit *et al.* (CERES Coll.), Proc. 15^{th} *Int. Conf. on Ultra-Relativistic Nucleus-Nucleus Collisions (Quark Matter '99)*, Turin, Italy, 10-15 May 1999, to be published Nucl. Phys. **A**.

[21] B. Lenkeit *et al.* (CERES Coll.), to be published in proceedings *INPC'98*, Paris, France, Nucl. Phys. **A** (1999).

[22] A. L. S. Angelis *et al.* (HELIOS/3 Coll.), CERN-EP/98-82

[23] C. M. Ko *et al.*, Nucl. Phys. **A610** (1996) 342c.

[24] G. Q. Li *et al.*, *APCTP Workshop on Astro-Hadron Physics*, Seoul, Korea, October 1997.
G. E. Brown and M. Rho, Phys. Lett. *66*, 2720 (1991).

[25] K. Haglin, Nucl. Phys. **A584**, (1995) 719.
K. Haglin, Phys. Rev. **C57**, (1998) 1449-1453.

[26] Addendum to proposal SPSLC/P280: CERN/SPSLC/96-35 SPSLC/P280 Add.1. (1996)

[27] M. C. Abreu *et al.* (NA50 Coll.), Phys. Lett. **B 450** (1999) 456.

[28] C. Gershel and J. Hüfner, Z. Phys. **C 56** (1992) 171.

[29] M. C. Abreu *et al.* (NA50 Coll.), Phys. Lett. **B 410** (1997) 337.

[30] J. Rafelski, J. Letessier and A. Tounsi, Proc. *XXVI Int. Conf. on High Energy Physics*, Dallas, TX, USA, American Institute of Physics, New York, ed. J. R. Sanford, (1992) 983-990.

[31] P. Koch, B. Müller and J. Rafelski, Phys. Rep. **142** (1986) 167.

[32] Thesis of R. P. Barnes, *"Production of Strange and Multistrange Baryons in Ultra-Relativistic Heavy Ion Collisions"*, The University of Birmingham (1993).

[33] J. Rafelski, Phys. Lett. **B262** (1991) 333.

[34] D. Di Bari *et al.* (WA85 Coll.), Nucl. Phys. **A590** (1995) 307c-315c.

[35] J. B. Kinson *et al.* (WA94 Coll.), Nucl. Phys. **A590** (1995) 317c-331c.

[36] F. Antinori *et al.* (WA85 Coll.), Phys. Lett. **B 447** (1999) 178-182.

[37] M. Venables for the WA94 Collaboration, Proc. *Int. Symposium on Strangeness in Quark Matter: SQM '97*, Thera, Santorini, Greece, ed. A. D. Pantegiotou, publ. in J. Phys. G: Nucl. Part. Phys. **23** No. 12, (1997) 1857-1864.

[38] WA97 Proposal, CERN/SPSLC/91-29 SPSLC/P263 (1991).

[39] J. W. Cronin *et al.*, Phys. Rev **D11**, 3105 (1975).
D. Antreasyan *et al.*, Phys. Rev. **D19**, 764 (1979).

[40] NA57 Proposal, CERN/SPSLC/96-40 SPSLC/P300 (1996).

[41] E. Andersen *et al.* (WA97 Coll.), CERN Preprint CERN-EP/99-29, to be publ. in Phys. Lett. **B**.

[42] C. Bovet *et al.*, *"The CEDAR counters for Particle Identification in the SPS Secondary Beams: A Description and an Operation Manual"*, CERN Yellow Report 82-13 (1982).

[43] F. Antinori *et al.* (WA97 Coll.), Nucl. Phys. **A590** (1995) 139c-146c.

[44] E. H. M. Heijne *et al.* (RD19 Coll.), Nucl. Instr. Meth. **A349** (1994) 138-155.

[45] Particle Data Group, Phys. Rev. **D54** (1996) 1-720.

[46] Application Software Group, *PAW tutorial*, CERN Program Library Q121.

[47] J. Podolanski and R. Armenteros, Phil. Mag 45 (1954) 13.

[48] Application Software Group, *GEANT manual*, CERN Program Library W5013.

[49] F. James, *MINUIT manual*, CERN Program Library D506.

[50] J. Rafelski and J. Letessier, Proc. 15^{th} *Winter Workshop on Nuclear Dynamics*, Park City, UT, USA, 9-16 January 1999.

[51] E. Schnedermann, J. Sollfrank and U. Heinz, NATO ASI Series **B303** (1993) 175.

[52] A. Bialas, M. Bleszyński and W. Cynż, Nucl. Phys. **B111** (1976) 461.
D. Kharzeev, C. Lourenço, M. Nardi and H. Satz, Z. Phys. **C74** (1997) 307.

[53] N. Carrer *et al.* (WA97 and NA57 Coll.), Proc. 15^{th} *Int. Conf. on Ultra-Relativistic Nucleus-Nucleus Collisions (Quark Matter '99)*, Turin, Italy, 10-15 May 1999, to be published Nucl. Phys. **A**.

[54] D. Elia *et al.* (WA97 Coll.), Proc. 15^{th} *Int. Conf. on Ultra-Relativistic Nucleus-Nucleus Collisions (Quark Matter '99)*, Turin, Italy, 10-15 May 1999, to be published Nucl. Phys. **A**.

[55] E. Andersen *et al.* (WA97 Coll.), Phys. Lett. **B433** (1998) 209.

[56] G. Roland *et al.* (NA49 Coll.), Nucl. Phys. **A638** (1998) 91c-102c.

[57] V. Blobel, In: CERN 85-09 (1985) 88-127.

[58] L. Šándor *et al.* (WA97 Coll.), Proc. 15^{th} *Int. Conf. on Ultra-Relativistic Nucleus-Nucleus Collisions (Quark Matter '99)*, Turin, Italy, 10-15 May 1999, to be published Nucl. Phys. **A**.

[59] J. W. Harris *et al.* (STAR Coll.), Proc. 10^{th} *Int. Conf. on Ultra-Relativistic Nucleus-Nucleus Collisions (Quark Matter '93)*, Borlange, Sweden, June 20-24 1993, ed. E. Stenlund, H. F. Gustafsson, A. Oskarsson and I. Otterlund, publ. in Nucl. Phys. **A566** (1994) 277c-286c.

[60] J. T. Mitchell *et al.* (PHENIX Coll.), Proc. 14^{th} *Int. Conf. on Particles and Nuclei (PANIC '96)*,Williamsberg, VA, USA, 1996, publ. in World Scientific (1996) 433.

[61] ALICE Proposal, CERN/LHCC/95-71 (1995).

[62] J. R. Taylor, "An Introduction to Error Analysis: The Study of Uncertainties in Physical Measurments", University Science Books (1982).